NUCLEAR STRUCTURE STUDIES OF NEUTRON-RICH NUCLEI PRODUCED IN THE SPONTANEOUS FISSION OF ^{252}Cf: TRIAXIALITY NEAR $A = 110$; SPHERICAL SHAPES AND OCTUPOLE CORRELATIONS BEYOND ^{132}Sn

By

Shaohua Liu

Dissertation

Submitted to the Faculty of the

Graduate School of Vanderbilt University

in partial fulfillment of the requirements

for the degree of

DOCTOR OF PHILOSOPHY

in

Physics

December 2010
Nashville, Tennessee

Approved:

Professor Joseph H. Hamilton

Professor Akunuri V. Ramayya

Professor Charles F. Maguire

Professor Sait A. Umar

Professor Robert A. Weller

DEDICATION

To

Richard and Zhenfeng

ACKNOWLEDGMENTS

It has be an honor and a pleasure to be advised by Professor Joseph H. Hamilton and Professor Akunuri V. Ramayya for my research project. Their personality and enthusiasm in science taught and encouraged me so much. It is an invaluable experience in my career to work with them. This dissertation would not have been accomplished without their patient, priceless assistance and support. I would like to express my heartfelt gratefulness to them.

Acknowledgments should be given to Professors Charles F. Maguire, Sait A. Umar, and Robert A. Weller for their service in my Ph.D. committee. The wonderful environment provided by the Department of Physics and Astronomy at Vanderbilt University is very important for my four-year graduate life. I would also like to express my thanks to those in the nuclear physics group. Ke Li and Chris Goodin, two former graduate students, taught me how to carry out data analysis. Prof. Yixiao Luo and Dr. Jae-Kwang Hwang gave many very useful comments on my research. Mrs. Carol Soren supplied me with continuous aids in organizing documents, planning for travel, and doing paperwork. I also enjoy working together with Nathan Brewer.

My gratitude should be extended to those individuals at ORNL and UNIRIB of ORAU who have taken the time from their intensely busy schedules to teach me and assist me in many aspects during my stay there. They are, but not limited to, Dr. Krzysztof Rykaczewski, Dr. Ken Carter, Dr. Jon Batchelder, Dr. Dan Stracener and Dr. Nick Stone. I benefited a great deal from the discussion with Dr. John Rasmussen of LBNL. I also thank Dr. Aldo Covello and Dr. Angela Gargano of

University of Naples Federico II for discussions with them on the shell model and their work on the shell-model calculations. Communication with Dr. Adrian Gelberg of University of Cologne and his calculations on triaxiality enriched my understanding of some nuclear properties. Prof. Shengjiang Zhu of Tsinghua University also helped me in my study.

Special thanks should be given to my family. I could always receive support and encouragement from my parents. Zhenfeng, my wonderful wife, is always standing up for me, which gives me courage and confidence. I am also extremely grateful for the arrival of my lovely son, Richard, who empowers me to move forward.

I wish that I could list all the persons who helped me in the past four years, but I cannot.

The work at Vanderbilt University is supported in part by the US Department of Energy under Grant and Contract Nos. DE-FG05-88ER40407.

TABLE OF CONTENTS

LIST OF TABLES

LIST OF FIGURES

CHAPTER I

INTRODUCTION

Nuclear physics can trace its origin to Rutherford's proposal of the atomic nucleus in 1911. Since then, the understanding of the structure of the nucleus has grown immensely in both theory and experiment with enormous amounts of theoretical and experimental efforts. Generally, theoretical answers to the nuclear many-body problem are partly phenomenological. So, nuclear theory and experiment are closely tied together, where theory finds its inspiration from experiment for the structure and parameters of models, while experiment takes its inspiration from theory in finding out what kind of experiments are most practical to test nuclear models. However, there is no single theory that has the capability for interpreting all of the rich variety of phenomena observed experimentally in nuclei. Instead, there are many different models proposed to attempt at explaining and characterizing different phenomena. There have been different methods and techniques to perform nuclear experiments as well. Therefore, nuclear physics research utilizes a broad range of experimental and theoretical techniques. As new experimental techniques promote researchers' ability to study nuclei farther and farther away from stability, nuclear physics research has moved towards more and more exotic fields and new theoretical models have been required to interpret novel phenomena.

A nucleus is defined by the proton number Z and the neutron number N, or the mass number $A = Z + N$. One may write all these three numbers explicitly

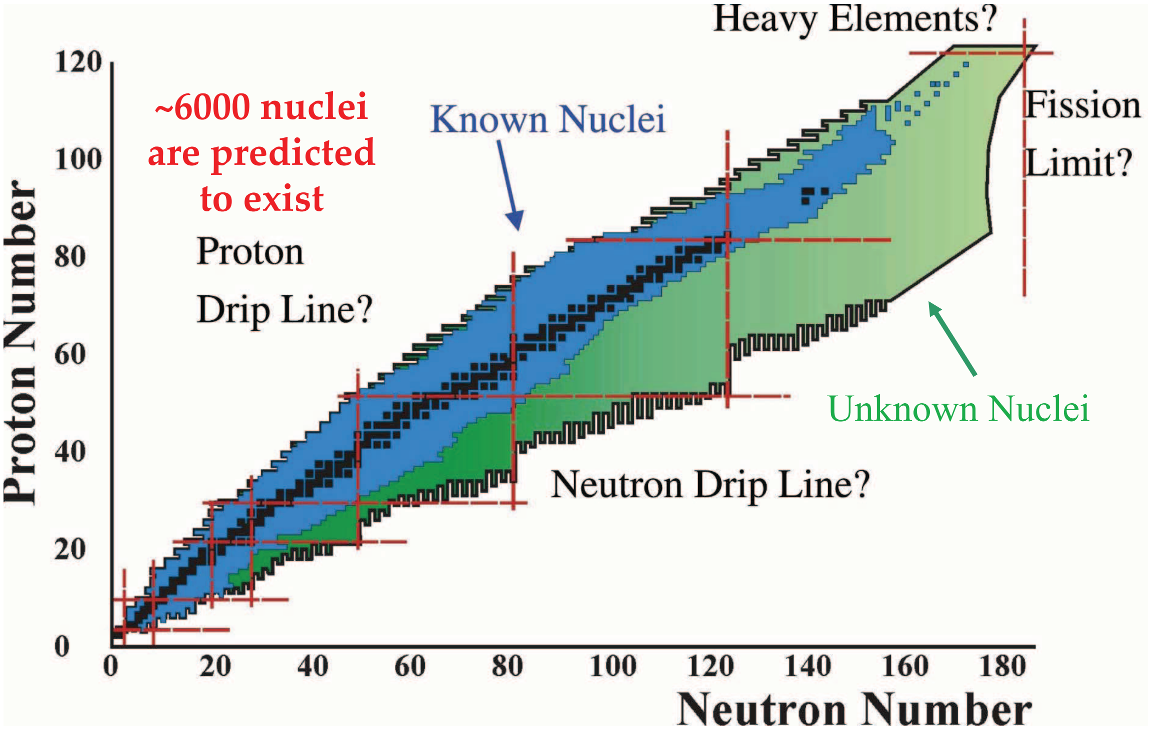

Figure 1.1: Chart of nuclides. Stable nuclei are indicated in black and major spherical closed shells are indicated by vertical and horizontal lines.

to describe a nucleus like ${}^{A}_{Z}\mathrm{X}_{N}$, where X is the atomic symbol. Figure 1.1 shows a nuclide chart, with the stable nuclei indicated in black. The stability of a nucleus is closely related to the forces holding its nucleons together and determined by the competition between the attractive nuclear forces and the disruptive Coulomb forces. One expects that the nuclear stability will be lost first at the so-called neutron drip line, where nuclei have zero binding for the next neutron, or the proton drip line, where the next proton has no binding. The stable nuclei form a region, which can be called the valley of beta-stability. Nuclei outside this valley are unstable.

Today, the study of exotic nuclei, which are far from the valley of beta-stability, either neutron-rich or proton-rich, presents an important challenge for nuclear physics.

Nuclear models have to be radically improved in order to accommodate the wealth of new phenomena that have been observed by the continuing experimental efforts. Though we are still far from having a unified theory to describe those observations, much important progress has been made. For example, modern improvements in the shell model have been made by using interactions obtained from nucleon-nucleon potentials that fit the nucleon-nucleon phase shifts. The current nuclear physics frontiers involve studying nuclei at the extremes, including neutron-rich or proton-rich nuclei, high-spin states, larger deformations, exotic shapes, and so on. These investigations extend not only the available range of nuclei, but also new physics pictures related to the proton/neutron ratio in nuclei. For example, the properties of neutron-rich nuclei related to the rapid neutron capture r-process are very important to understand the nuclear synthesis in the universe. The r-process path cannot be known without knowing the structures of these neutron-rich nuclei far from stability.

The study of nuclei at high spin is an active topic in nuclear structure studies. High-spin studies can provide experimental evidence for many exotic and interesting phenomena and thus very effective tests for the corresponding models. High-spin states can be formed by either driving individual nucleons to higher angular momentum orbits or making the core of paired nucleons rotate rapidly. The excitation energies can be in the form of the collective rotations or vibrations of the entire core. If the core rotates fast enough, one nucleon pair in the core may be broken with the addition of two valence nucleons, resulting in the occurrence of backbending of the moment of inertia. The collective structure and the single particle structure of nuclei are complementary and competitive to each other. Therefore, the studies of high-spin states are valuable to understand the relative importance of collectivity and individuality in a nucleus for developing nuclear models.

One main method to produce neutron-rich nuclei in high-spin states is the spontaneous fission of ^{252}Cf. Measuring γ-rays emitting from the fission fragments allows us to study the behavior of these excited nuclei as they deexcite to their ground states or isomeric states through γ-ray emission. With the development of the sophisticated experimental facilities and data acquisition and analysis techniques, we are able to identify the γ-rays of a specific nucleus and build its level scheme with a plentiful supply of information regarding the nuclear structure of this nucleus.

In the present work, we have investigated the prompt γ-ray spectroscopy of the fission fragments produced in the spontaneous fission of ^{252}Cf. We focus on the isotopes in the mass regions where exotic nuclear shapes appear, such as ^{114,115}Rh in the $A = 110$ region with triaxiality and ^{140,142}Cs in the region related to octupole correlations. We are also interested in the nuclei with a few nucleons beyond the doubly-magic core ^{132}Sn, where the spherical shell model is suitable to describe their nuclear properties with effective interactions. In Chapter II, some theoretical topics related to the current work will be introduced. In Chapter III, several experimental techniques employed in the present experiment and data analysis will be presented. The remaining chapters will give the experimental and theoretical results. The corresponding details will be presented in each chapter.

CHAPTER II

THEORETICAL BACKGROUND

In this chapter, a few theoretical topics related to the current studies will be presented. A brief introduction of two types of natural decay processes will be given first. Then three major nuclear models, namely the spherical shell model, the collective model, and the unified model, will be described in detail to some extent. In Section 2.3, various nuclear shapes predicted by theory or observed in experiment will be discussed, especially the spherical shape and those related to triaxial deformations and octupole deformations/correlations, which have been observed in the present work.

2.1 Natural decay processes

There are a few decay processes that have been observed naturally. In this section, we will only focus on two processes that are related to our studies. They are the γ decay and spontaneous fission.

2.1.1 γ decay

A nucleus in excited states can release its "extra" energies and decays to lower states through electromagnetic radiations known as γ decay. The level energies and spin-parities (I^{π}) of excited states establish the level structures of nuclei and the investigation of γ-rays emitted from nuclei can reveal their nuclear properties.

The multipolarity of a γ-ray transition is a quantity that is related to the spins and parities of the initial and final states connected by this transition. In this process, both angular momentum and parity are conserved. Multipolarity is a term to describe the character of the electromagnetic radiation emitted from nuclei. The character of the radiation depends on the shape and time dependence of the charge distribution that produces it. It can either be electric (E) or magnetic (M) with a quantized angular momentum (L). Therefore, multipolarity of a γ-ray transition is denoted as EL or ML. Since the intrinsic spin of a photon is one, the angular momentum change for a γ-ray transition must be integral. Multipolarity of a transition is determined by the spin-parity selection rules:

$$L = \mid I_i - I_f \mid, \mid I_i - I_f \mid +1, \mid I_i - I_f \mid +2, \cdots, I_i + I_f \qquad (\text{no } L = 0) \tag{2.1}$$

and

$$\pi_i \pi_f = (-1)^L \tag{2.2}$$

for electric transtions, or

$$\pi_i \pi_f = (-1)^{L+1} \tag{2.3}$$

for magnetic transitions, where i and f stand for the initial and final states, respectively. For example, a $9/2^- \rightarrow 7/2^+$ transition could have a multipolarity of $M8, E7, M6, E5, M4, E3, M2$ or $E1$. The γ-ray transition probability for a given

E/ML, $T(E/ML; I_i \rightarrow I_f)$, can be obtained in the form of

$$T(E/ML; I_i \rightarrow I_f) = \frac{8\pi(L+1)}{L\big[(2L+1)!!\big]^2}\frac{1}{\hbar}\Big(\frac{E_\gamma}{\hbar c}\Big)^{2L+1} B(E/ML; I_i \rightarrow I_f), \tag{2.4}$$

where E_γ is the photon energy and $B(E/ML; I_i \rightarrow I_f)$ is the reduced transition probability, written in terms of the reduced matrix element as

$$B(E/ML; I_i \rightarrow I_f) = \frac{1}{2I_i+1}\left|< I_f \parallel \mathscr{M}(E/ML) \parallel I_i >\right|^2. \tag{2.5}$$

$< I_f \parallel \mathscr{M}(E/ML) \parallel I_i >$ is the so-called reduced matrix element and $\mathscr{M}(E/ML)$ is the electromagnetic operator. Then the values for the relative intensities of various multipoles can be estimated as

$$T(M1) : T(E2) : T(M3) : T(E4) \approx 1 : 1 \times 10^{-3} : 2 \times 10^{-10} : 1 \times 10^{-13} \tag{2.6}$$

and

$$T(E1) : T(M2) : T(E3) : T(M4) \approx 1 : 2 \times 10^{-7} : 2 \times 10^{-10} : 2 \times 10^{-17}. \tag{2.7}$$

We consider only the lowest multipoles since the probability goes down rapidly with increasing angular momentum carried away by the photon. So, the $9/2^- \rightarrow 7/2^+$ transition is expected to have a pure $E1$ multipolarity, with negligible relative intensities for other higher multipoles. In practice, if the multipolarity of a transition is known, it becomes possible to determine the I^π of the initial or the final state with known

I^π of one of these two states.

The multipolarity of a transition may affect some observable properties like lifetime of the initial state. Compared to α decay (10^{-5}-10^{17} seconds) and β decay (10^{-2}-10^{13} seconds), lifetime for γ decay is usually very short (10^{-12}-10^{-9} seconds). However, there are some levels, with lifetime of the order of 10^{-6} seconds or greater, which are called isomers. Generally, an isomeric state arises because multipolarity of the allowed transition from this level decaying to the lower level is very high.

The preceding example of the $9/2^- \to 7/2^+$ transition has a pure $E1$ multipolarity. However, some transitions do not have a pure multipolarity. For example, let us consider a $9/2^+ \to 7/2^+$ transition. It is possible for this transition to be either pure $M1$, pure $E2$ or $E2/M1$ mixed. The term, mixing ratio δ, which will be defined next, is used to describe such a situation.

One way to determine the angular momentum carried by a transition is to measure the angular correlation between two or more successive γ-ray transitions in a cascade, which include the transition of interest. The theoretical foundation for the angular correlation was first proposed in 1940 [1]. Early angular correlation experiments were carried out with only two or three detectors and were often restricted to 90°, 135°, or 180°. The angular correlation function $W(\theta)$ for two successive γ-ray transitions, $\gamma_1(L_1, L_1')$ and $\gamma_2(L_2, L_2')$, with the initial state I_1, intermediate state I_2, and final state I_3, as shown in Fig. 2.1, can be expressed as a Legendre polynomial expansion over all permitted orders k [2]

$$W(\theta) = 1+A_2(\gamma_1)A_2(\gamma_2)P_2(cos\theta)+A_4(\gamma_1)A_4(\gamma_2)P_4(cos\theta)+\cdots+A_{k_{max}}(\gamma_1)A_{k_{max}}(\gamma_2)P_{k_{max}}(cos\theta) \tag{2.8}$$

where $0 \leq k \leq \min(2I_2, 2L_1, 2L_2)$, namely the selection rules for k. These selection rules follow directly from the invariance of the correlation processes under rotation and inversion. In other words, γ-ray emission symmetric about a plane normal to the quantization axis is the reason of this result. The index k is an even integer as long as one does not measure linear polarizations of γ radiation.

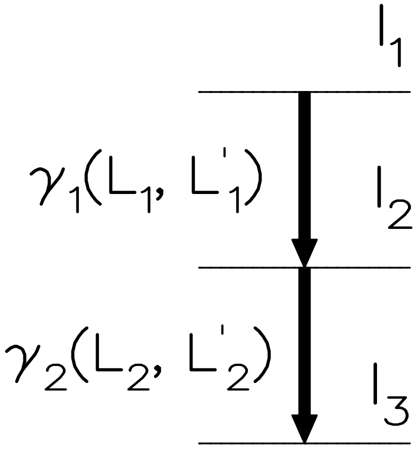

Figure 2.1: A schematic drawing for two successive γ-ray transitions in a cascade.

The $A_k(\gamma)$ coefficients depend on the multipole nature of the transitions and the product $A_k(\gamma_1)A_k(\gamma_2)$ is written as $A_k(\delta_1, \delta_2)$ [3], where

$$\begin{aligned} A_k(\delta_1, \delta_2) = & \frac{1}{1+\delta_1^2}\Big[F_k(L_1L_1I_1I_2) + (-1)^{(L_1-L_1')}2\delta_1 F_k(L_1L_1'I_1I_2) + \delta_1^2 F_k(L_1'L_1'I_1I_2)\Big] \\ & \times \frac{1}{1+\delta_2^2}\Big[F_k(L_2L_2I_3I_2) + 2\delta_2 F_k(L_2L_2'I_3I_2) + \delta_2^2 F_k(L_2'L_2'I_3I_2)\Big], \end{aligned} \tag{2.9}$$

The mixing ratios δ_1 and δ_2 are defined as the ratio of the corresponding reduced matrix elements

$$\delta_1 = \frac{< I_2 \parallel \mathscr{M}(E/ML_1') \parallel I_1 >}{< I_2 \parallel \mathscr{M}(M/EL_1) \parallel I_1 >}, \tag{2.10}$$

and

$$\delta_2 = \frac{< I_3 \parallel \mathscr{M}(E/ML_2') \parallel I_2 >}{< I_3 \parallel \mathscr{M}(M/EL_2) \parallel I_2 >} \tag{2.11}$$

respectively, and F_k is defined as [4]

$$F_k(LL'I_iI) = (-1)^{I_i+I-1}\Big[(2L+1)(2L'+1)(2I+1)(2k+1)\Big]^{\frac{1}{2}}\begin{pmatrix} L & L' & k \\ 1 & -1 & 0 \end{pmatrix}\begin{pmatrix} L & L' & k \\ I & I & I_i \end{pmatrix}. \tag{2.12}$$

L_1' and L_2' are used to describe possible multipole mixtures in γ_1 and γ_2, respectively. If one transition is mixed, one usually obtain a multipole mixture of orders 2^L and $2^{L'}$. Conservation of parity results in one being magnetic, the other electric. Note that $L_1' = L_1 + 1$ and $L_2' = L_2 + 1$ are chosen based on the relative intensities of various multipoles in Eqs. (2.6) and (2.7). In other words, only the multipole with the angular momentum one unit larger than L is taken into account in theoretical calculations and in experimental analysis.

In most cases, we need to consider only the first three terms in Eq. (2.8), which means that

$$W(\theta) = 1 + A_2(\delta)P_2(cos\theta) + A_4(\delta)P_4(cos\theta). \tag{2.13}$$

In Eq. (2.13), it is implied that one of the transitions is of pure multipole and δ is that of the mixed transition. The theoretical values for a pure quadrupole → quadrupole cascade ($L_1 = 2$, $L_2 = 2$ and $\delta_1 = 0$, $\delta_2 = 0$) are A_2=0.102 and A_4=0.009. Theoretical values for different spin sequences have been tabulated in Refs. [3, 5]. By comparing the experimentally measured A_2 and A_4 values with the theoretical ones, one is able to determine the angular momenta carried away by one of the transitions of interest, provided one knows the spins I_1, I_2, and/or I_3. It is worth pointing out that angular correlations can only give the L values carried away by the transitions in the correlation, but cannot tell the electric or magnetic multipoles. In other words, angular correlation measurements can be used to assign spins to states of interest, rather than their parities. However, one is still able to establish parities of levels of interest, by knowing other nuclear properties. In addition, angular correlations also provide an approach to determine the $E2/M1$ mixing ratio of a transition between two states with $\Delta I = 1$ ($I_1 - I_2 = 1$) and like parity, and the g-factor of the state with a "long" lifetime, which are measured and compared with theory in Chapter V and VI, respectively. More explicit introduction for the $E2/M1$ mixing ratio and g-factor will be given in the following.

A transition between two states with $\Delta I = 1$ and like parity is expected to have a multipolarity of $M1$, $E2$, or $M3$, and so on. By taking the relative intensities of multipoles into account, one can conclude that only the lowest two multipolarities dominate in this transition. Therefore, this transition can be of mixed $E2/M1$ character. The square of the $E2/M1$ mixing ratio is defined as the ratio of the transition probabilities $T(E2; I_1 \rightarrow I_2)$ and $T(M1; I_1 \rightarrow I_2)$ for an $E2$ and $M1$ transition, respectively, in the form of

$$\delta^2(E2/M1; I_1 \rightarrow I_2) = \frac{T(E2; I_1 \rightarrow I_2)}{T(M1; I_1 \rightarrow I_2)}. \tag{2.14}$$

The sign convention chosen in the present work is from Ref. [6], where the initial state of the transition is written on the right side in the reduced matrix elements. Thus, the mixing ratio is given by the corresponding $E2$ and $M1$ matrix elements as

$$\delta(E2/M1; I_1 \rightarrow I_2) = 0.835 E_\gamma \frac{< I_2 \parallel \mathscr{M}(E2) \parallel I_1 >}{< I_2 \parallel \mathscr{M}(M1) \parallel I_1 >}, \tag{2.15}$$

where E_γ is in MeV. From Eq. (2.15), one clearly sees that the mixing ratio is a measure of the ratio of the $E2$ and $M1$ transition matrix elements, which are related to the electric quadrupole operator and the magnetic dipole operator, respectively. So, the mixing ratio can give information about both electric and magnetic properties of a nucleus.

There are two nuclear quantities that can be easily accessible to being measured, namely, the magnetic dipole moment and the electric quadrupole moment. They represent the lowest non-trivial electric and magnetic multipoles in γ radiation, because the electric monopole is the nuclear charge and the electric dipole moment and the magnetic monopole moment probably vanish.

The magnetic dipole moment μ of a nucleus is an important quantity to describe the magnetic properties of a nucleus. The scale of the nuclear magnetism is the nuclear magneton, $\mu_{\mathrm{N}} = 0.315$ MeV/T. The magnetic moment of a nucleus is quite small and somewhat difficult to obtain directly. If a very strong magnetic field is applied to a nucleus, one may be able to measure its interaction with this nucleus and then know the magnetic dipole moment in this nucleus. In general, the g-factor, a dimensionless quantity used to evaluate the magnetic moments for different nuclear states, is defined as

$$g = \frac{\mu}{\mu_{\mathrm{N}} I} \tag{2.16}$$

where I is the spin value of the state of interest. The magnetic dipole moment of a nucleus has two distinct origins. One is the motion of charges within a nucleus. The g-factor of this origin can be referred to as the orbital g-factor. The other is the intrinsic magnetic moment of each nucleon related to its intrinsic spin motion. This is sometimes called the intrinsic-spin magnetic moment. Theoretical g-factor values can be predicted with different nuclear models for various mass regions.

The electric quadrupole moment Q_0 of a nucleus is a parameter to describes the effective shape of the ellipsoid of nuclear charge distribution. A non-zero quadrupole moment Q_0 indicates that the charge distribution is not spherically symmetric and the nucleus is deformed. More information about the nuclear deformed shapes and their relationship with the electric quadrupole moment will be given in Section 2.3.

A classical definition of the nuclear electric quadrupole moment is given by

$$Q_0 = \int \rho(3z^2 - r^2)\mathrm{d}V. \tag{2.17}$$

Electric quadrupole moments of nuclei can be measured from hyperfine splitting of atomic spectral lines, quadrupole hyperfine splitting of molecular rotational spectra, and other spectroscopic techniques.

It is worth mentioning that another nuclear deexcitation process competing with the γ-ray emission is the so-called internal conversion (IC). The internal conversion occurs when a nucleus in an excited state transfers some of its "excess" energy to an atomic electron to knock it out. It is a one step, direct process due to the overlap of wave functions of atomic electrons and the nucleus. The total internal conversion coefficient (ICC) of a transition is a very useful quantity to determine its multipolarity, defined as

$$\alpha_{\mathrm{T}} = \frac{T_e}{T_\gamma}, \tag{2.18}$$

where T_e and T_γ are the decay probabilities for the internal conversion and the γ-ray, respectively. Theoretical methods have been developed to predict α_{T} values for transitions of different energies in various nuclei. We use the BrIcc Conversion Coefficient Calculator [7] to obtain theoretical α_{T} values for different possible multipolarities in the present work.

2.1.2 Spontaneous fission

Spontaneous fission is a process in which a single heavy nucleus spontaneously splits into two or more smaller fragments with free neutrons. The process occurs mainly in heavy nuclei and is the direct result of competition between the attractive nuclear force and the Coulomb repulsion. One important spontaneous fission source is ${}^{252}_{98}\mathrm{Cf}$, which has a half-life of 2.645(8) years.

The energy to hold a ${}^{252}_{98}\mathrm{Cf}$ nucleus, so-called the binding energy, is approximately equal to the difference between the measured mass of ${}^{252}\mathrm{Cf}$ and the total mass of 98 protons and 154 neutrons. The binary spontaneous fission of a ${}^{252}\mathrm{Cf}$ nucleus is able to release an energy of $\approx$ 200 MeV. Besides the spontaneous fission process, the α decay is the dominant deexcitation mechanism for ${}^{252}\mathrm{Cf}$. The α-decay process can liberate an energy of $\approx$ 6 MeV. The preference for the α decay over the spontaneous fission manifests itself in the fact that the α decay branch occurs in 97% of the decay while the spontaneous fission branch is only 3%. These two competing processes are shown in Fig. 2.2.

The formation of states at high spin in the spontaneous fission process has been studied theoretically. We can estimate the max limit of the spin value as $I_{\mathrm{max}} = 36\hbar$. More information about the calculations can be found in Ref. [9]. This value is well beyond the highest value observed in our experiments about $22\hbar$. The possible reason is that these highest-spin states have much lower population in the spontaneous fission of ${}^{252}\mathrm{Cf}$. So, it is quite difficult to observe them.

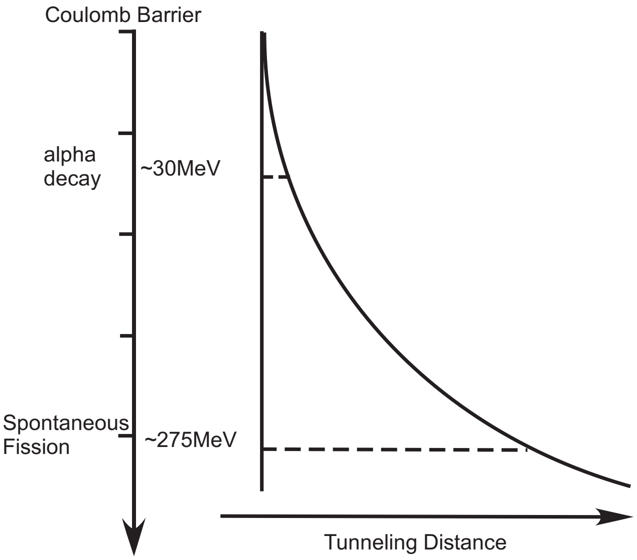

Figure 2.2: Relative potential-energy barrier widths for the processes of the spontaneous fission and α decay in ^{252}Cf. Taken from Ref. [8]

2.2 Nuclear models

Many different models have been proposed to interpret experimental phenomena in nuclear physics. Roughly, these models can be classified into two main types: the shell model and the collective model, which describe single nucleon motions and collective motions of nucleons in a specific nucleus, respectively. We will briefly describe the shell model, the collective model and a hybrid model, named as the unified model.

2.2.1 The shell model

The spherical shell model was first introduced by Mayer and Jensen [10]. Evidence of the existence of nuclear shells has been observed experimentally in many aspects, such as nuclide abundance, neutron and proton separation energies, and the α-decay energies. For example, sudden drops are seen in neutron and proton separation energies at certain numbers of neutrons or protons, like 50, 82, 126 for neutrons. These numbers are known as magic numbers. The first job was to find an appropriate potential that would reproduce these corresponding magic numbers correctly. This goal was not fulfilled until Mayer and separately Jensen found that the proper potential like the harmonic oscillator potential must include the spin-orbit interaction, a term of $\hat{l} \cdot \hat{s}$ with the opposite sign and much larger magnitude than the spin-orbit interaction of electrons in atoms. A realistic finite potential, the Woods-Saxon potential, with spin-orbit coupling is widely used in the form of [11]

$$U(r) = \frac{U_0}{1+\exp[(r-R_0)/a]} + \frac{U_{ls}}{r_0}\frac{1}{r}\frac{\mathrm{d}}{\mathrm{d}r}\left\{\frac{1}{1+\exp[(r-R_0)/a]}\right\}\hat{l}\cdot\hat{s}. \tag{2.19}$$

A typical set of parameters is $U_0 = [-51 + 33(N-Z)/A]$ MeV, $U_{ls} = -0.44U_0$, $a = 0.67$ fm, and $R_0 = r_0 A^{1/3}$ with $r_0 = 1.27$ fm. The spin-orbit interaction results in individual energy levels to split in such a way that at magic numbers, 2, 8, 20, 28, 50, 82, 126, are large gaps in the energy spacings. It is easy to understand that nuclei in the shell model have a spherical shape.

Besides its ideal reproduction of magic numbers, the shell model has been used to successfully interpret nuclear properties in more ways than one, such as the magnetic dipole moments, the electric quadrupole moments, the spin-parity assignments of ground states of odd-A nuclei, the isomer distributions, and the γ-ray transition probabilities. The strictest version of the shell model is the extreme single particle shell model, which assumes the "seniority rule" [12] that *two by two particles of the same kind pair off to angular momentum zero* and only the last odd nucleon outside the closed shells has a spin different from zero and is considered to contribute to the spin-parity of the ground state. Although this interpretation is an oversimplification somewhat, its predictions hold true in many cases. Let us take ^{57}Ni, with one neutron outside the doubly-magic core ^{56}Ni ($Z = 28, N = 28$), for an example. According to the extreme single particle shell model, the last neutron in the $p_{3/2}$ orbital should give a spin of 3/2 to the ground state, which turns out to be correct experimentally.

The shell model can also be used to predict and interpret excited states as well. Excited states are often calculated by considering nucleons outside a specific magic or doubly-magic core as single particles. It is assumed that nucleons up to the closed major shells or sub-shells are too tightly bound to contribute to nuclear excitations.

One interesting region for the shell model is beyond the doubly-magic core ^{132}Sn which has $Z = 50$ and $N = 82$. Many computer codes have been developed in the shell-model framework to interpret the nuclear structure of nuclei in this region. In the previous work of our group, realistic shell-model calculations with a two-body effective interaction derived from the CD-Bonn nucleon-nucleon potential were carried out for ^{137}Cs ($Z = 55$, $N = 82$) and ^{138}Cs ($Z = 55$, $N = 83$) and reproduced their experimental level patterns very well [13]. For ^{134}Te with two protons and ^{135}I with three protons outside the ^{132}Sn core, the values of the g-factors for levels predicted by the shell-model calculations were very consistent with the measured values [14]. As presented in Chapter V and VI, shell-model calculations are used to interpret the nuclear structures of a few neutron-rich nuclei beyond ^{132}Sn. More details will be given then.

However, despite its success, the shell model still has some limitations because it simply treats nucleons as independent particles, moving in a spherical mean potential produced by themselves. Even after including the pairing effect, the residual interaction and the possibilities of the configuration mixture, the shell model still cannot predict or interpret some features and phenomena of nuclei, such as larger quadrupole moments observed in nuclei far away from magic numbers, and certain distinguishing properties in low-energy excitations or high-energy excitations, which brings in the next two nuclear models.

2.2.2 The collective model

Many features of nuclei indicate that the nuclear motion does not consist of only the simple single particle excitations. Instead, there are a few typical effects that imply a collective motion, where all or at least a large part of nucleons in a nucleus move coherently with well-defined phases. Nearly all nuclei with neutron numbers at mid shell between two major magic numbers show some degree of collective behaviors. Two important types of the collective motions are the surface vibration of the nuclear shape that is a motion of nucleons from one region of the nuclear sphere to another one and the rotation of the entire nucleus. The first step of the collective model was made by Bohr and Mottelson in the 1950s. One important Hamiltonian of a collective motion including vibrational motions, rotational motions and their interactions (namely the rotation-vibration model) is given by [15]

$$\hat{H}_{\text{coll}} = \hat{H}_{\text{rot}} + \hat{H}_{\text{vib}} + \hat{H}_{\text{vib rot}}. \tag{2.20}$$

In even-even nuclei, strong indicators for the collectively rotational motions are, for example, the ratios of the lowest 4^+ to 2^+ state energies and the large 2^+ state electric quadrupole moments. Evidence of the rotational and vibrational motions is shown in Fig. 2.3, where the ratios of the first 4^+ to 2^+ level energies are shown.

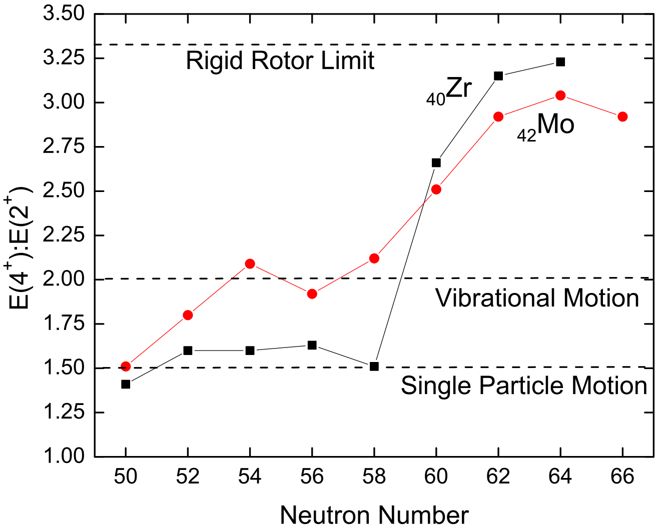

Figure 2.3: $E(4^+)$: $E(2^+)$ of yrast bands of even-even Zr and Mo isotopes.

In the collective model, the collective g-factor values for the excited states in rotational odd-even nuclei can be predicted simply as $g = Z/A$, while $g = 0.5Z/A$ is taken for even-odd nuclei [16]. Many states in rotational odd-A nuclei agree with these simple estimates.

It should be pointed out that the introduction of collective motions is definitely not to be treated as standing in opposition to the shell model. In fact, the mean field for the independent particles is of collective nature, essentially. This was clearly revealed by Nilsson [17] in 1955, who extended the spherical shell model to deformed nuclei that have shapes different from a sphere.

2.2.3 The unified model

In the above statements, it becomes clear that coherence in the nuclear single particle motion results in collective effects in some mass regions. That means the shell model and the collective model are, in fact, closely related. If we discuss the single particle motion and the collective motion simultaneously, the Hamiltonian of the entire nucleus will therefore be in the form of [15]

$$\hat{H} = \hat{H}_{\mathrm{coll}} + \hat{H}_{\mathrm{sp}} + \hat{H}_{\mathrm{int}} \tag{2.21}$$

where $\hat{H}_{\mathrm{coll}}$ is from Eq. (2.20), $\hat{H}_{\mathrm{sp}}$ is the Hamiltonian of the single particle and $\hat{H}_{\mathrm{int}}$ stands for the interaction between the single particle motion and the collective motion.

At the same time, the nucleus seems to have a deformed shape that is given, in a quantitative way, by the large values of the intrinsic electric quadrupole moments. That is because many protons in the nucleus can give a large value of the electric quadrupole moment if this nucleus has a permanent non-spherical shape. Thus, the deformed potential was introduced to solve the Hamiltonian of the single particle motion by Nilsson. The deformed potential that Nilsson chose was named as the Nilsson potential, in the form of [15]

$$V_{\mathrm{Nilsson}} = V_{\mathrm{h}} - C\hat{s} \cdot \hat{l} - D\hat{l}^2 \tag{2.22}$$

where V_h is the harmonic oscillator potential. Therefore, the deformed single particle Hamiltonian $\hat{H}_\mathrm{sp}$ becomes

$$\hat{H}_\mathrm{sp} = \frac{\hat{p}^2}{2M} + V_\mathrm{h} - C\hat{s}\cdot\hat{l} - D\hat{l}^2. \tag{2.23}$$

Nilsson chose the so-called asymptotic quantum numbers $[N, n_z, \Lambda, \Sigma]\Omega^\pi$ to describe the single particle orbitals in the deformed potential. N is the the principal quantum number of the major shell; n_z is the number of nodes in the wave function along the z axis that refers to the symmetry axis; Λ represents the projection of the orbital angular momentum l on the symmetry axis; Σ gives the projection of the spin s on the symmetry axis; Ω denotes the projection of the single particle angular momentum $j = l + s$ on the symmetry axis; π is the parity and defined as $\pi = (-1)^l$. Since one knows that $\Sigma = \pm 1/2$, $[N, n_z, \Lambda]\Omega^\pi$ is sufficient for the deformed single particle orbitals, where only Ω and π are good quantum numbers. However, the other three quantum numbers, N, n_z, and Λ, become good quantum numbers at large deformations and therefore are called asymptotic quantum numbers. The energy levels of a single particle moving in a deformed potential given by Nilsson in $[N, n_z, \Lambda]\Omega^\pi$ succeeded in interpreting and describing the ground states and excited states in nuclei with deformation.

After the introduction of the Nilsson deformed potential for the single particle motion, the Hamiltonian in Eq. (2.21) has the ability to predict the properties of nuclei in various mass regions with different shapes. That is the unified nuclear model. One important prediction of the unified theory of the collective rotation, collective vibration and single particle motion is the existence of γ-vibrational bands, which have been observed in Nb, Mo and Ru isotopes for example and other regions.

The major purpose of the present work is to discover the nuclear features of high-spin states in neutron-rich nuclei. In the mass regions where nuclei have large deformations, many exotic phenomena have been observed, such as prolate or oblate shapes, triaxiality, the backbending phenomenon, octupole deformations/correlations, chiral doublet bands. Many models, including the particle-plus-axial-rotor model and the triaxial-rotor-plus-particle model in the particle-plus-rotor-model framework, and the Interacting Boson Model (IBM), have been developed and utilized to interpret the above phenomena with partial success. In the present work as discussed in Chapter IV, calculations based on the rigid-triaxial-rotor-plus-quasiparticle model confirm the existence of triaxiality in ^{115}Rh which is observed experimentally.

For odd-A nuclei with deformation where the rotational collectivity is predominant, nuclear models in the particle-plus-rotor-model framework are able to explain their properties very well. The physics picture of this model framework can be described as a few valence particles moving more or less independently in the deformed potential of the core coupled to the collectively rotational core that stands for all the paired particles.

It is known that only a deformed nucleus can rotate collectively, and the only possible rotational axis is perpendicular to the symmetry axis, if the nucleus is axially symmetric. For the collective rotation, it is then possible to define the kinetic moment of inertia, $\mathscr{J}$, resulting in the following Hamiltonian as

$$H_{\text{rot}} = \frac{\boldsymbol{R}^2}{2\mathscr{J}} \tag{2.24}$$

where $\boldsymbol{R}$ is the collective angular momentum. For the pure collective rotation in even-even nuclei, the total angular momentum (the total spin) $\boldsymbol{I}$ is equal to $\boldsymbol{R}$, which leads to the level energy with the spin I in the form of

$$E(I) = \frac{\hbar^2}{2\mathscr{J}} I(I+1). \tag{2.25}$$

Pure rotational bands are essentially never seen in nuclei in practice because rotational and vibrational collectivity is more or less mixed. The kinetic moment of inertia can be extracted from experimental rotational bands. The experimental values of $\mathscr{J}$ are generally 25-50% of the rigid body value. The method to extract the kinetic moment of inertia experimentally will be given next.

For an odd-A nucleus, the specific features of its low-energy states are determined by the orbitals occupied by the odd nucleon. For these orbitals in an axially symmetric, deformed potential, only the parity and the projection of the single particle angular momentum $\boldsymbol{j}$ on the symmetry axis, namely Ω, are good quantum numbers. If the rotational axis is perpendicular to the symmetry axis, the collective rotational angular momentum has no component on the symmetry axis. As shown in Fig. 2.4 where the z-axis is chosen as the symmetry axis, the total spin $\boldsymbol{I}$ is the sum of the single particle spin $\boldsymbol{j}$ and the collective angular momentum $\boldsymbol{R}$ of the core rotor.

Then, the collectively rotational energy of an axially symmetric nucleus around an axis perpendicular to the z-axis can be calculated from

$$\begin{aligned} H_{\text{rot}} =& \frac{\boldsymbol{R}^2}{2\mathscr{J}} = \frac{(\boldsymbol{I}-\boldsymbol{j})^2}{2\mathscr{J}} = \frac{1}{2\mathscr{J}}\left[(I_x - j_x)^2 + (I_y - j_y)^2\right] \\ =& \frac{1}{2\mathscr{J}}\left[(\boldsymbol{I}^2 - I_z^2) + (j_x^2 + j_y^2) - (I_x j_x + I_y j_y)\right]. \end{aligned} \tag{2.26}$$

The recoil term $(j_x^2 + j_y^2)$ is constant for a rotational band. The term $(I_x j_x + I_y j_y)$, which can be expressed as $(I_+ j_- + I_- j_+)$, corresponds classically to the Coriolis force, which results in a coupling between the single particle motion and the collective rotation. These terms in Eq. (2.26) are of different importance in different situations. Thus, it is useful to consider three limits where one of these terms is predominant and can consequently be solved. In the strong coupling limit, the single particle adiabatically follows the rotation of the core and the coupling to the deformation is much stronger than the perturbation caused by the Coriolis interaction. In the weak coupling limit, the nuclear deformation is very small and the single particle essentially moves in the spherical shells with a slight perturbation (for example, from the quadrupole vibration). In the decoupling limit, the Coriolis force is so strong that the coupling to the deformation can be neglected, and $\boldsymbol{R}$ is parallel to $\boldsymbol{j}$ each other. In the following text, we only focus on the first limit, the strong coupling limit, which is also called deformation alignment.

In the strong coupling limit, one sees that the projection of the total spin on the z-axis, K, is a good quantum number and is equal to Ω, as shown in Fig. 2.4. For small I, it is justified to assume that the Coriolis interaction is small and only its

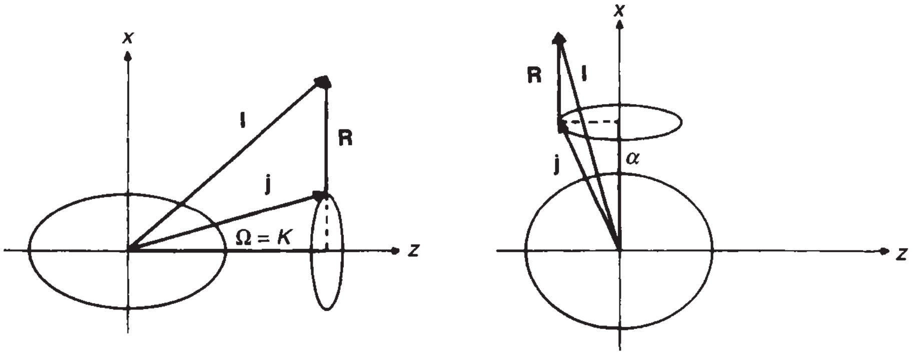

Figure 2.4: Illustration of two extreme coupling schemes, the strong coupling limit (left figure) and the decoupling limit (right figure). Taken from Ref. [18]

diagonal contributions need to be considered. The diagonal matrix elements of the Coriolis interaction are not equal to zero only for $K = \frac{1}{2}$. Thus, one can obtain the level energy in a rotational band as

$$E(I, K) = E_{\rm sp} + \frac{1}{2\mathscr{J}}[I(I+1) - K^2] \qquad (K \neq \frac{1}{2}), \tag{2.27}$$

where $E_{\rm sp}$ is the eigenvalue of the single particle Hamiltonian, for example, as given in Eq. (2.23). In Eq. (2.27), the Coriolis interaction is completely neglected. For $I > K$, the spins $I = K,\ K+1,\ K+2,\ \cdots$ are observed experimentally to form $\Delta I = 1$ rotational bands. For rotational bands with $K = \frac{1}{2}$ where the Coriolis effect cannot be neglected, the expression of the level energy is given by

$$E(I, K = \frac{1}{2}) = E_{\rm sp} + \frac{1}{2\mathscr{J}}\Big[I(I+1) - \frac{1}{4} + a(-1)^{I+\frac{1}{2}}\Big(I + \frac{1}{2}\Big)\Big], \tag{2.28}$$

where a is the so-called decoupling parameter.

At large spins, K is no longer a good quantum number because of K mixing caused by the Coriolis interaction, but the parity is still preserved. A new good quantum number was introduced to describe the invariance of the Hamiltonian with respect to the rotation about the rotational axis by π. It is named as the signature quantum number, α. Without going into details, we need to mention the α values for odd- and even-A nuclei. For odd-A nuclei, α can have the values of $+\frac{1}{2}$ and $-\frac{1}{2}$. The states in rotational bands with $\alpha = +\frac{1}{2}$ have spin sequences of $\frac{1}{2}$, $\frac{5}{2}$, $\frac{9}{2}$, $\frac{13}{2}$, $\cdots$, while spin sequences with $\alpha = -\frac{1}{2}$ are $\frac{3}{2}$, $\frac{7}{2}$, $\frac{11}{2}$, $\frac{15}{2}$, $\cdots$. For even-A nuclei, α can have the values of 0 and 1, with spin sequences 0, 2, 4, 6, $\cdots$ and 1, 3, 5 ,7, $\cdots$, respectively. The band-heads of rotational bands may have any spin in the corresponding sequences.

In high-spin studies, the relationship between the kinetic moment of inertia and the rotational frequency is very important to interpret the phenomenon of back-bending. The rotational frequency is defined by

$$\omega = \frac{\mathrm{d}E(I)}{\hbar \mathrm{d}I_x}, \tag{2.29}$$

where $E(I)$ is the rotational energy and I_x is the component of the total spin $\boldsymbol{I}$ in the rotational axis, $x-$axis. An approximation is used widely in the form of

$$\hbar\omega = \frac{1}{2}E_\gamma(I+1 \rightarrow I-1). \tag{2.30}$$

According to Eq. (2.24), the kinetic moment of inertia can be obtained by

$$\frac{\hbar^2}{\mathscr{J}} = 2\frac{\mathrm{d}E(I)}{\mathrm{d}I^2}. \tag{2.31}$$

It is also not difficult to derive an often-used approximation for the kinetic moment of inertia in the form of

$$\mathscr{J} = \frac{\hbar^2(2I+1)}{E_\gamma(I+1 \to I-1)}. \tag{2.32}$$

From Eqs. (2.30) and (2.32), one can obtain the rotational frequency and the kinetic moment of inertia from the experimental level energies, $E_\gamma(I+1 \to I-1) = E(I+1) - E(I-1)$. These two qualities will be used in Chapter IV to discuss the the phenomenon of back-bending.

2.3 Nuclear shapes

From the above introduction, it is obvious that nuclei in different mass regions have different shapes. For example, the doubly-magic nuclei have a spherical shape, but those far from the closed shells are expected to have deformed shapes. The coexistence of spherical and deformed shapes in the same nucleus and different deformed shapes in a nucleus has been well established [19–21].

The nuclear shapes can be described in terms of an expansion of the radius vector from the origin to the nuclear surface in a series of spherical harmonics, in the form of

$$R(\theta,\phi) = R_0\Big[1 + \sum_{\lambda=0}^{\infty}\sum_{\mu=-\lambda}^{\lambda} \alpha_{\lambda\mu} Y_{\lambda\mu}(\theta,\phi)\Big] \tag{2.33}$$

where R_0 is the radius of a sphere with the same volume, and θ and ϕ are the polar angles with respect to an arbitrary coordinate set. By the requirement of volume conservation, α_{00} is expected to be zero, which corresponds to a spherical shape. For $\lambda = 1$, it describes the translation of the system as a whole, so $\alpha_{1\mu} = 0$. The non-trivial lowest order is $\lambda = 2$, which is related to quadruple deformations. Evidence for higher-order deformations, for example, $\lambda = 3$ for octupole deformations and $\lambda = 4$ for hexadecapole deformations, has been observed. Note that many of the coefficients $\alpha_{\lambda\mu}$ vanish when symmetries are present, for example, $\alpha_{\lambda\mu\neq 0}$ if there is axial symmetry and $\alpha_{\mathrm{odd}-\lambda\mu}$ if the nucleus has reflection symmetry.

For $\lambda = 2$, Eq. (2.33) can be rewritten as

$$R(\theta, \phi) = R_0\Big[1 + \sum_{\mu=-2}^{2} \alpha_{2\mu} Y_{2\mu}(\theta, \phi)\Big]. \tag{2.34}$$

Two of these five variables $\alpha_{2\mu}$ ($\mu = -2, -1, 0, 1, 2$) vanish and the rest correspond to the Euler angles in the laboratory frame. That is, $\alpha_{21} = \alpha_{2-1} = 0$, $\alpha_{22} = \alpha_{2-2}$, and α_{20} is independent. Thus, Eq. (2.34) becomes

$$R(\theta, \phi) = R_0\Big\{1 + \alpha_{20} Y_{20}(\theta, \phi) + \alpha_{22}\big[Y_{22}(\theta, \phi) + Y_{2-2}(\theta, \phi)\big]\Big\}. \tag{2.35}$$

In general, the physical picture of the system is more conveniently expressed in terms of two variables β_2 and γ for α_{20} and α_{22}, where

$$\alpha_{20} = \beta_2 \cos\gamma, \tag{2.36}$$

and

$$\alpha_{22} = \frac{1}{\sqrt{2}} \beta_2 \sin\gamma. \tag{2.37}$$

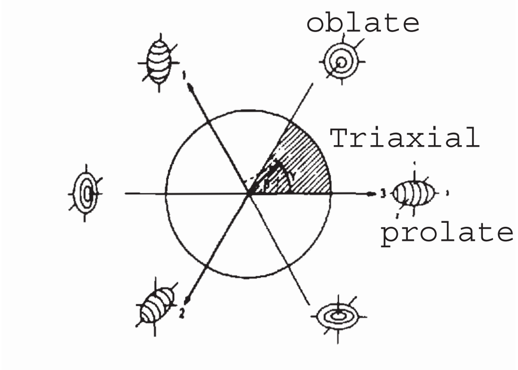

Figure 2.5: Various nuclear shapes in the (β_2, γ) plane. Taken from Ref. [11].

It is obvious that

$$\sum_{\mu} \alpha_{2\mu}^2 = \beta_2^2. \tag{2.38}$$

Therefore, the parameter β_2, related to the quadrupole deformation, is a measure of the deviation of the nuclear shape from sphere. The larger β_2 is, the more quadrupole deformation a nucleus has. Since $\alpha_{22} = \frac{1}{\sqrt{2}}\beta_2 \sin\gamma$ vanishes for the axially symmetric quadrupole deformation, the parameter γ describes the departure from axial symmetry. Further, for axially symmetric shapes, the only remaining $\alpha_{\lambda 0}$ can be simplified as $\alpha_{\lambda 0} = \beta_\lambda$. Without going into details, it is known that in the (β_2, γ) plane $\gamma = 0 - 60°$ is sufficient to describe all ellipsoidal shapes. The different 60° sectors only correspond to a different labeling of the three principal axes. The z-axis is chosen as the symmetry axis here. The nucleus is a prolate ellipsoid for $\gamma = 0°$ or an oblate ellipsoid for $\gamma = 60°$. If $0° < \gamma < 60°$, the nucleus is expected to be triaxial with maximum triaxiality at $\gamma = 30°$. The observation of nearly maximum triaxiality in ^{115}Rh will be presented in Chapter IV. Figure 2.5 gives a straightforward illustration of the nuclear shapes related to the different γ sectors.

Note that some literature do not introduce the parameter γ, but assume that the parameter β can be either positive or negative for axially symmetric nuclei. In this case, the positive β corresponds to prolate while the negative to oblate. In addition, one can obtain the relationship between β and the electric quadrupole moment in quadrupole deformations as

$$Q_0 \approx \frac{3}{\sqrt{5\pi}} eZR_0^2\beta. \tag{2.39}$$

Therefore, the nucleus is prolate (or oblate) if its Q_0 is positive (or negative).

The Q_0 is called the intrinsic electric quadrupole moment, to differentiate the experimental (or laboratory) electric quadrupole moment Q, which can be measured experimentally. In the unified model, the relationship between these quantities is expressed as

$$Q(I) = \frac{3K^2 - I(I+1)}{(I+1)(2I+3)} Q_0 \tag{2.40}$$

for different levels with spins I. The Q_0 can be derived form the $B(E2)$ value by

$$Q_0 = \left[\frac{16\pi}{5} B(E2)\right]^{\frac{1}{2}}. \tag{2.41}$$

Another interesting shape is related to the reflection asymmetry where the coefficients $\alpha_{\lambda\mu}$ with odd-λ do not vanish. The lowest order of λ for this case is $\lambda = 3$, which corresponds to octupole shapes. Soon after the nuclear collective model was established, low-lying, negative-parity states were observed in even-even Ra and Th nuclei, where these negative-parity states form bands with spin-parity sequences 1^-, 3^-, 5^-, $\cdots$. The K quantum number of these bands was found to be $K = 0$. Along with

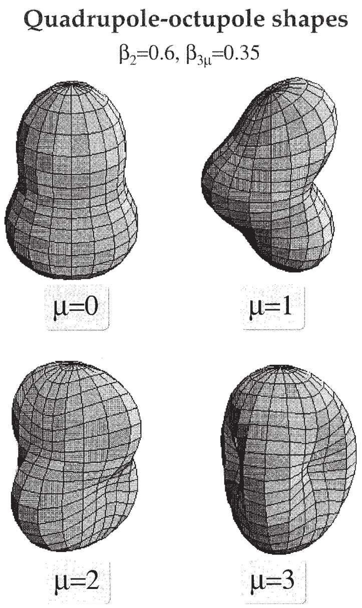

Figure 2.6: Quadrupole-octupole shapes. In all cases, the same axial quadrupole deformation β_2=0.6 is assumed. The four shapes correspond to octupole deformations with $\mu = 0$, 1, 2, and 3. Taken from Ref. [23].

the fact that their energies are much lower than those expected for two-quasiparticle states, they were interpreted as octupole vibrations about a spheroidal equilibrium shape. Since then, theoretical efforts have been made as regards the possibility of octupole deformations in nuclei through many approaches. The tendency towards reflection asymmetric shapes can be associated with the maximum $\Delta N = 3$ octupole coupling between the intruder sub-shell (l, j) and the nearby normal-parity sub-shell ($l - 3$, $j - 3$). One mass region with strong octupole deformations/correlations is related to $Z = 56$ ($h_{11/2} \leftrightarrow d_{5/2}$ coupling) and $N = 88$ ($i_{13/2} \leftrightarrow f_{7/2}$ coupling) as theoretically predicted [22] and is one topic of interest in the present work discussed in Chapter VII. A few examples of nuclear shapes with $\lambda = 3$ are shown in Fig. 2.6.

The nuclear electric dipole moment $\boldsymbol{D}$ is used to measure the shift between the center of charge and the center of mass of the nucleus. For a reflection symmetric nucleus, it is equal to zero. However, a large static $\boldsymbol{D}$ may arise in a reflection asymmetric system. Here, we use D_0 because the discussion is restricted to an axially symmetric system, where the other two components vanish. Assuming the strong-coupling limit and axial shape, there is a simple, approximate relationship between D_0 and Q_0

$$D_0 = \sqrt{5B(E1)/16B(E2)} \times Q_0, \tag{2.42}$$

because both the ratio of $B(E1)$ and $B(E2)$ and Q_0 are easily measured experimentally. The D_0 is a very important quantity in the studies of nuclear structure related octupole deformations/correlations. More information will be given in Chapter VII.

A new quantum number needs to be introduced for a reflection asymmetric system, namely the simplex quantum number, s. Simplex has properties similar to those of the signature quantum number. Without going into details, one obtains two sets of doublet bands with the spin-parities as

$$s = +1, I^{\pi} = 0^{+}, 1^{-}, 2^{+}, 3^{-}, \cdots \qquad \text{and} \qquad s = -1, I^{\pi} = 0^{-}, 1^{+}, 2^{-}, 3^{+}, \cdots \tag{2.43}$$

for reflection asymmetric, even-A nuclei, and

$$s = +i, I^{\pi} = \left(\frac{1}{2}\right)^{+}, \left(\frac{3}{2}\right)^{-}, \left(\frac{5}{2}\right)^{+}, \cdots \quad \text{and} \quad s = -i, I^{\pi} = \left(\frac{1}{2}\right)^{-}, \left(\frac{3}{2}\right)^{+}, \left(\frac{5}{2}\right)^{-}, \cdots \tag{2.44}$$

for reflection asymmetric, odd-A nuclei.

CHAPTER III

EXPERIMENTAL TECHNIQUES

In this chapter, a few topics of experimental technique that are related to the current experiments are addressed.

3.1 The spontaneous fission of ^{252}Cf

Many nuclear properties have been known by investigating γ-rays emitted from nuclei in excited states. There are several methods to produce nuclei in excited states. One way is the β decay of a nucleus to populate excited states in its daughter nucleus. However, only low-lying levels are populated through the β decay. In order to study high-spin structures of nuclei, nuclei can be produced in heavy-ion induced reactions. However, nuclei produced via reactions of that kind are proton-rich but not neutron-rich (less or more neutrons, respectively, than the stable isotopes of the element). Neutron-rich, especially very neutron-rich nuclei are quite difficult to populate, especially in high-spin states. The current major way to produce neutron-rich nuclei is through the fission process, either the induced fusion-fission or the spontaneous fission of some very heavy isotopes. Therefore, studies of nuclei from the spontaneous fission process provide a key approach to know the structures of neutron-rich nuclei.

Two spontaneous fission sources have been used to study neutron-rich nuclei. They are ^{248}Cm and ^{252}Cf [24]. The present work is obtained by examining the experimental

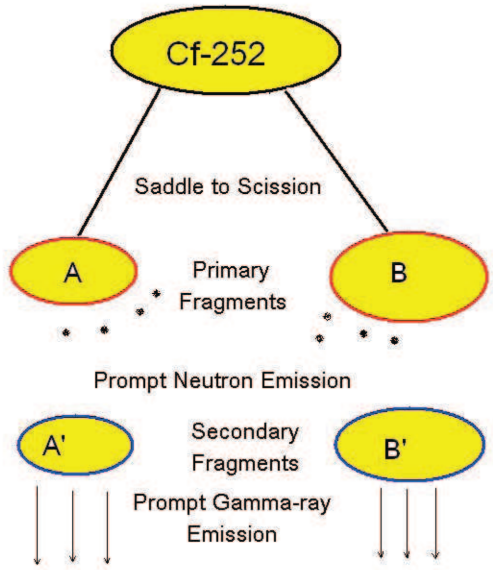

Figure 3.1: A scheme of the binary spontaneous fission process of ^{252}Cf.

data obtained from the spontaneous fission of $^{252}_{98}$Cf. During the spontaneous fission of a ^{252}Cf source, the primary fission fragments evaporate some neutrons to form the secondary fragments right after the splitting of the parent nucleus. These secondary fragments are usually in very excited states and emit γ-rays promptly. The first two steps occur very quickly, within 10^{-20} to 10^{-15} seconds. The evaporation of neutrons can take most of excitation energies, but only a small quantity of angular momenta of the primary fragments. As the neutron evaporation becomes energetically impossible, the prompt γ-ray emission takes over. The emission will eventually lead the secondary fragments to their ground states or isomeric states with a lifetime much greater than the time-scale of the fission process, relatively considered to be stable. A scheme is given in Fig. 3.1 to demonstrate the spontaneous fission process of ^{252}Cf. Though ternary fission is possible to occur where light charged particles are emitted with two primary fragments, its probability is down over two order of magnitude. So one only has to deal with the binary fission in most cases, as presented in Fig. 3.1.

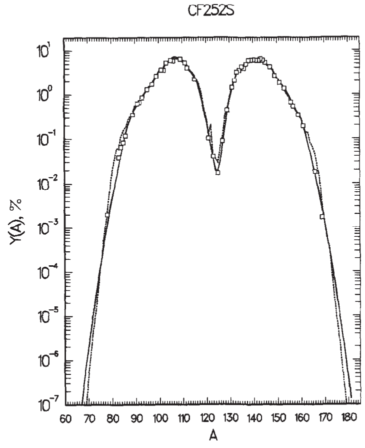

Figure 3.2: Mass-number yields $Y(A)$ vs mass number A from the experiment (□), the A'_p model (—) and Rider's mass-number yields ($\cdots$). Taken from Ref. [25].

The asymmetric breakup of ^{252}Cf produces nuclei into two mass regions, as shown in Fig. 3.2. Thus, each binary fission event of ^{252}Cf produces a complimentary pair of one heavy and one light fragment. Because of no individual proton emitted in the process, the same pair of two nuclei, whose proton numbers add up to 98, is always formed in the fission process, for example, Mo ($Z = 42$) with Ba ($Z = 56$), Tc ($Z = 43$) and Cs ($Z = 55$), Ru ($Z = 44$) with Xe ($Z = 54$), and Rh ($Z = 45$) with I ($Z = 53$). Therefore, γ-rays from a nucleus are not only coincident with γ-rays from itself but also with those from its fission partners in the coincidence measurement. This is a double-edged sword during analysis of data from the spontaneous fission of ^{252}Cf. On the one hand, for identifying transitions in an unknown nucleus, the known transitions in its partner isotopes can provide evidence. On the other hand, the existence of partner isotopes makes the data analysis more difficult because more than 150 nuclei are populated in the spontaneous fission of ^{252}Cf and each secondary fragment may give off up to 100 transitions. Overlap in transition energies occurs to obscure the signatures of the nucleus of interest.

3.2 γ-ray detection

The measurement of γ-ray energies and intensities is the major way to obtain information about the nuclear structure in a nucleus, especially in high-spin states. High-spin states decay rapidly to the ground states or isomers mostly by emitting γ-rays. Basically, one needs to consider two physical processes for γ-ray detection. One is the interaction between the incident γ-rays and the atoms of the detector material, which excites a great amount of atomic electrons from their atomic orbitals. The other is the collection of the free electrons and transformation of these electrons into a measurable electrical signal with a magnitude proportional to the incident γ-ray energies.

3.2.1 Interaction with matter

When passing through matter, γ-rays ionize by three main processes: the photoelectric effect, the Compton scattering, and the pair production .

The photoelectric effect is the case where a photon interacts with and transfers its energy to an atomic electron and then knocks out that electron from the atom. The kinetic energy of the so-called photo-electron is equal to the difference between the incident γ-ray energy and the binding energy of the corresponding atomic electron. The photoelectric effect is the dominant energy loss mechanism for photons of energies smaller than 50 keV, while it is much less important for γ-rays of higher energies.

The Compton scattering is an interaction where an incident γ-ray loses enough energy to an atomic electron to cause its ejection by the collision. The scattered photon has less energy and an emission direction different from that of the incident one. If the new photon has enough energy, more collisions may occur. The Compton scattering is the principal absorption mechanism for γ-rays of energies 100 keV to 10 MeV. The γ-rays obtained from the spontaneous fission of ^{252}Cf usually have energies from a few keV to a few MeV. So, these γ-rays lose their energies mainly through the Compton scattering.

The pair production becomes possible when the photon has an energy more than 1.02 MeV and is very important as an absorption mechanism when the energy of a photon exceeds about 5 MeV. During the interaction with the electric field of a nucleus, the energy of the incident γ-ray is converted to create an electron-positron pair, whose equivalent rest mass is equal to 1.02 MeV. The remaining γ-ray energy becomes the kinetic energies of the electron-positron pair and the recoil nucleus. The generated positron cannot exist individually and it interacts with a free electron to produce two γ-rays each of which has an energy of half of 1.02 MeV. This process is also called annihilation.

3.2.2 Gammasphere

Nowadays, modern germanium crystals, which are semiconductor materials, are widely used for γ-ray detection. They have advantages in detecting γ-rays, including excellent energy resolution and detection efficiency. The energy resolution is of particular importance for experiments which produce a lot of γ-rays of similar energies. One example of such experiments is the spontaneous fission of ^{252}Cf. High purity germanium (HPGe) detectors can provide the best energy resolution. The photons can create electron-hole pairs by exciting electrons when passing through the semiconductor crystals. If these electrons have sufficient energies, they can subsequently produce other electron-hole pairs as well. If a bias voltage is applied to the crystals, the charges can be collected as signals which are proportional to the energies of γ-rays deposited in the crystals. Thus, very large amounts of charges will be produced and collected as a measure of the corresponding γ-ray energies. The energy resolution of the HPGe crystals is around 2 keV when measured at the full width at half maximum of a 1.33-MeV γ-ray.

As mentioned in Subsection 3.2.1, the Compton scattering is the main interaction for photons of energies 100 keV to 10 MeV, which is normally the energy range of γ-rays of interest in the present experiment. It is possible for the photon to escape from the detector without depositing its entire energy in the detector crystal. Then, a signal of lower energy is produced because not all energy of this photon is collected by the detector. In practice, any event where the incident γ-ray escapes from the Ge crystal is not a desirable event because it adds to the background of the γ-ray spectrum. One good solution to this problem is to use suppression shields which detect the escaped γ-rays and thus tell the control system to deliberately ignore the corresponding energy signal from the Ge crystal. A common material used for this purpose is a scintillator Bismuth Germanate ($Bi_4Ge_3O_{12}$), known as BGO for short. This technique is called Compton suppression. It is not necessary for such a scintillator to have a good energy resolution because it is only used to veto events. The anti-Compton effect dramatically increases the peak-to-total ratio without losing the photopeak statistics.

There are three key factors which are required to be improved for better γ-ray detection: energy resolution, detection efficiency, and granularity. The solution to maximize them is to use advanced detector arrays of HPGe detectors. If over a hundred individual Ge detectors are arrayed in a sphere to surround the target area, a large detection solid angle, and thus improved detection efficiency can be obtained because of increased solid angle. An array of Ge detectors covering the target area is also able to separate multiple individual events to increase granularity. One state-of-the-art example of such arrays is the so-called GRETINA.

The Gammasphere detector array, which was completed in 1995 at Lawrence Berkeley National Laboratory, consists of 110 individual co-axial HPGe/BGO detector modules. Each Ge detector has a BGO suppression shield plus a cylindrical BGO back-plug behind the detector. The detector system is kept cool using a liquid nitrogen delivery system. The target-to-detector distance of this array is 25.25 cm. The total solid angle covered by Gammasphere is 47% of 4π with full 110 detectors. Its total photopeak efficiency is 9.9% and peak-to-total ratio is 0.6% for 1.33-MeV γ-rays. And the energy resolution is 2.5 keV for 1.33-MeV γ-rays. All of these properties of Gammasphere are very good for γ-ray detection and make it one of the most advanced γ-ray detection systems.

3.2.3 The coincidence method

The application of the coincidence method in our present experiment is a key because more than 3000 γ-rays are produced in the spontaneous fission of ^{252}Cf and the γ-ray spectrum seems extremely complex, without further conditions. In any single γ-ray gate, one sees not only the transitions in coincidence with this γ-ray in this nucleus, but also all the transitions from its up to ten different partners, along with many other random coincidence transitions. To eliminate most of the γ-rays that do not belong to the isotope of interest, the triple-coincidence technique was employed.

The principle of the coincidence method is to measure the "simultaneous" emission of more than one radiation, for example, a β-ray and a γ-ray or two γ-rays in the double coincidence and three γ-rays in the triple coincidence, with the help of two more detectors and a coincidence electric circuit for measuring the simultaneity of these events within a resolving time window. All events that occur within this time window count as coincidence events. In the present experiment, the time window is expected to be about 200 ns and any three or more events detected in this time period trigger the circuit to record a count. For example, if three γ-rays of energies E_1, E_2, and E_3 are detected within the time window, a count is added at (E_1, E_2, E_3) by one with a coordinate of E_1 along the first energy axis, E_2 along the second energy axis, and E_3 along the third energy axis. Every recorded three- or higher-fold event is thus sorted, building a full γ–γ–γ database. The count N has a relationship as $N(E_1, E_2, E_3) = N(E_1, E_3, E_2) = N(E_2, E_1, E_3) = N(E_2, E_3, E_1) = N(E_3, E_1, E_2) =$

$N(E_3, E_2, E_1)$ because each axis is constructed symmetrically.

We have to admit that this technique can result in a significant decrease in the data statistics. However, the dramatic decrease in the background relative to the peak height and the elimination of γ-rays associated with random coincidence more than compensates for this decrease in statistics. Thus, double gating on transitions in one isotope strongly enhances transitions solely in this isotope though transitions in its partners appear as well, while double gating on one transition in one isotope and one in one of its partners can highlight the transitions just in these two isotopes.

3.3 The 2000 experiment

The experimental data used for the present work were obtained from a spontaneous fission experiment performed in November, 2000 for a two-week period with the Gammasphere detector array at Lawrence Berkeley National Laboratory. A thick ^{252}Cf fission source with an α-activity of 62 μCi was placed between two 10 mg/cm^2 unmagnetized iron foils. All fission fragments were fully stopped in the iron foils and thus the need of a Doppler correction for the γ-rays emitted from the fission fragments was eliminated. The source was surrounded by a 7.62 cm polyethylene ball to absorb β-rays and conversion electrons, as well as to partially moderate and absorb fission neutrons. 101 detectors of Gammasphere were in function in this experiment. A total of 5.7×10^{11} triple- and higher-fold γ-ray coincidence events were collected. Raw experimental data were copied onto a RAID disk array for angular correlation analysis. It is also worth recalling that the low energy cut-off of the 2000 experiment is 30 keV.

It is very important to find out energies and relative intensities of γ-ray transitions as accurately as possible. So the response of the Ge detectors in Gammasphere is required to be calibrated. Some standard sources, namely ^{56}Co, ^{133}Ba, and ^{152}Eu, have been used to measure the energy calibration and efficiency curves of detectors. Energies and intensities of γ-rays in those standard sources have been tabulated in Ref. [26]. The energy calibration for Gammasphere was fitted to a third order polynomial in the form of

$$E = a + bx + cx^2 + dx^3, \tag{3.1}$$

where E is the energy in keV, x is the channel number, and a, b, c, and d are the coefficients. The fitted values for these coefficients are summarized in Table III.1.

Table III.1: Fitted coefficients of the third order polynomial in energy calibration for Gammasphere. Taken from Ref. [8].

Coefficient	Fitted value
a	-6.2734×10^{-1}
b	3.3370×10^{-1}
c	-9.0093×10^{-8}
d	4.7999×10^{-12}

The efficiency calibration was fitted to the equation as

$$\mathrm{EFF} = \exp\left[(A + Bx + Cx^2)^{-H} + (D + Fy + Gy^2)^{-H}\right]^{-1/H}, \tag{3.2}$$

where $x = \log(E/100)$, $y = \log(E/1000)$, E is the energy in keV and A, B, C, D, F, G, and H are parameters. The efficiency curve of Gammasphere is shown in Fig. 3.3 with the calculated parameters as A =14.1597, B = 9.18559, C = -2.7907, D = 6.36297, F = -0.65056, G = 0.0, and H = 2.09765 [8].

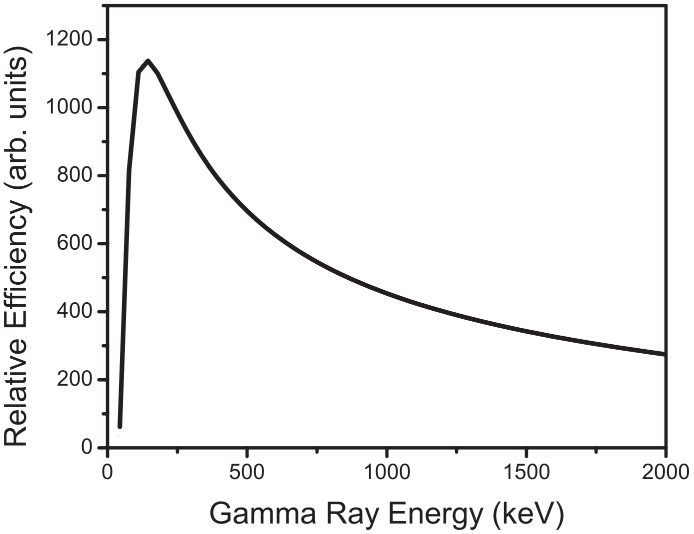

Figure 3.3: Efficiency curve of Gammasphere in arbitrary units. Taken from Ref. [8].

3.4 Data analysis

As mentioned in Section 3.3, 5.7×10^{11} triple- and higher-fold coincidence events in more than 150 nuclei with more than 3000 γ-rays were obtained in our 2000 experiment. The huge raw dataset needs to be compressed and analyzed by a certain software. The RadWare software package is a perfect tool for this purpose.

3.4.1 RadWare software package

RadWare is a software package for interactive graphical analysis of γ-ray coincidence data ,which was developed by David Radford of the Physics Division at Oak Ridge National Laboratory. It has been used by many physicists worldwide as they study the structure of nuclei and analyze the results of their experiments.

A few common RadWare programs are: *incub8r* (a program to create a compressed 1/6 cube of full symmetry), *xmlev* (a very powerful program for examining, interpreting, and fitting γ–γ–γ coincidence matrices in cube and deducing level schemes of excited states of nuclei), *gf3* (a general program for spectrum manipulation, fitting, and analysis), and *xmgls* (a program to make level scheme plots in RadWare). More information regarding programs in RadWare can be found on the website of RadWare at http://radware.phy.ornl.gov/.

A pre-scan of the raw data is required to construct a γ–γ–γ coincidence matrix. A time window should be set first. The time window of 200 ns in the present experiment is expected to include most prompt coincidences and filter out the majority of random events. If a number of transitions are observed and recorded within the time window, these transitions are expected to form an event. To increase coincidence counts for our data, events of higher fold than three were unfolded into triple-coincidence events. The matrix was built symmetrically to increase the data statistics and speed up the data analysis. It is necessary to project the matrix along one of its axes and then use the corresponding projection spectrum to make a background spectrum, which is one input file for the program *xmlev*. One has to modify the selected background spectrum until the corresponding coincidence spectra are neither with background over-subtracted nor under-subtracted, especially in either the high-energy or low-energy region.

3.4.2 Level scheme construction

Studying γ-ray emission and patterns of the γ-ray energies in nuclei allows us to know spins and parities of excited states, and thus further information of their nuclear structure. A level scheme of a nucleus usually is chosen to describe and study the nuclear properties of a nucleus graphically. These levels schemes are important not only for testing nuclear structure models but also for nuclear technology applications.

A level scheme of a nucleus can tell us the following aspects about the nuclear properties of this nucleus. They are, but not limited to, the transition energies and intensities, the level energies, spins, and parities, measurable level half-lives, and level patterns of depopulations and populations. For example, decay patterns can be used to propose different nuclear shapes. As shown in Fig. 3.4, the presence of a rotational band with an opposite parity to the yrast band of an even-even well-deformed nucleus may indicate octupole deformations/correlations in this nucleus.

The identification of the γ-ray signatures is the first important step to build a level scheme of a nucleus. The identification of a transition is the assignment of this transition to a particular nucleus, which include the assignments of both the mass number and the atomic number.

Since more than 150 nuclei are produced in the fission process of ^{252}Cf and thus the spectra are extremely complicated, it is quite difficult to fulfill this goal using

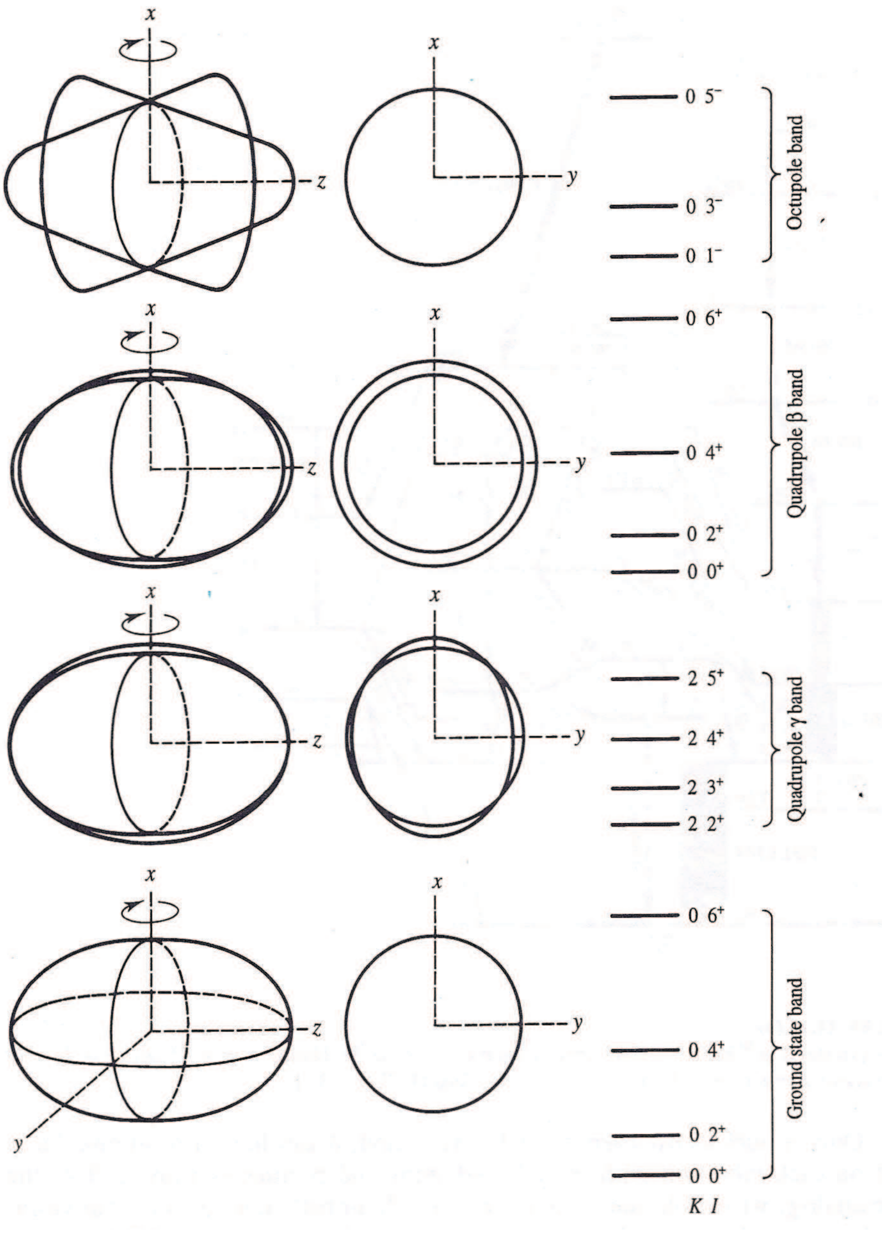

Figure 3.4: Illustration of the rotational bands built on the ground and γ-, β-, and octupole-vibrational states in a well-deformed even-even nucleus. Taken from Ref. [27].

only one technique. Therefore, a few analysis techniques, some of which will be introduced next, are employed together to identify new transitions in a particular fission fragment.

In some cases, γ-ray emission does not occur when a nucleus in an excited state decays to a lower state. Instead, the excess energy of the nucleus is used to eject electrons, and this process is called the internal conversion. This process is followed by the emission of atomic x-rays. Since these x-rays act as fingerprints of elements, if a transition is found to be in coincidence with the characteristic x-rays of a particular nucleus, the transition can be assigned to this isotope.

One can also rely on previously known experimental results. It is hard to assign transitions to a nucleus without any known γ-ray transitions in this nucleus. If there is any experiment where one or more γ-ray transitions in the nucleus of interest have been identified, the situation becomes simple. In many cases, β-decay studies have been carried out to find some low-lying excited levels with the corresponding transitions. In the experiments of the β-decay studies and heavy ion reactions, mass separation has been performed to identify a specific nucleus. It is possible for us to identify new higher-spin levels in our high statistics data with these known transitions, by double gating on the known transitions and searching for a self-consistent set of new transitions that appear in coincidence with the known ones and themselves. For a well-populated nucleus having a sufficiently large fission yield, this procedure can be simple because a well-gated spectrum shows intense peaks of transitions from higher-spin levels. However, for very neutron-rich nuclei this procedure may be somewhat difficult because they have much lower populations in the spontaneous fission of ^{252}Cf.

Even worse is that these exotic nuclei may have not been produced by other methods.

Then, one has to rely on the known transitions in the fission partners of the nucleus of interest. The prompt γ-ray transitions in the complementary fission fragments are considered to be in coincidence with each other. Therefore, in a spectrum gated on transitions in one nucleus, the transitions from the partner nuclei are expected to show up along with those belonging to this specific nucleus. The peaks of these transitions are less intense than those from the gated nucleus. In principle, all partners produced in the fission should be present in the spectrum. One may be able to identify new transitions in a new nucleus, by double gating on transitions from its different fission partners. An example will be given in Chapter IV. This method also has an advantage that one can double-check the assignment of the transitions to a particular isotope by comparing the intensities with the expected yields for each partner pair in the spectra gated on its partners.

In most cases, we have to firmly determine the mass number of the transitions we have observed. A good way to substantiate a mass number assignment of a transition to a fission fragment is to determine the correlated pair yield functions for its partners because the three- or four-neutron channel generally has the largest yield [28]. However, it is not feasible to obtain accurate results in this way in some cases, especially in the present work. This is because how high-spin states in some odd-odd isotopes decay to their ground states is not clear so far. Thus, an alternative method, which has been used for our previous work in ^{137,138}Cs [13] and ^{143,144}La [29], is adopted in the present work, described as follows. We measure the fission yield ratios of two partner isotopes of the nucleus of interest in the gates set on transitions in this nucleus and its isotopes, and then compare the variation of these ratios with those of two neighboring isotopes in the gates set on their own partners. More explicit usage will be given in the corresponding chapters.

Then one can create a level scheme based on the observed transitions to establish the structure of the nucleus of interest. Once these transitions are placed in order with respect to each other, we can see and propose the level structure of the nucleus and understand its behavior in terms of the relevant nuclear model.

It is worth mentioning that the transitions in a cascade should be in coincidence with each other, but the transitions belonging to another cascade parallel to the former should not appear in the spectra gated on the transitions from the former cascade. These parallel cascades form multiple excitation bands of the nucleus if they belong to the same isotope. So, we may observe several parallel bands in a nucleus in addition to the yrast band, where the levels have the lowest energies for each spin. We may be able to see crossings between these bands giving further evidence for the existence of the parallel bands.

The relative intensities of the γ-ray transitions also give us the clues to place these transitions in the level scheme. In the spontaneous fission of ^{252}Cf, a nucleus populated at high spin decays to the lower levels on the way to the ground state. So the transitions at lower-spin members in the same band are stronger. We can compare the relative intensities of the upper transitions by double gating on the lower transitions and then determine their locations in a cascade. The transitions in the side-bands appear to be less intense than those in the yrast band in a given nucleus. Systematics of the nuclear level schemes of neighboring nuclei of the specific nucleus and their decay patterns can also help us place the observed transitions in right order.

The next step is to assign the spin-parities (I^π) to the levels in the level scheme. This is not an easy procedure. In most cases, the spin-parity of the ground state can be known from the theoretical predictions based on the shell structure, direct measurements, or nuclear systematics. If we know the multipolarity of the transition decaying to the ground state, we are able to assign the spin-parity to the level that this transition depopulates, on the basis of the spin-parity selection rules mentioned in Subsection 2.1.1. One direct way to know the multipolarity of a transition is to measure its total internal conversion coefficient (α_{T}) and compare the experimental value with theory. We have used this method to determine the spin-parities of the levels connected by low-energy transitions. The α_{T} of a low-energy transition can be measured from the intensity balance in and out of the state where the transition feeds or decays, by double gating on other two transitions in the same cascade. Systematics are also very useful to assign the spin-parities to the excited states in a nucleus by comparing its level pattern with those of its neighboring isotones and isotopes or the corresponding nuclei in other mass regions, if they bear a remarkable likeness in their level patterns.

Another way to know the multipolarity of a transition is to measure its angular correlations with other coincidence transitions. As mentioned in Subsection 2.1.1, we are capable of knowing the difference in parities of the levels connected by a given transition from its other nuclear properties, though angular correlation analysis involving this transition is only able to assign the spins to the levels. A program reported in Ref. [30] was newly developed by our group to perform γ–γ angular correlation analysis with our Gammasphere data.

3.4.3 Angular correlation and g-factor measurements

Our high statistics data and the space structure of Gammasphere make it possible for us to carry out angular correlation measurements. At its full capacity, Gammasphere is composed of 110 HPGe detectors, corresponding to 5995 unique detector pairs. These detectors are placed at seventeen different azimuthal angles and sixty various polar angles. For each azimuthal angle, there are five to ten detectors placed symmetrically with respect to the polar angle. Because of the symmetries of Gammasphere, the angle between any two detectors will be one of only sixty-four possible values, and each of these sixty-four angle bins has many pairs of detectors. For this experiment, only 101 detectors were in function, so the number of detectors in each bin is slightly less than if Gammasphere was at its full capacity. The sixty-four angle bins are composed of detector pairs sharing the same central angle. After the relative intensity of each angle bin is found, the experimental A_2 and A_4, the two quantities for angular correlation analysis mentioned in Section 2.1.1, can be obtained by fitting the distribution to the function given by Eq. (2.13). In practice, sixty-four data points are too much for a fourth order polynomial fit as in Eq. (2.13), so the bins were further combined into seventeen. After each of the sixty-four histograms has been fitted to find the intensity of the peak of interest, the data is further binned by properly adding these numbers. The bin response function, the bin efficiency, and the solid angle correction are taken into account as well in the fitting procedure.

More information on this method as regards the solid-angle correction, the data sorting, the relative detector efficiencies, and the response function of the Gammasphere and the details of the fitting procedure can be found in Refs. [8,30,31].

As mentioned in Section 3.3, the fission fragments were implanted and stopped in a ferromagnetic material (the iron foils) where they were subject to the hyperfine fields (B_{HF}) caused by their implantation in substitutional sites in the iron lattice. It becomes possible for us to carry out angular correlation measurements to determine the g-factors of the "long-lived" states by using the integral perturbed angular correlation (IPAC) technique [4]. For an intermediate nuclear state with a lifetime τ, the spin vector of this nucleus will rotate about B_{HF} over the lifetime of this state, with a rotational frequency proportional to B_{HF} and the g-factor of this state. For our experiment, the magnetic domains in the iron foils, which were not cooled and not affected by any external field, remained randomly oriented. Then, the net result of the rotation of the implanted nucleus about the randomly oriented hyperfine fields (B_{HF}) is an attenuation of the expected angular correlation. This is the basic idea of the IPAC technique for the g-factor measurement.

If the lifetime of the state that interacts with B_{HF} is much longer than the stopping time (a few picoseconds), the angular correlation will be attenuated. Therefore, the angular correlation function $W(\theta)$ becomes

$$W(\theta) = 1 + A_2^{\mathrm{theory}}(\delta) G_2 P_2(\cos\theta) + A_4^{\mathrm{theory}}(\delta) G_4 P_4(\cos\theta) \tag{3.3}$$

where G_2 and G_4 are the attenuation factors, defined as

$$G_k = \frac{A_k^{\mathrm{exp}}(\delta)}{A_k^{\mathrm{theory}}(\delta)}. \tag{3.4}$$

The attenuation factor G_k is related to the Larmor precession frequency ω_{L} and the lifetime τ by [32]

$$G_k = \frac{1}{2k+1}(1 + 2\sum_{q>0}^{k} \frac{1}{1+q^2\phi^2}), \tag{3.5}$$

where the angle of precession ϕ is related to the Larmor precession frequency ω_{L} and the lifetime τ by

$$\omega_{\mathrm{L}} = \frac{\phi}{\tau} = \frac{\mu_{\mathrm{N}} g B_{\mathrm{HF}}}{\hbar}. \tag{3.6}$$

In these equations, the subscript k is the same as that in Eq. (2.9), g is the nuclear g-factor, B_{HF} is the nuclear hyperfine field in iron, and μ_{N} is the nuclear magneton.

The $A_{2,4}^{\mathrm{theory}}$ can be calculated for various values of the mixing ratio for a given spin sequence with the Wigner 3-j and 6-j coefficients, as outlined and tabulated in Refs. [3, 5]. With these theoretical values, the attenuation factor G_k is found by measuring A_k^{exp}, and then using Eq. (3.4). The g-factor of the state can be extracted by solving Eqs. (3.5) and (3.6) as

$$|g| = \frac{\hbar\phi}{\mu_{\mathrm{N}} B_{\mathrm{HF}} \tau}. \tag{3.7}$$

It is worth noting that ϕ, proportional to the product $gB_{\mathrm{HF}}\tau$, needs to be within certain limits for the present method to be applicable. If ϕ is very small, the angular correlation will not be attenuated; if ϕ is quite large, then G_k will approach their asymptotic limits of $G_2 = \frac{1}{5}$ and $G_4 = \frac{1}{9}$, as indicated in Eq. (3.5), with no useful information for the g-factor measurements. Because only ϕ^2 can be obtained from Eq. (3.5), our method can measure only the magnitude, but not the sign of the g-factor.

In iron, hyperfine fields are of the order between 10 and 100 Tesla and typically g-factors for states with lifetimes from a few hundred picoseconds to a few nanoseconds can be measured by the IPAC technique with the source/foil arrangement used in the present work. For the excited states with a much shorter lifetime, but still longer than the stopping time, it is assumed that the angular correlations will not be perturbed and no attenuation will be observed. To obtain the nuclear g-factor from the angular correlation attenuation, the hyperfine field needs to be known. Our previous reports on this method [14, 33, 34] show that the hyperfine fields were not aligned and that no significant electric fields were generated by radiation damage in the foils. The compilation by Rao [35] is a useful, though somewhat outdated, source of the B_{HF} values.

Because of the extremely large number of γ-rays in our fission experiment, some additional coincidence gates can be applied to the angular correlation of interest for better selectivity. In the present work, it is not necessary to use additional gates in some cases because the coincidence spectrum is relatively clean for transitions of energies > 1 MeV. Most of the correlations for the $N = 83$ isotones are unattenuated because of their large transition energies as reported in Chapter VI.

CHAPTER IV

TRIAXIALITY IN THE $A = 110$ REGION: LEVEL STRUCTURES OF ^{114,115}Rh

4.1 Introduction

The $Z = 45$ neutron-rich Rh isotopes are five protons below the 50 proton closed shell and midway between the 50 and 82 neutron major shells, a region where nuclei are characterized by shape coexistence and shape transitions, including triaxial shapes [36]. In this region, the active proton orbitals, near the top of the $\pi g_{9/2}$ sub-shell, drive the nuclear shape towards oblate deformations, while the neutron Fermi levels, below or near the bottom of the $\nu h_{11/2}$ sub-shell, drive the shape to prolate deformations. These tendencies have been observed in the yrast bands of odd-Z and odd-N nuclei which are built on the $\pi g_{9/2}$ and $\nu h_{11/2}$ orbitals. Shape coexistence and transitions in even-Z nuclei in this region have been studied [24]. The proton orbitals originating from the $g_{9/2}$ sub-shell are influenced by the triaxial nuclear deformation. The appearance of triaxial deformations and soft shape transitions were found in nuclei of $Z \geq 42$ [24, 37]. Our systematic studies of neutron-rich odd-Z isotopes of Y, Nb, Tc, and Rh ($Z = 39, 41, 43, 45$) indicated a shape transition from an axially symmetric shape with very large quadrupole deformations in ^{99,101}Y to an axially asymmetric shape with large triaxiality in ^{107,109,111}Tc and ^{111,113}Rh isotopes [38–41].

Because of the deformations driven by $N \approx 60$ neutrons ($\nu h_{11/2}$), several proton sub-shells are near the Fermi levels and may play a role in the odd-Z nuclei with $A \approx 110$. Rotational bands built on $\pi g_{9/2}$, $\pi p_{1/2}$ and $\pi(g_{7/2}/d_{5/2})$ sub-shells were found in odd-even $^{107-113}$Rh [41–43]. In our previous studies on Rh isotopes, calculations with a rigid-triaxial-rotor-plus-quasiparticle (RTRP) model provided a reasonable fit to the excitation energies and branching ratios in the $\pi g_{9/2}$ yrast bands and the collective yrare bands and to the signature splitting in the $\pi g_{9/2}$ yrast bands of ^{111,113}Rh at near-maximum triaxiality with $\gamma = 28^\circ$ [41]. The yrare bands built on the $11/2^+$ state also provided evidence for triaxiality in these nuclei. It is of interest to extend our knowledge of the structures of Rh isotopes to the more neutron-rich ^{114,115}Rh. Low-lying states in these two isotopes were observed in β-decay studies and reported in Refs. [44] and [45], respectively. However, there has not been any report on high-spin states in ^{114,115}Rh before this work.

The odd-odd Rh isotopes are of great interest in that a remarkable similarity in high-spin, negative-parity states was seen through a large range of neutron numbers from 59 (^{104}Rh) to 67 (^{112}Rh) [41,46–50]. The spin-parity of the band-head is 6^- with a 7^- intermediate state from $N = 59$ to $N = 65$ and then the band-head becomes 7^- in ^{112}Rh. The $\Delta I = 1$, negative-parity yrast bands originating from the coupling of a proton in the $g_{9/2}$ orbital with a strongly aligned $h_{11/2}$ neutron occur at low and moderate excitations in odd-odd Rh isotopes. The level scheme of ^{114}Rh shows the same structure as the light Rh isotopes and the level scheme is proposed to be built on a 7^- excited state from the systematics of the odd-odd Rh isotopes. The signature inversion of the yrast bands of ^{106,112,114}Rh is observed to occur at 10.6 $\hbar$ for ^{114}Rh, 12.5 $\hbar$ for ^{112}Rh, and 13.7 $\hbar$ for ^{106}Rh.

For ^{115}Rh, the yrast and yrare bands are observed. Spin-parity assignments are proposed for the observed levels based on the systematics of the odd-even Rh isotopes.

Though odd-even $^{109-113}$Rh isotopes show back-bending which was argued to be the result of alignment of an $h_{11/2}$ neutron pair [41], the level scheme of ^{115}Rh is not observed to sufficiently high spins to show this phenomenon. Calculations based on the RTRP model for ^{115}Rh have been carried out and compared with the experimental data. Preliminary results favor a triaxial shape with $\beta_2 = 0.26$ and $\gamma = 28^\circ$ in ^{115}Rh.

4.2 Experimental results

^{114,115}Rh are too neutron-rich to be produced by heavy-ion reactions to study their high-spin states. However, according to theoretical predictions of fission yields in the spontaneous fission of ^{252}Cf [25], the sufficiently large fission yields of ^{114,115}Rh make it possible to observe excited states in these two isotopes in our high statistics database.

The basic idea to identify new transitions in an unknown nucleus is by double gating on transitions in its partner isotopes and comparing the fission yields, as mentioned in Subsection 3.4.2. The fission partners of ^{114,115}Rh are I isotopes, namely $^{133-136}$I [51–54].

In particular, one should recall that the transition energy overlap occurs in some neighboring isotopes which makes it more difficult to identify and assign new transitions in the spectra observed by gating on transitions in their partners. There are several examples, such as the 192.4-keV transition in ^{104}Mo [55] and the 193.1-keV transition in ^{108}Mo [56], the 242.0-keV transition in ^{108}Ru and the 240.8-keV transition in ^{110}Ru [57], the 159.3-keV transition in ^{110}Rh and the 159.2-keV transition in ^{112}Rh [41], and the 211.7-keV transition in ^{111}Rh and ^{113}Rh [41]. The level schemes of ^{114,115}Rh established in the present work are shown in Figs. 4.1 and 4.2, respectively.

One clearly sees that the strongest transitions of energies 211.2 keV in ^{114}Rh and 213.3 keV in ^{115}Rh overlap and are also severely masked by the strongest 211.7-keV transition in ^{111}Rh and ^{113}Rh whose fission yields are much larger than those of ^{114}Rh and ^{115}Rh. This may be why high-spin states in either ^{114}Rh or ^{115}Rh have not been observed for a long time, though the fission yields of ^{114}Rh and ^{115}Rh make it possible for us to find them in our high statistics data. This means that one highlight of the present work is the separation of the four peaks, the 211.7 keV in ^{111,113}Rh, the 211.2 keV in ^{114}Rh, and the 213.3 keV in ^{115}Rh, in the spectra with gates set on transitions in their partner I isotopes.

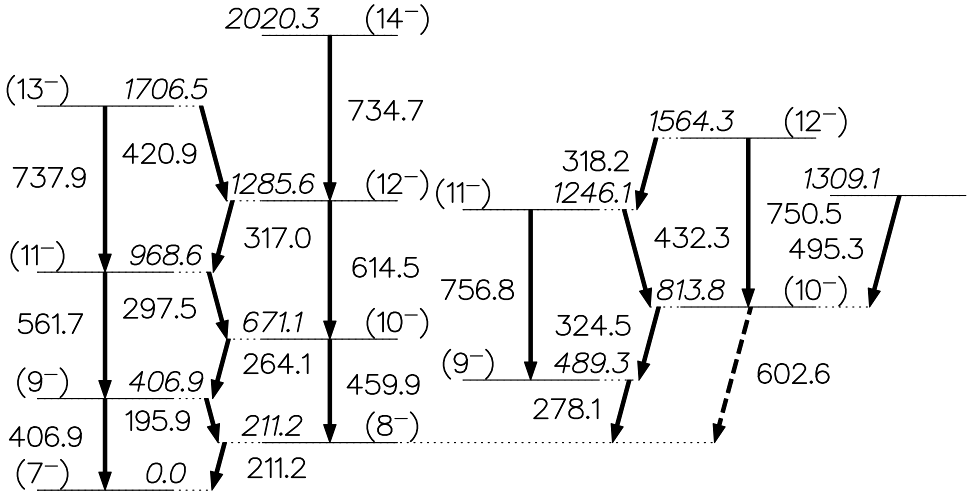

Figure 4.1: The new level scheme of ^{114}Rh. Energies are in keV. All transitions are newly observed.

The identifications of the transitions in ^{114,115}Rh are based on extensive cross-

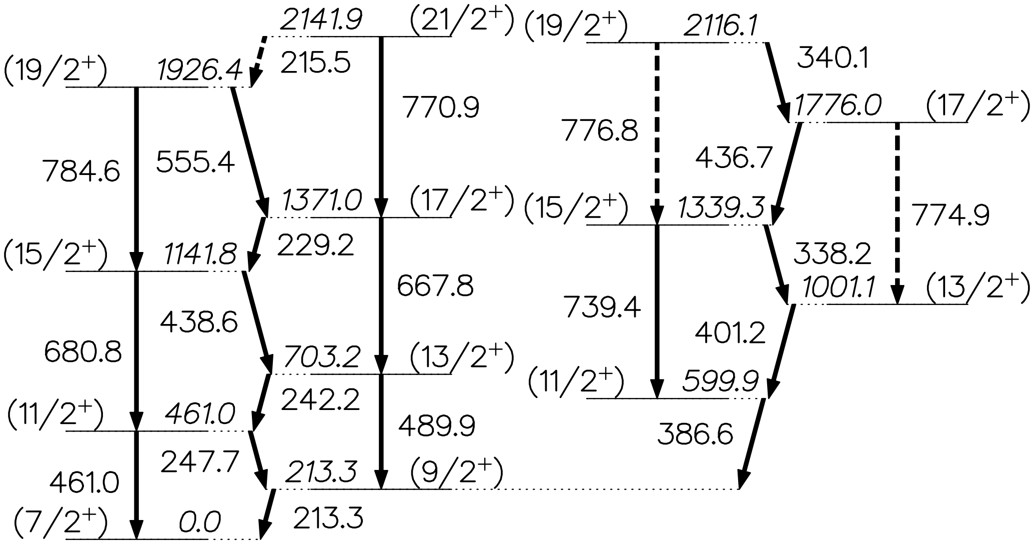

Figure 4.2: The new level scheme of ^{115}Rh. Energies are in keV. All transitions are newly observed.

checking of the coincidence relationships and relative transition intensities with those of the complementary fission fragments $^{133-136}$I, and with the relevant transitions in ^{114,115}Rh as well. Careful background subtractions are always performed to eliminate possible accidental coincidences. To show how new transitions in ^{114,115}Rh are identified, several coincidence spectra are created, by double gating on strong transitions in the $^{133-135}$I isotopes and new ones assigned to ^{114,115}Rh.

Two spectra are obtained by double gating on two transitions in ^{134}I and ^{135}I, respectively, as shown in Fig. 4.3. Three new transitions of energies 195.9, 247.7, and 278.1 keV are seen in both spectra, along with those previously known strong transitions in ^{111,112,113}Rh [41, 43]. Let us first double gate on the new 195.9-keV transition in Fig. 4.3 and on a strong transition in ^{134}I (952.4 keV) and one in ^{135}I

(1133.8 keV), as shown in Fig. 4.4 (a) and (b). In Fig. 4.4 (a) and (b), three new transitions of energies 211.2, 264.1, and 297.5 keV are seen. Though the transition of energy 232.3 keV in ^{113}Rh is also seen in Fig. 4.4 (a) and (b), it is doubtful that the new transition of energy 211.2 keV is the same as the transition of energy 211.7 keV in ^{113}Rh. By comparing Fig. 4.4 (a) with (c) and Fig. 4.4 (b) with (d), respectively, where the gates are set on transitions in ^{134}I and ^{113}Rh for Fig. 4.4 (c) and ones in ^{135}I and ^{113}Rh for Fig. 4.4 (d), one can conclude that the new 211.2-keV transition is not the one of energy 211.7 keV in ^{113}Rh. Figure 4.5 shows the spectra, double gated on the new 278.1-keV transition and a strong transition in ^{134}I (952.4 keV) and one in ^{135}I (1133.8 keV), respectively, which indicate the same new transition of energy 211.2 keV as in Fig. 4.4 (a) and (b), along with a new transition of energy 324.5 keV. The following spectra are double gated on the new 278.1- and 324.5-keV transitions, the new 195.9- and 211.2- keV transitions, and the new 195.9- and 264.1-keV transitions, as shown in Fig. 4.6. These three spectra show the new transitions and the coincidence relationship among them and those known transitions in I isotopes (the 912.7-keV transition in ^{133}I, the 952.4-keV transition in ^{134}I, the 288.2- and 1133.8-keV transitions in ^{135}I, and the 1111.8-keV transition in ^{136}I), which allows us to build the new level scheme of one Rh isotope, as shown in Fig. 4.1.

Now let us turn to the new transition of energy 247.7 keV observed in Fig. 4.3. Three spectra are obtained by double gating on the 247.7-keV transition and a strong transition in each of the ^{133,134,135}I isotopes, respectively, as shown in Fig. 4.7. Two new transitions of energies 213.3 and 242.2 keV are found in these spectra. The 211.7-keV transition in ^{113}Rh and the new 213.3-keV transition form a doublet peak

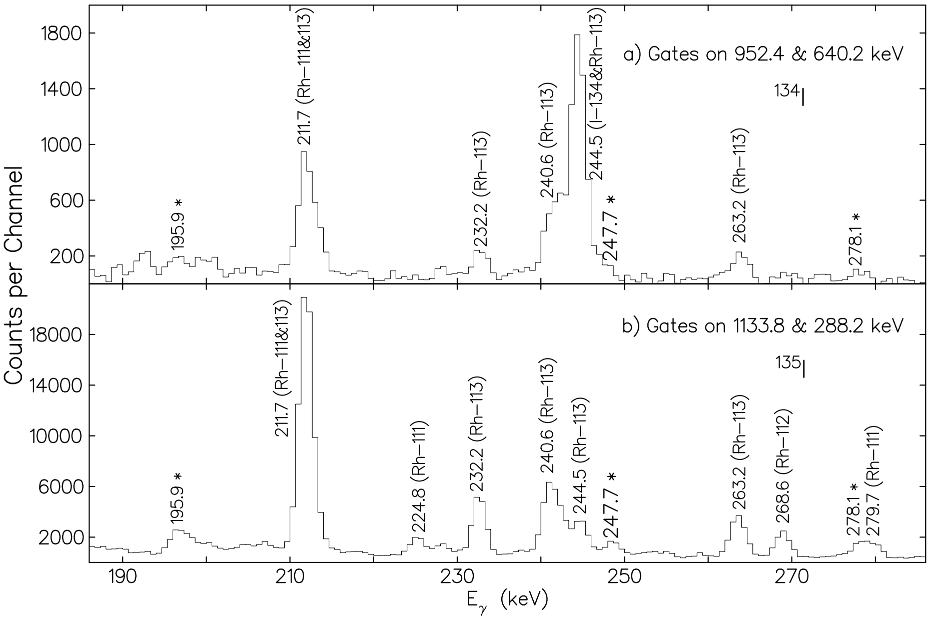

Figure 4.3: Coincidence spectra double gated on transitions in ^{134,135}I. Three new transitions of energies 195.9, 247.7, and 278.1 keV are indicated with an asterisk.

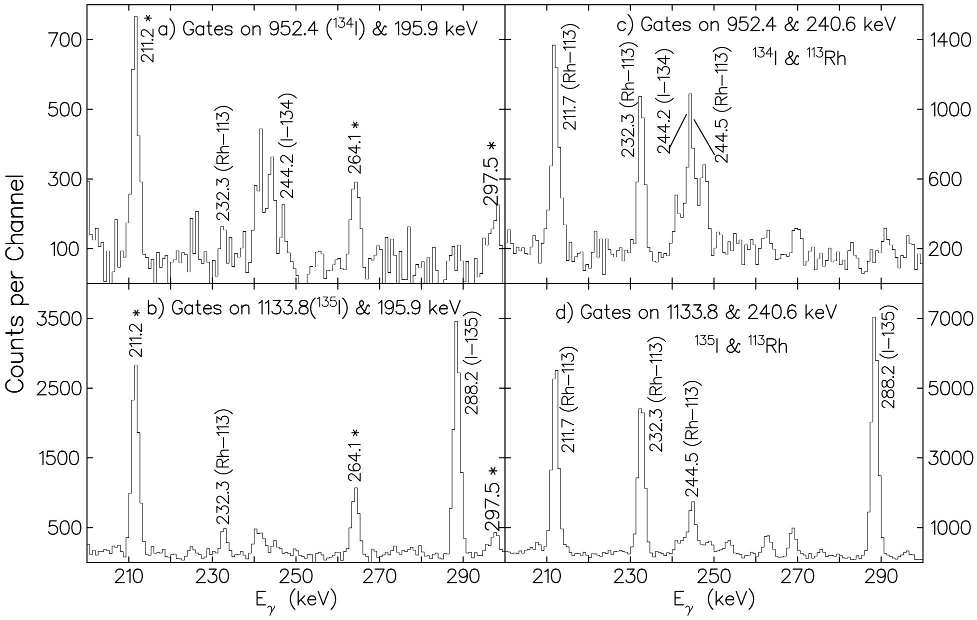

Figure 4.4: Coincidence spectra double gated on the new 195.9-keV transition (see Fig. 4.3) and the 952.4- (^{134}I) and 1133.8-keV (^{135}I) transitions. Three new transitions of energies 211.2, 264.1, and 297.5 are marked with an asterisk. The spectra gated on transitions in ^{134}I and ^{113}Rh, and ones in ^{135}I and ^{113}Rh are shown on the right side as evidence that the new 211.2-keV transition is not the one of energy 211.7 keV in ^{113}Rh.

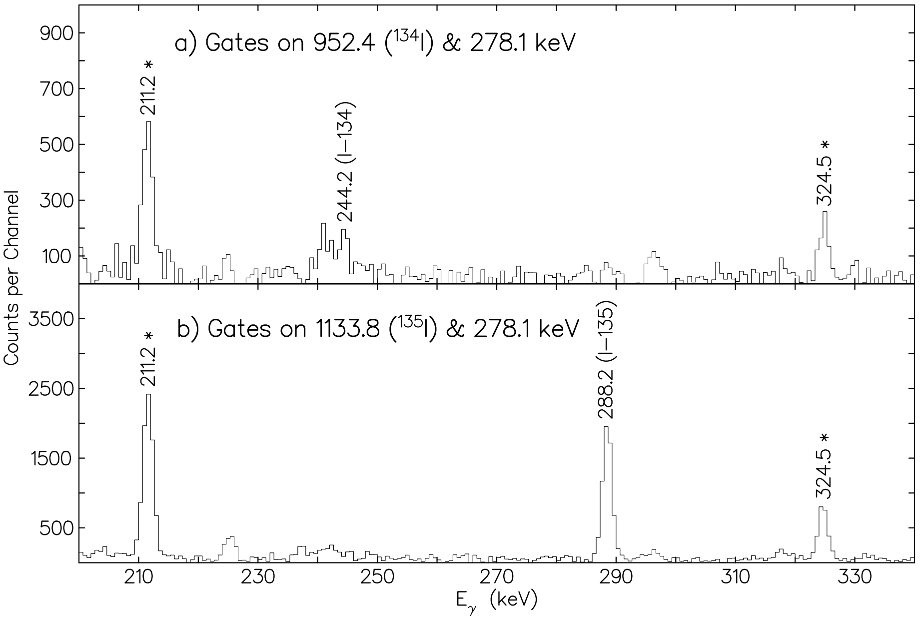

Figure 4.5: Coincidence spectra double gated on the new 278.1-keV transition (see Fig. 4.3) and the 952.4- (^{134}I) and 1133.8-keV (^{135}I) transitions. The new transitions of energies 211.2 and 324.5 keV are marked with an asterisk.

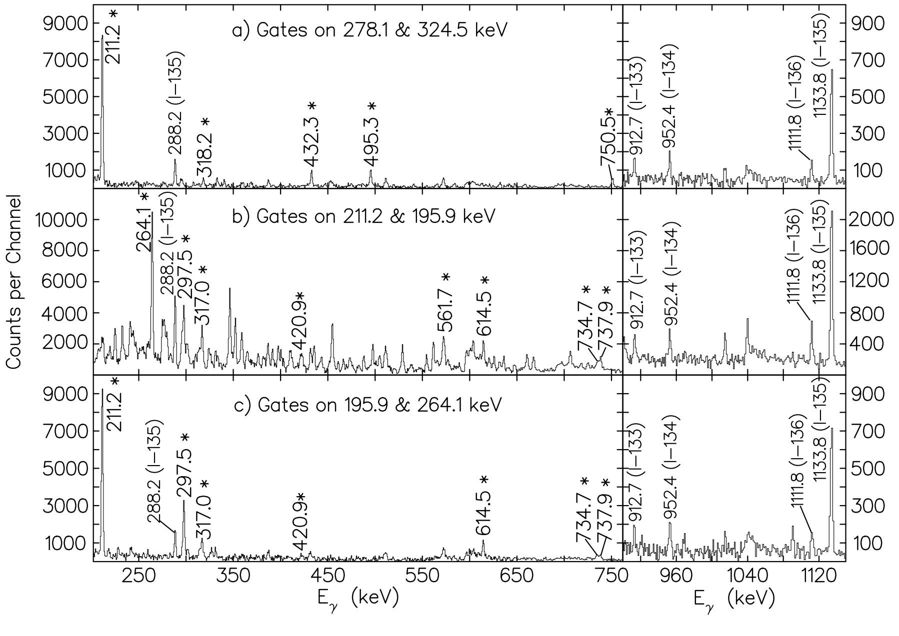

Figure 4.6: Coincidence spectra double gated on the new 278.1- (see Figs. 4.3 and 4.5) and 324.5-keV (see Fig. 4.5) transitions, the new 195.9- (see Figs. 4.3 and 4.4) and 211.2-keV (see Fig. 4.4) transitions, and the new 195.9- (see Figs. 4.3 and 4.4) and 264.1-keV (see Fig. 4.4) transitions. All transitions marked with an asterisk are newly observed.

in Fig. 4.7 (c) because of the large fission yield of ^{113}Rh, 4-n fission partner of ^{135}I. A careful examination of Fig. 4.3 (a) reveals a shift of the 211.7-keV peak to the right, which indicates that a new transition of energy about 213 keV should exist there and this transition belongs to a heavier Rh isotope other than ^{113}Rh. This transition is confirmed in Fig. 4.7 as the 213.3-keV transition. The spectra gated on the new 213.3-keV transition and the 912.7- (^{133}I), 952.4- (^{134}I), and 1133.8-keV (^{135}I) transitions, respectively, clearly demonstrate the coincidence relationship among the 213.3-, 242.2-, and 247.7-keV transitions as well as those in the I isotopes, as presented in Fig. 4.8. One new transition of energy 489.9 keV, equal to the sum of 242.2 and 247.7 keV, is coincident with the gate transitions. A new transition of energy 386.6 keV is observed in Fig. 4.8, but not coincident with the new 247.7-keV transition, which indicates that the 386.6-keV transition, in coincidence with the new 213.3-keV transition and transitions in the I isotopes, may compose another band in this Rh nucleus. The spectra in Fig. 4.9, double gated on the new 386.6-keV transition and the 912.7- (^{133}I), 952.4- (^{134}I), and 1133.8-keV (^{135}I) transitions, respectively, support such an assumption with the observation of the 213.3-keV transition and two new transitions of energies 338.2 and 401.2 keV, although the latter two are not very strong. Three spectra created by double gating on the new 213.3- and 247.7-keV transitions, the new 242.2- and 247.7-keV transitions, and the new 386.6- and 338.2-keV transitions, respectively, as shown in Fig. 4.10, support the coincidence relationship among the newly observed transitions and the known ones in $^{133-136}$I. These coincidence data enable us to establish the new level of one Rh isotope, as shown in Fig. 4.2.

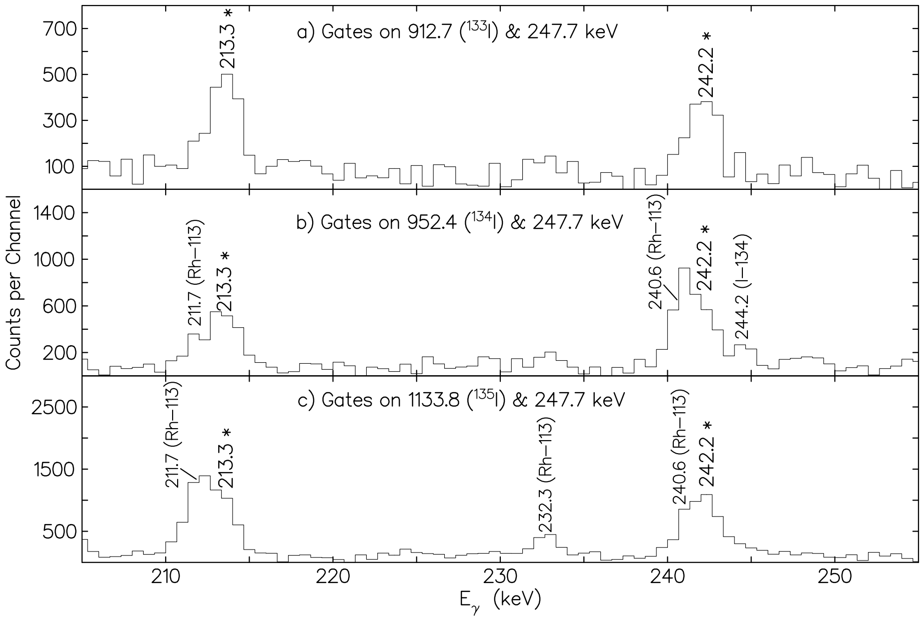

Figure 4.7: Coincidence spectra double gated on the newly observed 247.7-keV transition (see Fig. 4.3) and the 912.7- (^{133}I), 952.4- (^{134}I), and 1133.8-keV (^{135}I) transitions. Two new transitions of energies 213.3 and 242.2 keV are seen and marked with an asterisk.

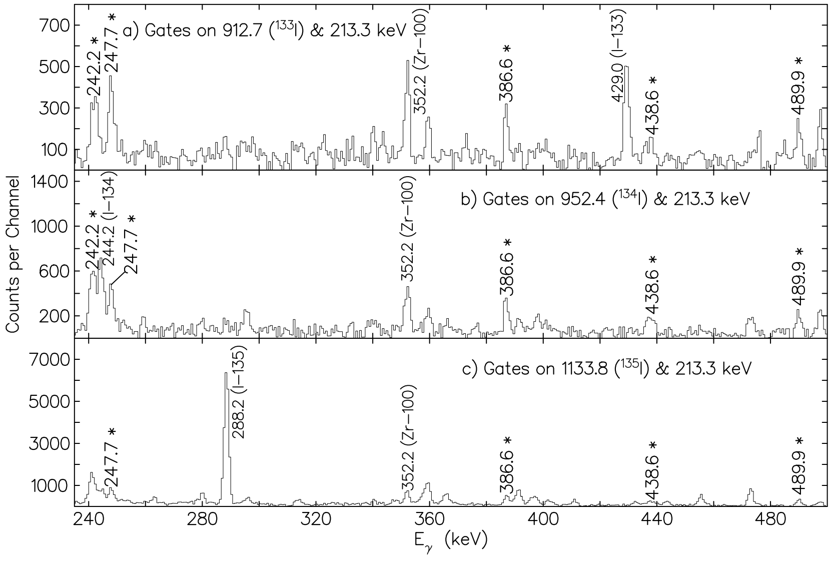

Figure 4.8: Coincidence spectra double gated on the new 213.3-keV transition (see Fig. 4.7) and the 912.7- (^{133}I), 952.4- (^{134}I), and 1133.8-keV (^{135}I) transitions. The new 489.9-, 386.6-, and 438.6-keV transitions are marked with an asterisk. The strongest 212.6-keV transition in ^{100}Zr [58], close to 213.3 keV, leads to the contamination of the 352.2-keV peak (^{100}Zr) [58] in these spectra.

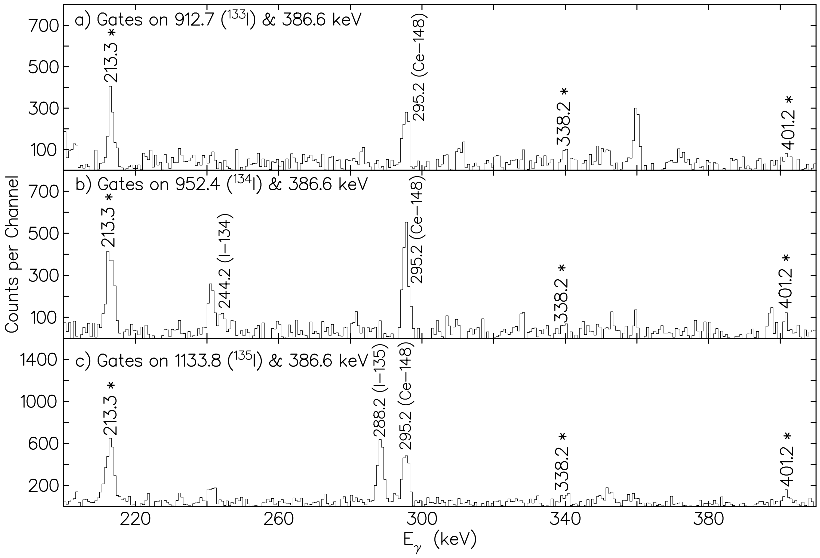

Figure 4.9: Coincidence spectra double gated on the new 386.6-keV transition (see Fig. 4.8) and the 912.7- (^{133}I), 952.4- (^{134}I), and 1133.8-keV (^{135}I) transitions. The new 213.3-keV transition (see Figs. 4.7 and 4.8) is seen. Two new 338.2- and 401.2-keV transitions are seen. The 295.2-keV transition in ^{148}Ce is a contamination introduced by the 386.2-keV transition in ^{148}Ce [59] that is close to 386.6 keV.

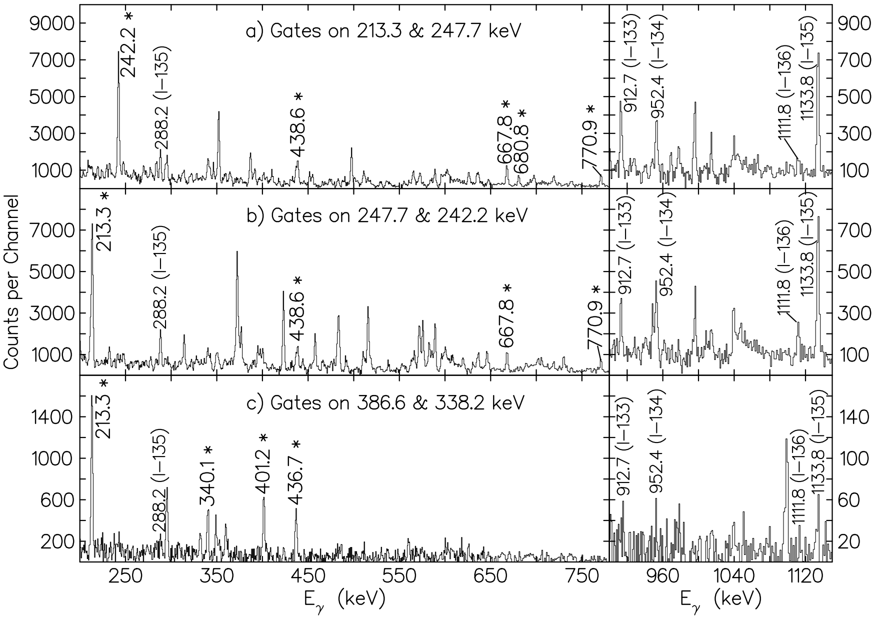

Figure 4.10: Coincidence spectra double gated on the new 213.3- (see Fig. 4.7) and 247.7-keV (see Fig. 4.3) transitions, the new 247.7- (see Fig. 4.3) and 242.2-keV (see Fig. 4.7) transitions, and the new 386.6- (see Fig. 4.8) and 338.2-keV (see Fig. 4.9) transitions. All coincidence transitions marked with an asterisk are newly observed.

As seen in the above spectra, the transitions in the level schemes shown in Figs. 4.1 and 4.2 are in coincidence with transitions in I isotopes. Therefore, we propose the level schemes shown in Figs. 4.1 and 4.2 belong to one or two Rh isotopes. A simple comparison of the relative intensities among the 912.7- (^{133}I), 952.4- (^{134}I), 1133.8- (^{135}I), and 1111.8-keV (^{136}I) transitions in Figs. 4.6 and 4.10 reveals that the level schemes belong to two different Rh isotopes and the former should be lighter than the latter. Because the level schemes of $^{109-113}$Rh are well known, we propose that the former level scheme in Fig. 4.1 is of ^{114}Rh while the latter in Fig. 4.2 is of ^{115}Rh.

The most crucial support is from the following measurements to determine the mass numbers of these transitions. As mentioned in Chapter III, one way to assign the mass number to transitions in a fission fragment is to determine the correlated pair yield functions for the partners because the three- or four-neutron channel generally has the greatest yield [28]. However, it is not feasible to obtain accurate results here. This is because how high-spin states in the odd-odd I and Rh isotopes decay to their ground states has not been clear so far. In addition, the serious overlap caused by the strong transition of energy 211.7 keV in ^{113}Rh obstructs this method. In the 60.6/183.0- (^{112}Rh), 232.2/240.6- (^{113}Rh), 195.9/264.1-, and 213.3/247.7-keV double gates, the fission yield ratios of the 1111.8-keV transition in ^{136}I to the 1133.8-keV transition in ^{135}I are measured to be 0.55(8), 0.32(4), 0.21(3), and 0.15(2), respectively, as shown in Fig. 4.11. The variation of these ratios is similar to those of ^{146}La to ^{145}La in the $^{101-104}$Nb gates, of ^{142}Cs to ^{141}Cs in the $^{105-108}$Tc gates, and of ^{136}I to ^{135}I in the $^{110-113}$Rh gates, as presented in Fig. 4.11. So the mass numbers for both of the 247.7 → 213.3- and 264.1 → 195.9-keV cascades are above 113 and the former is larger than the latter. Therefore, we conclude that the 247.7 → 213.3-keV cascade is in ^{115}Rh and the 264.1 → 195.9-keV cascade in ^{114}Rh after considering the fact that the fission yields of ^{114}Rh and ^{115}Rh are much greater than those of other heavier Rh isotopes in the ^{252}Cf fission. The same ratios in the new 278.1/324.5- and 213.3/386.6-keV gates are also measured as 0.22(3) and 0.16(2), respectively, as shown in Fig. 4.11, which supports the proposal that the 324.5 → 278.1- and 401.2 → 386.6-keV cascades form a side-band in ^{114}Rh and ^{115}Rh, respectively, as presented in Figs. 4.1 and 4.2. To further confirm this assignment, two additional plots are given in Figs. 4.12 and 4.13. Figure 4.12 shows the fission yield ratios of ^{135}I to ^{134}I in the $^{112-115}$Rh gates, which keep the same tendency as those intensity ratios of ^{136}I to ^{135}I in the same gates. The fission yield ratios of ^{135}I to ^{133}I and ^{136}I to ^{134}I in the $^{113-115}$Rh gates are presented in Fig. 4.13, where the variations of both are similar. More evidence for our mass number assignments will be discussed in the next section. Thus, the high-spin level schemes of ^{114}Rh and ^{115}Rh are built for the first time in the present work, as shown in Figs. 4.1 and 4.2, respectively.

In fission experiments, spin values can be assigned on the basis of internal conversion coefficients of low-energy transitions and $\gamma - \gamma$ angular correlations. The statistics of our present data for ^{114,115}Rh are too weak to carry out such an analysis. Therefore, as discussed in the next section, the spin-parity assignments shown in Figs. 4.1 and 4.2 are mainly based upon the assumption that spin values increase with increasing excitation energies in yrast decays and the analogy with the level structures of the lighter Rh isotopes and neighboring nuclei.

Because of the overlap of the 211.7-keV transition in ^{113}Rh and the relatively low

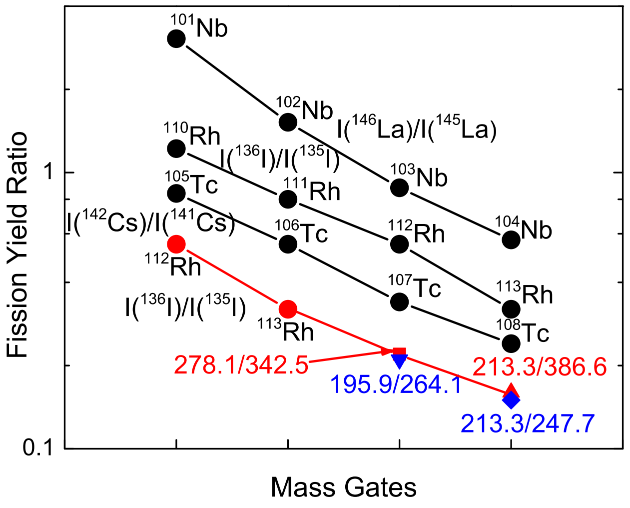

Figure 4.11: Fission yield ratios of ^{136}I to ^{135}I in Rh gates, along with those of ^{146}La to ^{145}La in Nb gates and of ^{142}Cs to ^{141}Cs in Tc gates. Data are taken from Refs. [38, 39, 41, 53, 54, 60–65] and the present work. A logarithmic scale is used for the y-axis. The uncertainties are smaller than the symbol size.

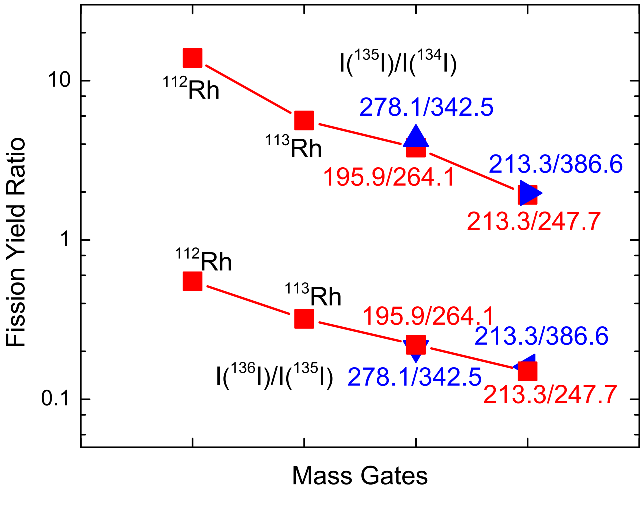

Figure 4.12: Fission yield ratios of ^{136}I to ^{135}I and of ^{135}I to ^{134}I in Rh gates. Data are taken from Refs. [41, 52–54] and the present work. A logarithmic scale is used for the y-axis. The uncertainties are smaller than the symbol size.

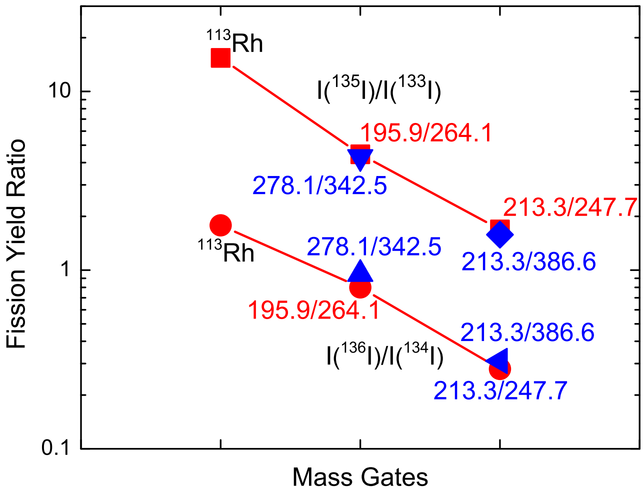

Figure 4.13: Fission yield ratios of ^{136}I to ^{134}I and of ^{135}I to ^{133}I in Rh gates. Data are taken from Refs. [41,51–54] and the present work. A logarithmic scale is used for the y-axis. The uncertainties are smaller than the symbol size.

yields of ^{114,115}Rh in the spontaneous fission of ^{252}Cf, only the γ branching ratios for some levels are measured and summarized in Table IV.1 for further discussion, instead of the relative transition intensities.

Table IV.1: γ branching ratios of some levels in ^{114,115}Rh are given in parentheses following the corresponding transitions.

Nucleus	Level energy (keV)	Spin-parity	Transition energy (keV)
^{114}Rh	406.9	(9^-)	195.9 (100); 406.9 (126)
	671.1	(10^-)	264.1 (100); 459.9 (39)
	968.6	(11^-)	297.5 (100); 561.7 (43)
	1285.6	(12^-)	317.0 (100); 614.5 (84)
^{115}Rh	461.0	$(11/2^+)$	247.7 (100); 461.0 (59)
	703.2	$(13/2^+)$	242.2 (100); 489.9 (87)
	1141.8	$(15/2^+)$	438.6 (100); 680.8 (24)

4.3 Discussion and calculations

The high-spin level schemes of ^{114,115}Rh, established here for the first time, provide very useful information for further exploring the structure evolution in the more neutron-rich region of the Rh isotopic chain. Even though the level schemes of these two heavier Rh isotopes are not established to very high spins due to their low fission yields, we can still obtain some valuable conclusions, which will be discussed next.

4.3.1 ^{114}Rh

The $\Delta I = 1$, negative-parity yrast band assigned to ^{114}Rh as displayed in Fig. 4.1, together with the level schemes built on the $\pi g_{9/2} \otimes \nu h_{11/2}$ configuration in lighter odd-odd $^{104-112}$Rh shows a striking similarity that supports a common interpretation for all bands, as presented in Fig. 4.14. Figure 4.14 shows the level structures of odd-odd $^{104-114}$Rh relative to the 7^-state in each nucleus. On the basis of this similarity, tentative spins and parities are assigned to the states of the yrast band of ^{114}Rh, as presented in Fig. 4.1. With an assumption that the 278.1-keV transition has an $E2/M1$ character, spins and parities are assigned to the levels in the side-band in ^{114}Rh as well. Note that no such side-band populating the (8^-) level has been observed in the other odd-odd Rh isotopes.

Earlier investigations of odd-odd $^{100-114}$Rh in β-decay studies established their low-lying excited states. The ground states of ^{100}Rh and ^{102}Rh were found to be 1^- and 2^-, respectively, and those of odd-odd $^{104-114}$Rh were proposed to have a spin-parity of 1^+ [66]. A 5^+ isomeric state was seen in ^{100,104}Rh, fed by a transition from a

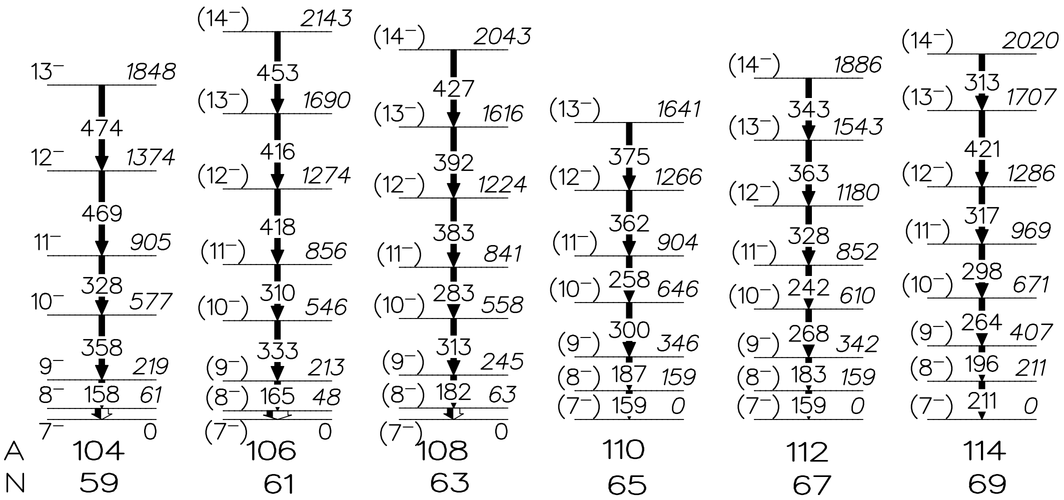

Figure 4.14: $\Delta I = 1$, negative-parity yrast bands of odd-odd $^{104-114}$Rh associated with the $\pi g_{9/2} \otimes \nu h_{11/2}$ configuration. Level energies are relative to the corresponding 7^- state. Data are taken from the present work for ^{114}Rh and Refs. [41, 46–50] for others.

6^+ state while a 6^+ isomeric state was found in ^{102}Rh, fed by a transition from a 5^+ state [46]. High-spin states of both negative and positive parities in ^{100,102,104}Rh are built on their isomeric states [46]. A 6^+ isomeric state was proposed for ^{106,112}Rh while a 5^+ isomeric state for ^{108,110}Rh [41, 47–50]. Note that no positive-parity, high-spin level was observed in ^{106,108,110,112}Rh, feeding their isomeric states. It is also interesting that the 7^- state of the $\Delta I = 1$, negative-parity bands of odd-odd $^{104-112}$Rh decays to a 5^+ isomeric state through a 6^- state or directly to a 6^+ isomeric state. It is worth mentioning that there is no 6^- state seen in ^{112}Rh, but its 7^- band-head decays to a 6^+ isomer. One observes a remarkable likeness between the level structures of ^{110}Rh and ^{112}Rh relative to the 7^- state and their resemblance to the level structure of ^{114}Rh. Therefore, it is reasonable to propose that the present level scheme of ^{114}Rh is built on a 7^- state. However, we have not observed any transition depopulating the 7^- state in ^{114}Rh to an isomeric state.

The signature splitting is a quantity of the difference of the Routhians (the energy referring to the rotating coordinate system) between the two signatures of a rotational band. This quantity can be used as an indicator of the shape of the nucleus. A signature splitting is expected where a large Coriolis mixing is involved. This is more pronounced at high spin. Moreover, such an effect can also be found at the bottom of a rotational band where the Fermi level is located between two orbitals coming from a high-j sub-shell. A triaxial deformation can also contribute to the signature splitting, because K is not a good quantum number any longer. Here, the plots for the signature splitting of yrast bands of odd-odd $^{108-114}$Rh and odd-even $^{107-115}$Rh are presented in Figs. 4.15 and 4.16, respectively, where the signature splitting function $S(I)$ (extremely sensitive to the triaxial deformation parameter γ) is defined as

$$S(I) = \frac{E(I) - E(I-1)}{E(I) - E(I-2)} \frac{I(I+1) - (I-2)(I-1)}{I(I+1) - (I-1)I} - 1. \tag{4.1}$$

One sees that the signature splitting of ^{114}Rh as well as of ^{108,110,112}Rh is not as large as that of ^{115}Rh, which is comparable to those of ^{109,111,113}Rh. This feature provides additional support for our spin-parity assignments. In the case of ^{108}Rh, $\gamma = 11°$ reproduces the level pattern better than $\gamma = 23°$ [43], which was successfully used to interpret the level structure of ^{107}Rh [42]. If we assume that the γ value for ^{114}Rh is similar to that for ^{108}Rh, which is much smaller than the calculated results of $\gamma = 28°$ for ^{113}Rh and $\gamma = 28°$ for ^{115}Rh, one may reach a conclusion that the triaxial deformation in ^{114}Rh is not as large as in ^{115}Rh, as in the case of ^{108}Rh and ^{107}Rh. The side-band feeding the (8^-) state in the yrast band is also a sign of the existence of the triaxial deformation in ^{114}Rh (see the next subsection for the discussion about the yrare band). The observation of such a band in ^{114}Rh may indicate that triaxiality in ^{114}Rh is stronger than estimated from the systematics with $\gamma \approx 15°$, because one has not seen the yrare band in ^{108}Rh.

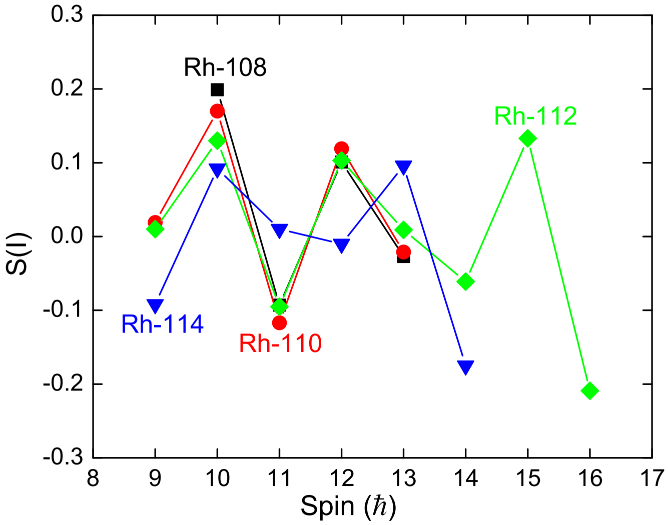

Figure 4.15: Signature splitting function $S(I)$ for yrast bands of odd-odd $^{108-114}$Rh. Data are taken from Refs. [41, 48–50] and the present work.

Figure 4.15 also exhibits another three striking features: first, the signature splitting decreases and then increases with increasing spins; second, the signature splitting is anomalous at low spin; third, the inversion of the signature is observed in ^{112,114}Rh. The favored signature of the configuration $j_\pi \otimes j_\nu$ for high-spin states in an odd-odd nucleus is expected to be $\alpha_{\mathrm{f}} = \frac{1}{2}\left[(-1)^{j_\nu - 1/2} + (-1)^{j_\pi - 1/2}\right]$ [67], which gives α_{f}=0 for the $\pi g_{9/2} \otimes \nu h_{11/2}$ configuration in odd-odd Rh isotopes [50]. So, the favored signature states in odd-odd Rh isotopes have even-integer spins. If the Routhian of the favored signature is found to lie higher in energy as compared to that of the unfavored

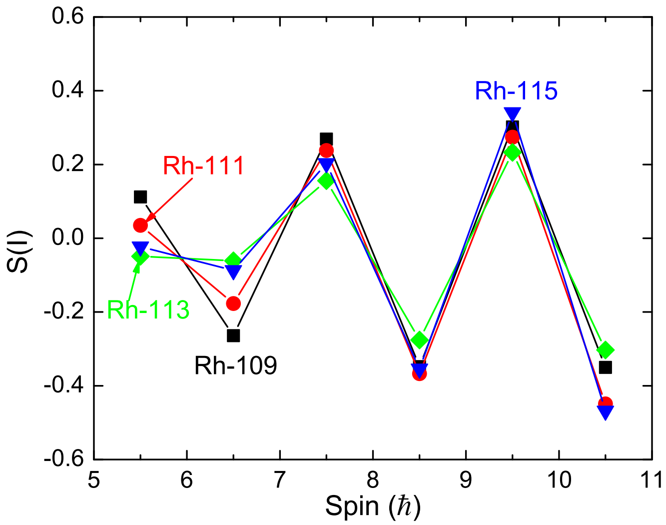

Figure 4.16: Signature splitting function $S(I)$ for yrast bands of odd-even ${}^{109-115}$Rh. Data are taken from Refs. [41–43] and the present work.

signature, the corresponding signature splitting is anomalous. In Fig. 4.15, $S(I)$ for states with even-integer spins are higher than states with odd-integer spins at low spin in odd-odd Rh isotopes. Thus, the anomalous signature splitting is seen in these odd-odd Rh isotopes.

To demonstrate the anomalous signature splitting in more detail and find the signature inversion points more distinctly, two additional plots are present here. In Fig. 4.17, $E(I)-E(I-1)$ (energy difference) vs spin is plotted for yrast bands of odd-odd ${}^{106-114}$Rh, which is a simple way to indicate the signature inversion. One clearly sees the energy differences of the favored signature partners are larger than those of the unfavored signature partners in odd-odd ${}^{106-114}$Rh at low spin. The energy differences of the unfavored signature partners rise above those of the favored signature partners at some spin for ^{106}Rh, ^{112}Rh, and ^{114}Rh, where the signature inversion occurs. After that, the signature splitting becomes normal and the anomalous splitting disappears.

The inversion points for ^{106}Rh, ^{112}Rh, and ^{114}Rh are seen to be 13.7 $\hbar$, 12.5 $\hbar$, and 10.6 $\hbar$, respectively, as indicated in Fig. 4.17. Though levels in ^{108}Rh and ^{110}Rh were not identified sufficiently high to find such points, we can still predict them according to the data of ^{108}Rh and ^{110}Rh shown in Fig. 4.17. The values of both points for ^{108}Rh and ^{110}Rh seem to be larger than 13 $\hbar$ and smaller than 14 $\hbar$, while the value for ^{108}Rh is greater than that for ^{110}Rh. To be more exact, one can estimate the spin point for ^{108}Rh as 13.5 $\hbar$ and that for ^{110}Rh as 13.2 $\hbar$. It is very interesting to find that the signature inversion points decrease with increasing neutron numbers in these odd-odd Rh isotopes. The same trend is followed in odd-odd $^{108-116}$Ag as well, as shown in Fig. 4.18, where the inversion points for ^{108}Ag, ^{110}Ag, and ^{116}Ag are indicated to be 14.4 $\hbar$, 12.7 $\hbar$, and 11.8 $\hbar$, respectively. In Fig. 4.18, one may also estimate the inversion point for ^{112}Ag larger than ^{116}Ag and smaller than ^{110}Ag, though it is somewhat difficult to estimate that for ^{114}Ag. The interpretation of this observation will be discussed below. Interesting systematics can be seen in Figs. 4.17 and 4.18 that $E(I)-E(I-1)$ (energy difference) monotonically decreases with increasing neutron numbers for the favored signature partners in both Rh and Ag isotopes. Another useful plot in odd-odd $^{106-114}$Rh is given in Fig. 4.19, where $\Delta E = \big[E(I)-E(I-1)\big] - \frac{1}{2}\Big\{\big[E(I+1)-E(I)\big] + \big[E(I-1)-E(I-2)\big]\Big\}$ vs spin is shown. In this figure, it is easier and clearer to determine the signature inversion points for ^{106}Rh, ^{112}Rh, and ^{114}Rh as the values proposed above. From the above mentioned, we confirm the proposal in Ref. [43] that the anomalous signature splitting does not persist for spin values greater than 14 $\hbar$ in ^{106,108}Rh. Note that only the study of a particular configuration $j_\pi \otimes j_\nu$ along a wide isotopic chain can lead to such information.

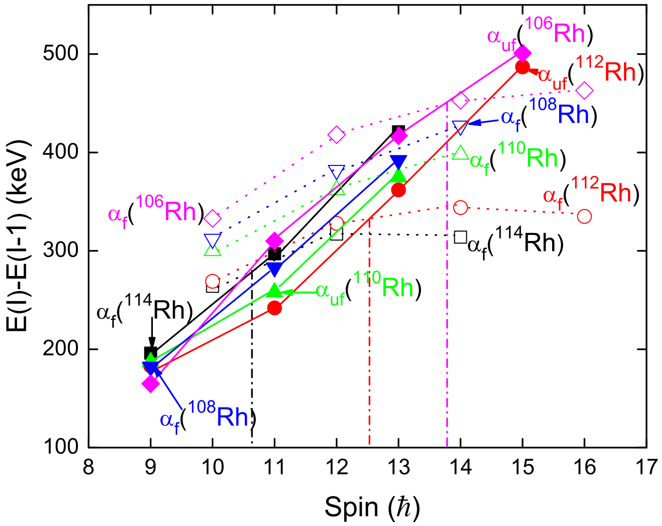

Figure 4.17: $E(I) - E(I-1)$ (energy difference) vs spin is used to indicate the signature inversion of yrast bands of odd-odd $^{106-114}$Rh. The signature inversion is observed in ^{106}Rh, ^{112}Rh, and ^{114}Rh. Open and solid symbols are for the favored and unfavored signature states, respectively. Data are taken from Refs. [41, 47–50] and the present work.

The observation of the anomalous signature splitting and the signature inversion is a common feature in many mass regions. In all cases, the normal signature splitting is achieved above a certain spin value, which depends on the nucleon numbers. The mechanism of the signature inversion has been studied in various theoretical frameworks, giving different explanations. Some of them involve the same grounds as in the odd-A cases, such as the influence of triaxial shapes or the particular locations of the two Fermi levels among the orbitals originating from high-j sub-shells for axial shapes. Moreover, a significant residual proton-neutron interaction in the particle-plus-rotor model with an axially symmetric core can also induce an anomalous signature split-

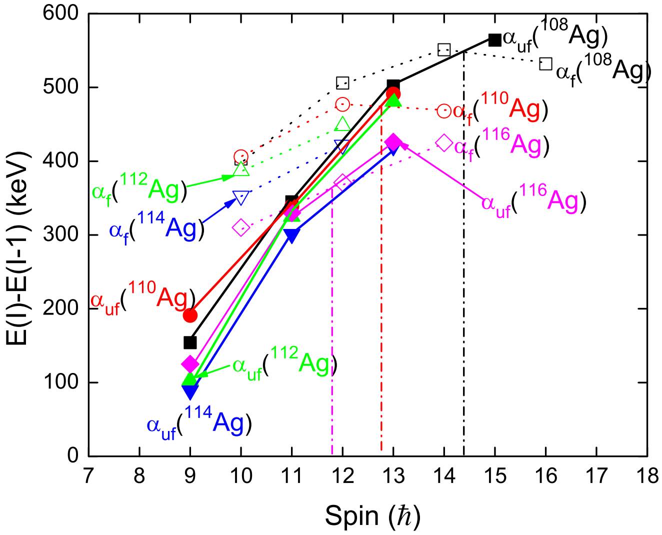

Figure 4.18: $E(I) - E(I-1)$ (energy difference) vs spin is used to indicate the signature inversion of yrast bands of odd-odd $^{108-116}$Ag. The signature inversion is observed in ^{108}Ag, ^{110}Ag, and ^{116}Ag. Open and solid symbols are for the favored and unfavored signature states, respectively. Data are taken from Refs. [48, 49, 68].

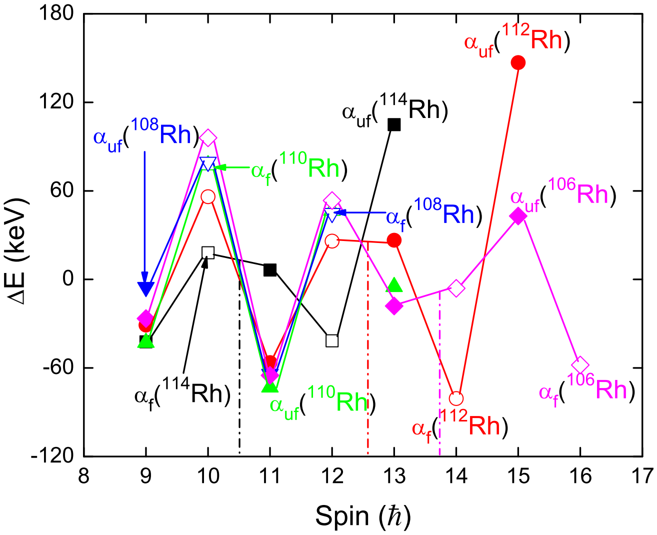

Figure 4.19: ΔE vs spin is plotted to indicate the signature inversion of yrast bands of odd-odd $^{106-114}$Rh. The signature inversion is observed in ^{106}Rh, ^{112}Rh, and ^{114}Rh. Open and solid symbols are for the favored and unfavored signature states, respectively. Data are taken from Refs. [41, 47–50] and the present work.

ting followed by the signature inversion. The mechanism of the signature inversion in odd-odd nuclei is still an open question and theorists have been working to find a universal mechanism for different mass regions.

Theoretical calculations were carried out based on the cranking shell model with triaxial shapes [69], which predicted the existence of the signature inversion in the $A = 80$, 100, 130, and 160 regions. For nuclei in the rare-earth region, the signature inversion in ^{154}Tb was well reproduced with the triaxial parameter $\gamma = 13.5°$. By investigating nuclei in the rare-earth region with $A \approx 160$, the authors in Ref. [69] found the γ value range $5° < \gamma < 25°$ to reproduce the experimental results. However, the author in Ref. [70] proved that the signature inversion in odd-odd nuclei in the above mass regions can be consistent with an axially symmetric shape with the Coriolis effects in the particle-plus-rotor-model framework once the angular momentum is retained as a good quantum number in the calculations. Thus, the experimental signature inversion might not be used as evidence for triaxial shapes and the cranking shell-model calculations could be so realistic as to compare with experiments with such a small $\gamma \approx 10°$ [67]. The deficiencies of the cranking model were also explained and its applicability to the signature inversion phenomenon in odd-odd nuclei was questioned in Ref. [71]. The author in Ref. [71] found that the best result could be obtained when the proton-neutron interaction is combined with triaxial deformations using a particle-plus-rotor model. The signature inversion can also be obtained in the projected shell-model framework with axial symmetric shapes resulting from the crossing of different bands with opposite signature dependence, which was proposed in Ref. [72]. After that, the triaxial projected shell model in a realistic configuration space was developed and used to reproduce the signature inversion in the $A = 130$ region very well [73]. The systematics studies of the signature inversion in the $A = 160$ region in Ref. [74] indicated that triaxiality and Coriolis effects alone are not sufficient to predict the experimental results and a residual proton-neutron interaction must be taken into account in the particle-plus-rotor-model calculations. The Interacting Boson-Fermion Model was also proposed to give theoretical explanations for the signature inversion [75]. The quadrupole-pairing interaction to the mean-field potential combined with triaxiality was found to be able to account for the signature inversion in the $A = 130$, 160 regions in Ref. [76].

More recently, a few theoretical calculations have been done to interpret the signature inversion observed in $A \approx 100$ Rh and Ag isotopes. With the reproductions of the signature inversion points of 14 $\hbar$ for ^{102}Rh and 10 $\hbar$ for ^{98}Rh, the authors in Ref. [77] found that the competition between the proton-neutron interaction and the Coriolis force using a two-quasiparticle-plus-rotor model can be a universal mechanism for the signature inversion phenomenon in all mass regions, $A = 80$, 100, 130, and 160. However, the same authors later claimed that the triaxial deformation could play an important role where the signature inversion was observed at high spin in the $A = 100$ region [78]. By studying the signature inversion in the odd-odd ^{102,104}Rh and ^{104,106}Ag and in three-quasiparticle rotational bands in ^{101}Rh, the authors in Ref. [79] using the cranking shell model proposed that these nuclei have a triaxial shape with $\gamma \approx 25°$ which causes the signature inversion. They mentioned that the observed inverted signature splitting is somewhat larger than the one predicted and this discrepancy may be caused by ignoring the effect of the quadrupole-pairing interaction proposed in Ref. [76]. It is interesting that those authors in Ref. [79] gave a new theoretical interpretation to the signature inversion in the $A = 100$ region as a competition between the proton-neutron interaction and the Coriolis force in Ref. [80].

Regarding the current cases in the $A = 110$ region, it is obvious that triaxiality is supposed to play an important role in the nuclear structures in the above odd-odd Rh isotopes. Since an yrare band is observed in ^{114}Rh, it is possible for us to see such a band in lighter odd-odd Rh isotopes. If so, larger triaxial deformations might be required to interpret the yrare band and one might obtain a large γ. Then one may propose that the triaxial deformation results in the signature inversion in these nuclei. Of course, the origin of the signature inversion in the $A = 110$ region poses a good question for more experimental and theoretical work.

4.3.2 ^{115}Rh

The level structure of ^{115}Rh, as presented in Fig. 4.2, bears significant resemblance to those of ^{111}Rh and ^{113}Rh, mainly in bands 1 and 6 reported in Ref. [41], though levels in ^{115}Rh are not identified as high as those in ^{111}Rh and ^{113}Rh and only two bands are observed in ^{115}Rh, not as many as in ^{111}Rh and ^{113}Rh. A side-band strongly populating the yrast $(9/2^+)$ excited level has been observed in ^{115}Rh, as in ^{111}Rh and ^{113}Rh, which indicates a deviation from axial symmetry. In Ref. [81], the study on ^{125}Xe shows that the signature pattern of the yrast band could be in two triaxial shapes, either on the prolate side or the oblate side. The side-band, so-called yrare band, was used to determine which side the triaxial shape is on. The side-band in the Xe isotope is analogous to the side-band here in ^{115}Rh, as confirmed in ^{111,113}Rh in Ref. [41]. In the following model calculations, level energies in ^{115}Rh are well reproduced as natural consequences of the triaxial deformation.

As shown in Fig. 4.16, a very large, normal signature splitting of the yrast band is observed in ^{115}Rh. The splitting pattern in ^{115}Rh is similar to those in ^{109,111,113}Rh and all of these four Rh isotopes have a likeness in the splitting strength at high spin. Such a large signature splitting observed in ^{109,111,113}Rh has been interpreted in Refs. [41, 42] in terms of triaxiality playing a major role. One also finds a large signature splitting in the neighboring Ag isotopes, ^{115}Ag and ^{117}Ag, as plotted in Fig. 4.20. The signature splitting in the Ag isotopes is even greater than that in their corresponding Rh isotones, which may indicate that the strength of triaxiality in these Ag isotopes is larger than that in the corresponding Rh isotones, since a softness for triaxiality in ^{115,117}Ag was proposed in Ref. [82]. Otherwise, there might be an unknown reason causing such a large signature splitting in these two Ag isotopes.

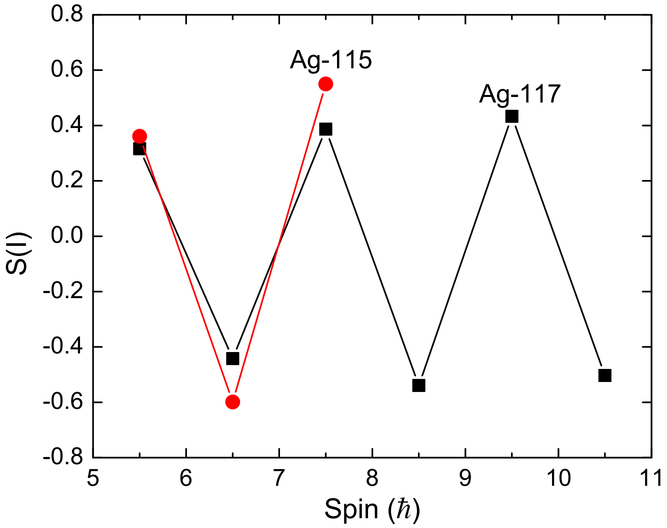

Figure 4.20: Signature splitting function $S(I)$ for yrast bands of odd-even ^{115,117}Ag. Data are taken from Ref. [82]

In Ref. [41], Luo *et al.* reported the observation of back-bending in the yrast bands of ^{111,113}Rh that sets in above the $21/2^{+}$ level in ^{111}Rh and the $19/2^{+}$ level in ^{113}Rh. Therefore, it is of interest to find where the back-bending occurs in ^{115}Rh. Figure 4.21 is a back-bending plot (kinetic moment of inertia vs rotational frequency) for the yrast bands of $^{108-115}$Rh. A back-bending is clearly seen in ^{109}Rh, ^{111}Rh, and ^{113}Rh and the back-bending frequency moves monotonically higher with decreasing neutron numbers in these isotopes. For ^{115}Rh, its kinetic moment of inertia at low rotational frequency is comparable to those for ^{109}Rh, ^{111}Rh, and ^{113}Rh. One cannot determine where a back-bending occurs in ^{115}Rh because levels in ^{115}Rh identified here are not as high as in ^{111,113}Rh. However, one may predict that the back-bending frequency in ^{115}Rh, which is obviously higher than that in ^{113}Rh, is either comparable to or higher than that in ^{111}Rh or higher than even that in ^{109}Rh, by following the data shown in Fig. 4.21. It is very interesting to see that the back-bending in ^{115}Rh does not conform to the above systematics in ^{109}Rh, ^{111}Rh, and ^{113}Rh. More experimental work is needed to find the accurate back-bending frequency and further theoretical work is required to interpret the above observation. Data for the odd-odd $^{108-114}$Rh are also included in Fig. 4.21, where no back-bending is found in these nuclei. This is another support for our mass number and spin-parity assignments. The lack of back-bending in ^{108,110,112,114}Rh could be blocking by the odd neutron. So, the back-bending in ^{109}Rh, ^{111}Rh, and ^{113}Rh means a neutron pair breaking in these odd-even Rh isotopes. As mentioned in Ref. [41], the breaking pair is in the $h_{11/2}$ neutron orbital.

Figure 4.22 shows the systematics of the long odd-even Rh isotopic chain from

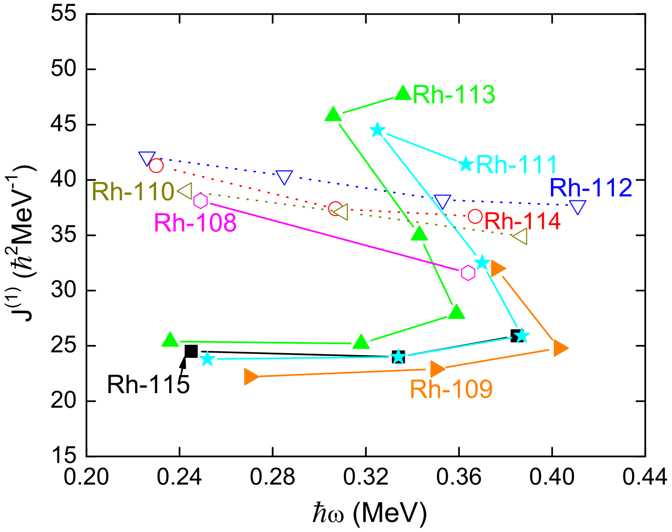

Figure 4.21: Kinetic moment of inertia vs frequency for the $\alpha = +1/2$ signature partners of yrast bands of odd-even $^{108-115}$Rh and the even-integer signature partners of yrast bands of odd-odd $^{108-115}$Rh. Back-bending is observed in ^{109,111,113}Rh. Possible back-bending frequency for ^{115}Rh is estimated. See text. Date are taken from Refs. [41–43, 48–50] and the present work.

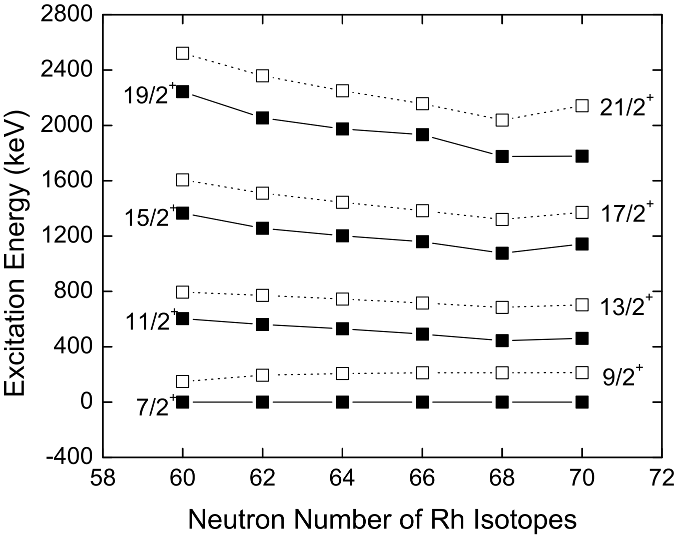

Figure 4.22: Systematics of level energies in yrast bands of odd-even $^{105-115}$Rh. Excitation energies decrease towards $N = 68$ and after that increase. Data are taken from Refs. [41–43, 83] and the present work.

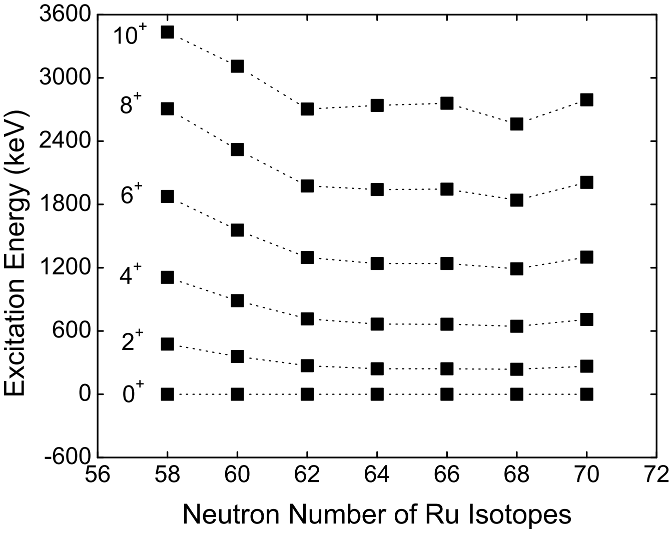

Figure 4.23: Systematics of level energies in yrast bands of even-even $^{102-114}$Ru. Excitation energies decrease towards $N = 68$ and after that increase. Data are taken from Refs. [57, 84–86].

^{105}Rh to ^{115}Rh. Level energies of the yrast bands of these Rh nuclei are compared and a trend that excitation energies decrease with increasing neutron numbers is observed before the neutron number reaches 68. Systematics of the yrast bands of neighboring Ru and Pd is given in Figs. 4.23 and 4.24, respectively, where one also sees decreasing level energies with increasing neutron numbers at $N \leq 68$. The level energies increase when the neutron number goes beyond 68 in all Ru, Rh, and Pd isotopes. This $N = 68$ effect is more distinct in Pd with larger neutron numbers. It is worth pointing out that finding a similar effect in the Rh isotopes as assigned supports our mass number and spin-parity assignments as well.

It is worth investigating the systematics of excitation energies of the yrare bands in the Rh and neighboring Tc isotopes where triaxiality has been proposed [39–41]. Such yrare bands are believed to be associated with the triaxial deformation. In Fig. 4.25, the level energies up to the $(15/2^+)$ state in the yrare bands relative to

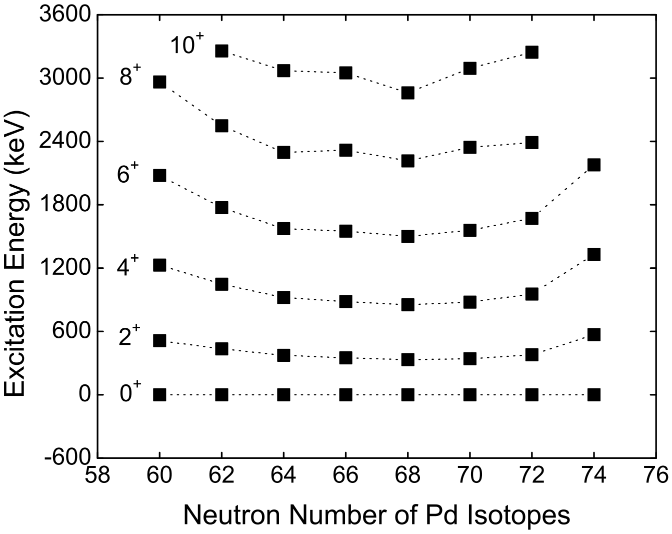

Figure 4.24: Systematics of level energies in yrast bands of even-even $^{106-120}$Pd. Excitation energies decrease towards $N = 68$ and after that increase. Data are taken from Refs. [87–90].

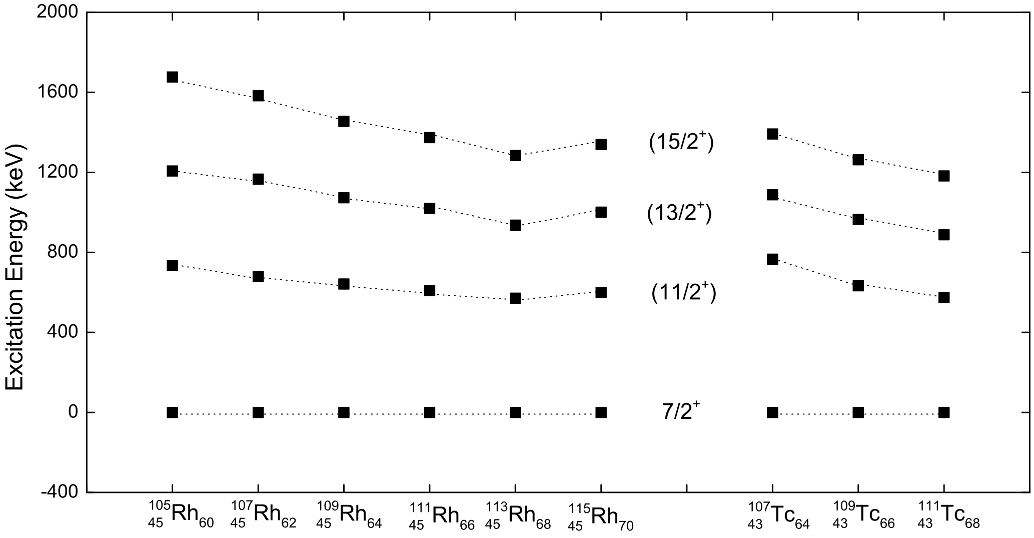

Figure 4.25: Systematics of level energies in yrare bands of odd-even $^{105-115}$Rh and $^{107-111}$Tc. Excitation energies decrease towards $N = 68$ and after that increase in Rh isotopes. Data are taken from Refs. [39–43, 83] and the present work.

the 7/2$^+$, ground state in odd-even $^{105-115}$Rh and $^{107-111}$Tc are plotted. The above mentioned $N = 68$ effect is seen again in the yrare bands in the Rh isotopes. However, one cannot make a clear conclusion of this effect at $N = 68$ in the yrare bands in the Tc isotopes, because such excited states in ^{113}Tc have not been observed yet.

Preliminary theoretical results based on the RTRP model show that triaxiality in ^{115}Rh has $\beta_2 = 0.26$ and $\gamma = 28°$. The details of this model can be found in Ref. [91]. Without going into details, we have to mention that the nuclear shape is described by the conventional deformation parameters β_2 and γ and the free parameters are β_2, γ, and the first $E(2^+)$ of the core. More information can be found in Ref. [41].

These three parameters have been fitted to the level energies of the yrast band and the yrare band of ^{115}Rh, which are expected to be very close to those of ^{113}Rh. The fitted values for them are $\beta_2 = 0.26$, $\gamma = 28°$, and $E(2^+) = 0.31$ MeV. The predicted level energies are summarized in Table IV.2, where very good agreement is seen between experiment and theory, though a discrepancy appears in the yrare band. The 21/2$^+$ yrast state in Table IV.2 seems to be mixed with a $\pi(1g_{9/2})^3$ configuration, which does not belong to the model space. Such a configuration manifests itself by causing back-bending. For the fitting of other experimental quantities, such as the signature splitting and branching ratios, some fine tuning appears necessary and is under way.

It is worth mentioning that the single particle wave function of the yrast band and the yrare band of ^{115}Rh is dominated by an $\Omega = 7/2$ single particle state, which corresponds to the [413]7/2$^+$ Nilsson orbital. On a spherical basis, its main component has $j = 9/2$. It is interesting to remark that nearly all the bands in ^{111,113}Rh have

Table IV.2: Experimental and theoretical energies of excited states in the yrast band and the yrare band of ^{115}Rh. Energies are in keV.

	Yrast band		Yrare band	
Spin-parity	E^{exp}	E^{theory}	E^{exp}	E^{theory}
$7/2^+$	0	0		
$9/2^+$	213	111		
$11/2^+$	461	467	600	567
$13/2^+$	703	592	1001	983
$15/2^+$	1142	1069	1339	1539
$17/2^+$	1341	1281	1776	2105
$19/2^+$	1926	1963	2116	2592
$21/2^+$	2141	2162		

the same single particle intrinsic structure. These bands differ from the yrast band mainly by the values of K_{dom}. The band-head of the yrare band in ^{115}Rh has $I = 11/2$ and $K_{\text{dom}} = 11/2$ from the $[413]7/2^+$ orbital as in the yrast state, but $K_{\text{dom}} = \Omega + 2$. This means that $R_3 = 2$, which is a specific feature of a triaxially deformed nucleus. In an axially symmetric nucleus, the rotation vector $\boldsymbol{R}$ must be perpendicular to the symmetry axis. $R_3 = 2$ means that the rotation vector of the yrare states is oriented along a principal axis which is different from the one of the ground state. So triaxiality occurs in ^{115}Rh with $\gamma = 28°$.

4.4 Conclusion

In this chapter, the nuclear structures of two very neutron-rich isotopes ^{114,115}Rh have been studied. Two completely new high-spin level schemes are established for ^{114}Rh and ^{115}Rh, respectively, for the first time. Eight levels with twelve transitions in the $\Delta I = 1$, negative-parity yrast band and five levels with eight transitions in a side-band in ^{114}Rh are found. The level scheme is proposed to be built on a 7^- excited state. The signature inversion of the yrast bands of ^{106,112,114}Rh is observed at 13.7 $\hbar$ for ^{106}Rh, 12.5 $\hbar$ for ^{112}Rh, and 10.6 $\hbar$ for ^{114}Rh. It is likely that the triaxial deformation results in the signature inversion in these nuclei. The level scheme of ^{115}Rh has eight levels with thirteen transitions in the yrast band and five levels with eight transitions in the yrare band. The existence of the large signature splitting in the yrast band and an yrare band in ^{115}Rh shows features which are typical for triaxially deformed nuclei. Preliminary calculations based on the rigid-triaxial-rotor-plus-quasiparticle model have been performed and compared with the experimental results. Triaxiality with $\gamma = 28^\circ$ for ^{115}Rh is predicted. These results enrich our knowledge of Rh isotopes in the more neutron-rich region and pose new challenges to theory in this mass region.

CHAPTER V

LEVEL IDENTIFICATIONS AND SHELL-MODEL DESCRIPTIONS IN ^{134}I, ^{137}I, AND ^{139}Cs

5.1 Introduction

Studies of the structures of neutron-rich nuclei near the $Z = 50$, $N = 82$ doubly-magic ^{132}Sn core provide important tests for shell-model calculations employing realistic effective interactions. In particular, these data can be used to find out how far from the closed shells a shell-model interpretation is adequate for neutron-rich nuclei. Therefore, with a few valence protons beyond the $Z = 50$ closed shell and valence neutrons outside the $N = 82$ major shell, ^{134}I ($Z = 53, N = 81$) and two $N = 84$ isotones ^{137}I ($Z = 53$) and ^{139}Cs ($Z = 55$) are good candidates for this purpose.

A level scheme of ^{133}I was constructed from the ^{133}Te β decay and the ^{133}I isomeric decay [66]. High-spin states in $^{135-139}$I were examined from the spontaneous fission of ^{248}Cm [53, 54, 92–94]. Low-lying transitions in ^{134}I were observed from the ^{134}Te β decay [95, 96]. A 3.8(2) min isomer at 316.3 keV was reported in ^{134}I and tentatively assigned as 8^- with no level above it. The state has either a $\pi 1g_{7/2}\nu(1h_{11/2})^{-1}$ or $\pi 2d_{5/2}\nu(1h_{11/2})^{-1}$ configuration [97]. However, no higher-spin states in ^{134}I have been reported so far. A new high-spin level scheme of ^{134}I is built and theoretical calculations in the shell-model framework performed by our collaborators support our results.

The β decay of ^{139}Xe [66], fission of ^{252}Cf [61] and fission of ^{248}Cm [98] have been used to populate excited states in the ^{139}Cs nucleus. Thirteen transitions and eleven levels up to high spins in ^{139}Cs were identified by Nowak *et al.* [98]. In the present work, we confirm the yrast band of ^{139}Cs reported in Ref. [98] and extend it up to 4670 keV, by adding ten new excited levels with eighteen new deexciting transitions. Spins and parities of levels in ^{139}Cs are firmly assigned up to $25/2^+$ experimentally. The level pattern of ^{139}Cs indicates the validity of a shell-model description. Realistic shell-model calculations have been performed to interpret the spectrum of ^{139}Cs and good agreement between theory and experiment is found.

The energy levels in ^{137}I, an isotone of ^{139}Cs, are also extended with three new excited levels added on the top of the level scheme reported in Ref. [92] and the current shell-model calculations produce better results than those obtained in Ref. [92].

5.2 First identification of high-spin states in ^{134}I

Here, we report the first identification of high-spin states in ^{134}I, populated in the spontaneous fission of ^{252}Cf. By double gating on the previously known transitions in $^{111-113}$Rh [41], fission partners of ^{134}I, the transitions in ^{134}I can be identified.

Coincidence spectra are obtained by double gating on strong transitions in $^{111-113}$Rh, as shown in Fig. 5.1. The transition energies used for double gating in Rh isotopes are shown in Fig. 5.1. In Fig. 5.1, one sees a new 952.4-keV transition and the previously known strong transitions in ^{133}I [66], ^{135}I [53], ^{136}I [54], and ^{137}I [92]. By double gating on the new 952.4-keV transition observed in Fig. 5.1 and on a strong transition in each of the $^{111-113}$Rh isotopes, several new transitions of energies 640.2, 244.3, 752.5, and 785.5 keV are observed, as shown in Fig. 5.2. Figure 5.2 (c) clearly demonstrates the coincidence relationship between the 940.4-, 640.2-, 244.3-, 752.5-, and 785.5-keV transitions as well as with those in the Rh isotopes. Careful cross-checking of numerous coincidence spectra confirmed that this cascade consisting of the 952.4-, 640.2-, 244.3-, 752.5-, and 785.5-keV transitions exists and belongs to an iodine isotope.

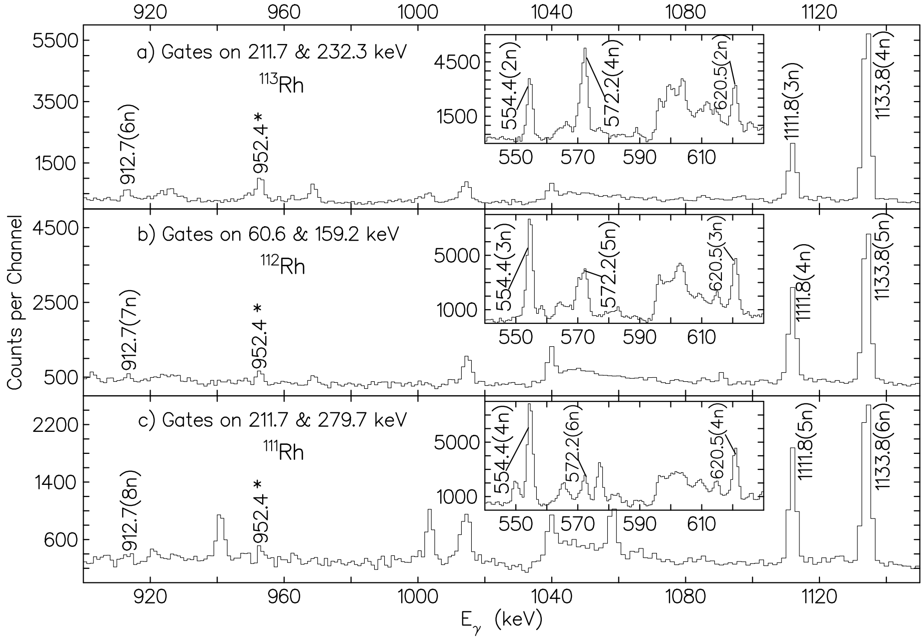

Figure 5.1: Coincidence spectra double gated on transitions in $^{111-113}$Rh [41]. The xn labels indicate transitions from an iodine isotope corresponding to the x neutron channel. A new transition of energy 952.4 keV is indicated in these spectra with an asterisk.

Since the high-spin level schemes of $^{133,135-139}$I are well known [53, 54, 66, 92–94], we propose that this cascade is in ^{134}I. A comparison of the relative intensities among the 952.4-keV transition, the 1133.8-keV transition in ^{135}I, and the 1111.8-keV transition in ^{136}I in different Rh gates (see Fig. 5.1) supports such a mass number assignment. The most important support is from the following measurements for

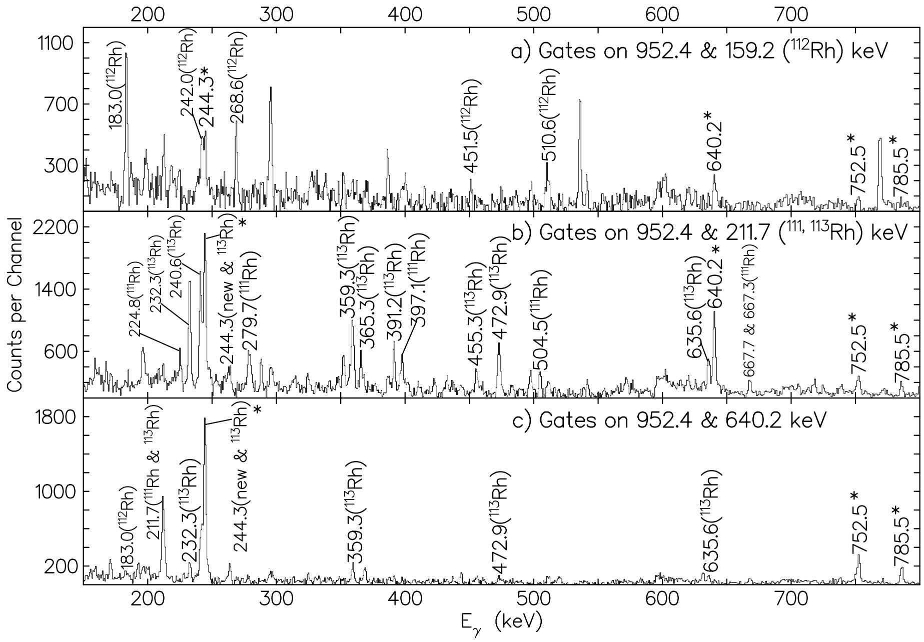

Figure 5.2: Coincidence spectra double gated on the new 952.4-keV transition and on the 159.2-, 211.7-keV transitions in Rh nuclei, and the new 640.2-keV transition. The transitions, marked with an asterisk, are newly identified.

the mass number assignment. In the 952.4/640.3-, 1133.8/288.2- (^{135}I), 1111.8/260.7- (^{136}I), and 620.5/488.2-keV (^{137}I) double gates, fission yield ratios of the 183.0-keV transition in ^{112}Rh to the 232.3-keV transition in ^{113}Rh are measured, as shown in Fig. 5.3. The variation of these ratios follows those of similar ratios of ^{105}Mo to ^{106}Mo in $^{142-145}$Ba double gates [66], which indicates that the mass number for the 640.3 → 952.4 cascade is below 135. The yrast level scheme of ^{133}I has been investigated very well [66] and most of the strongly populated transitions are also observed in our data, as presented in Fig. 5.4. Moreover, the fission yield of ^{132}I is much less than that of ^{134}I to exclude that this cascade belongs to ^{132}I. Therefore, the level scheme of ^{134}I is built with five new transitions for the first time, as shown in Fig. 5.5.

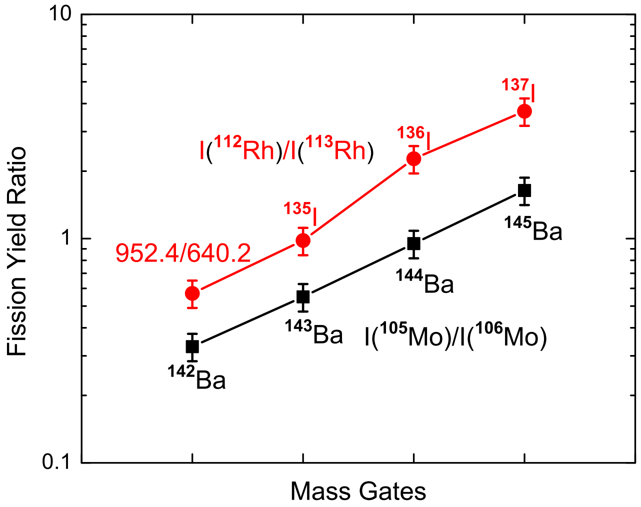

Figure 5.3: Fission yield ratios of ^{112}Rh to ^{113}Rh in the 952.4/640.3-keV and $^{135-137}$I gates along with those of ^{105}Mo to ^{106}Mo in $^{142-145}$Ba gates. A logarithmic scale is used for the y-axis. Data are taken from Refs. [53, 54, 66, 92] and the present work.

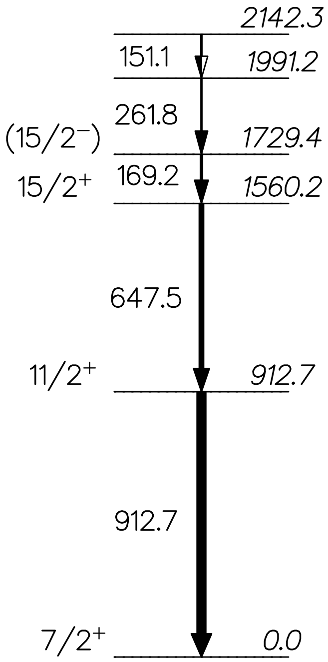

Figure 5.4: Partial level scheme of ^{133}I seen in our data. Energies are in keV and the width of the arrow is proportional to the corresponding γ-ray intensity.

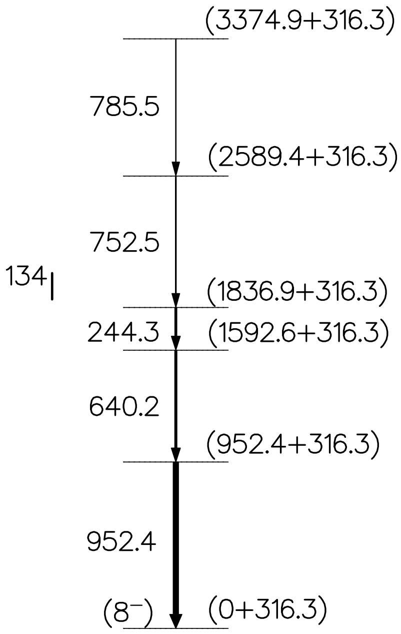

Figure 5.5: The new level scheme of ^{134}I identified for the first time. Energies are in keV and the width of the arrow is proportional to the corresponding γ-ray intensity. All transitions are new.

The ground state of ^{134}I was reported to be mainly built on the configuration of $\pi 1g_{7/2}\nu(2d_{3/2})^{-1}$ with a tentative spin-parity assignment of 4^+ [95]. A 3.8(2) min isomeric state at 316.3 keV in ^{134}I was reported and tentatively assigned to be either a $[\pi 1g_{7/2}\nu(1h_{11/2})^{-1}]_{8^-}$ or $[\pi 2d_{5/2}\nu(1h_{11/2})^{-1}]_{8^-}$ state [97]. The ground states of the $N = 81$ isotones ^{132}Sb ($Z = 51$) and ^{136}Cs ($Z = 55$) were reported to be $[\pi 1g_{7/2}\nu(2d_{3/2})^{-1}]_{4^+}$ [66] and $[\pi(1g_{7/2})^{-3}\nu(2d_{3/2})^{-1}]_{5^+}$ [99], respectively, and an 8^- isomeric state was found in both nuclei with the identical configuration of $\pi 1g_{7/2}\nu(1h_{11/2})^{-1}$ [66, 100]. For ^{132}I, a 4^+ ground state and an 8^- isomeric state were reported [66]. For ^{136}I, a 1^- ground state and a 6^- isomeric state were reported [66, 101] and high-spin states were proposed to be built on the 7^- state [54]. Therefore, it is most likely that the observed yrast cascade in ^{134}I in the present work is built on the 316.3-keV, 8^- isomeric state with a configuration of $\pi 1g_{7/2}\nu(1h_{11/2})^{-1}$. This configuration can be achieved by coupling a $1g_{7/2}$ proton from the ground state of ^{133}I to a $1h_{11/2}$ neutron hole from the ground state of ^{133}Te. This is supported by the fact that the spontaneous fission of ^{252}Cf mostly populates high-spin states.

The angular correlation for the 640.2- and 952.4-keV transitions in ^{134}I is measured by using the method described in Subsection 3.4.3. The measured A_2 and A_4 values for the 640.2 → 952.4-keV cascade are $-0.20(4)$ and $-0.02(5)$, respectively, as shown in Fig. 5.6. The theoretical A_2 and A_4 values of $\gamma-\gamma$ angular correlations are $A_2 = 0.102$ and $A_4 = 0.009$ for a pure quadrupole → quadrupole cascade, and $A_2 = -0.071$ and $A_4 = 0.0$ for a pure quadrupole → dipole cascade, and $A_2 = 0.05$ and $A_4 = 0.0$ for a pure dipole → dipole cascade [3, 5]. Comparisons of the experimental A_2 and A_4 values for the 640.2 → 952.4-keV cascade in ^{134}I with the theoretical ones listed above indicate that one or both of these two transitions are mixed.

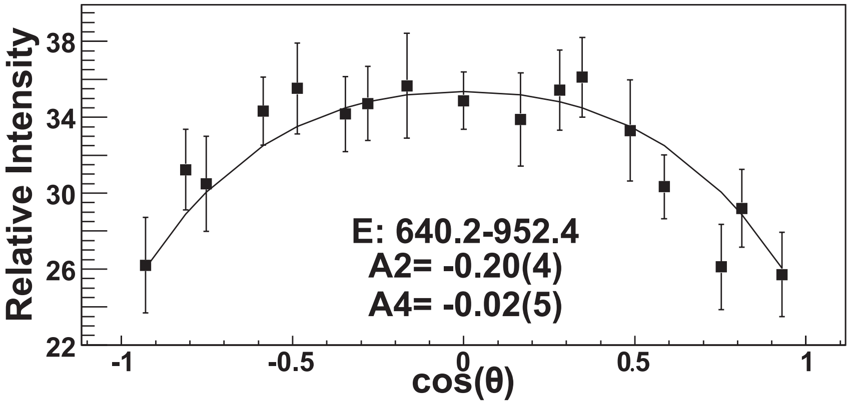

Figure 5.6: Angular correlation for the 640.2 → 952.4-keV cascade in ^{134}I.

Angular correlation measurements are also performed for transitions in ^{133}I, ^{135}I,

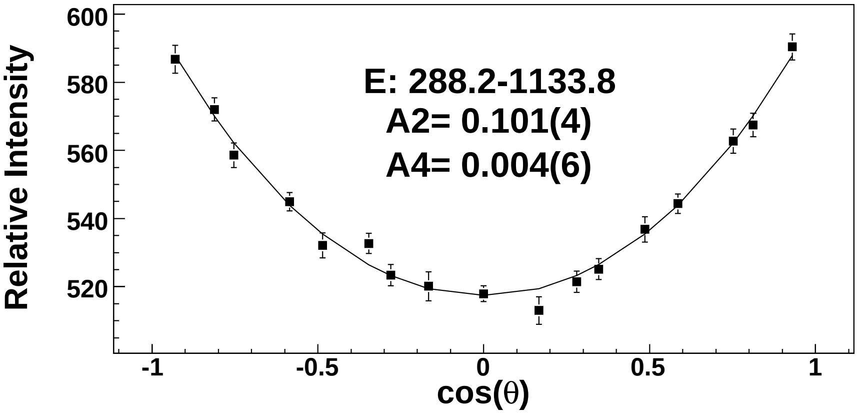

Figure 5.7: Angular correlation for the 288.2 → 1133.8-keV cascade in ^{135}I.

and ^{136}I for systematic comparisons. Figure 5.7 shows an example for the 288.2 → 1133.8-keV cascade in ^{135}I. These results are summarized in Table V.1 and are consistent with the theoretical $A_2 = 0.102$ and $A_4 = 0.009$ for a pure quadrupole → quadrupole cascade. These data establish that the 647.5- and 912.7-keV transitions in ^{133}I, the 288.2- and 1133.8- keV transitions in ^{135}I, and the 260.7- and 1111.8- keV transitions in ^{136}I are of pure $E2$ character. This conclusion confirms the tentative spin-parity assignments of $15/2^+ \rightarrow 11/2^+ \rightarrow 7/2^+$ to the 647.5 → 912.7-keV cascade in ^{133}I [66], $15/2^+ \rightarrow 11/2^+ \rightarrow 7/2^+$ to the 288.2 → 1133.8-keV cascade in ^{135}I [53] and $11^- \rightarrow 9^- \rightarrow 7^-$ to the 260.7 → 1111.8-keV cascade in ^{136}I [54]. However, the A_2 and A_4 values for the 640.2 → 952.4-keV cascade, and thus the multipolarities for these two transitions in ^{134}I do not follow the trend seen in ^{133}I, ^{135}I, and ^{136}I.

To determine the spin sequence of the 640.2 → 952.4-keV cascade in ^{134}I, plots of A_2 vs. A_4 using the mixing ratio δ as a parameter are shown in Fig. 5.8. Although the best fit for the spin sequence for the 640.2 → 952.4-keV cascade is 11 → 9 → 8 with the 952.4-keV transition mixed, 11 → 10 → 8 with the 640.2-keV transition mixed

Table V.1: Angular correlations measured in ^{133,135,136}I. Theoretical values of A_2^{theory} and A_4^{theory} of $\gamma-\gamma$ angular correlations for a pure quadrupole → quadrupole cascade are included.

Nucleus	Cascade (keV)	A_2^{exp}, A_4^{exp}	A_2^{theory}, A_4^{theory}
^{133}I	647.5 → 912.7	0.097(9), 0.006(9)	0.102, 0.009
^{135}I	282.2 → 1133.8	0.101(4), 0.004(6)	0.102, 0.009
^{136}I	260.7 → 1111.8	0.101(6), 0.009(10)	0.102, 0.009

and 10 → 9 → 8 with both the 640.2- and 952.4-keV transitions mixed which occurs in ^{132}Sb [102] are allowed.

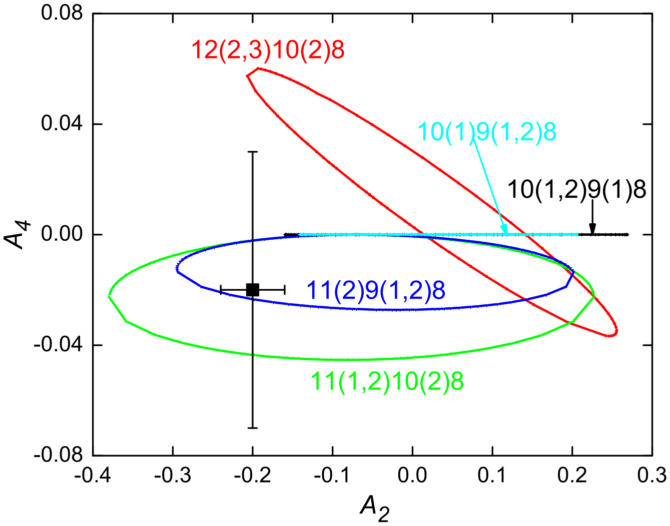

Figure 5.8: A_2 vs. A_4 for selected spin sequences using the mixing ratio δ as a parameter. The experimental A_2 and A_4 values for the 640.2 → 952.4-keV cascade in ^{134}I are shown. The theoretical A_2 and A_4 are taken from Refs. [3, 5].

Some yrast excitations in $^{133-136}$I are presented in Fig. 5.9. Their level spacings exhibit a strong shell effect of the $N = 82$ neutron major shell in ^{135}I, where the first transition has the largest transition energy. The energy of the first transition in ^{134}I ($N = 81$) lies between those of ^{133}I ($N = 80$) and ^{135}I ($N = 82$). The systematics also supports the mass number assignment of ^{134}I and its level order.

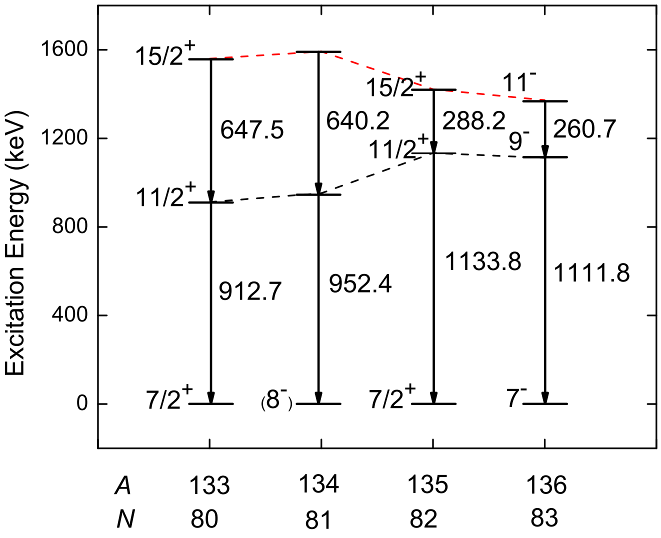

Figure 5.9: Some yrast states of $^{133-136}$I. Data are taken from [53, 54, 66] and the present work. Energies of the excited states in ^{134}I and ^{136}I are relative to the (8^-) state and the 7^-state, respectively.

Based on our experimental results, A. Covello and his collaborators have published a paper on shell-model calculations for ^{134}I [103]. Their results based on a realistic shell-model calculation are 0- (8^-), 1022- (10^-), 1674- (11^-), 1905- (12^-), 2439- (13^-), and 3142-keV (14^-) for the level energies. They are in good agreement with all level energies reported here with a root mean square deviation of about 100 keV, as shown in Fig. 5.10. As regards the nature of the states, it turns out that they are dominated by either the proton $\pi(1g_{7/2})^3$ $(8^-, 10^-, 13^-)$ or $\pi(1g_{7/2})^2(2d_{5/2})^1$ $(11^-, 12^-, 14^-)$ configuration, and the neutron hole being stably located in the $\nu 1h_{11/2}$ orbital. Our data support their shell-model calculations. Their results show that the 952.4-keV transition has a multipolarity of pure $E2$ while the 640.2-keV transition is of $E2/M1$ mixture, which are also consistent with our angular correlation measurement for the

640.2 → 952.4-keV cascade in ^{134}I.

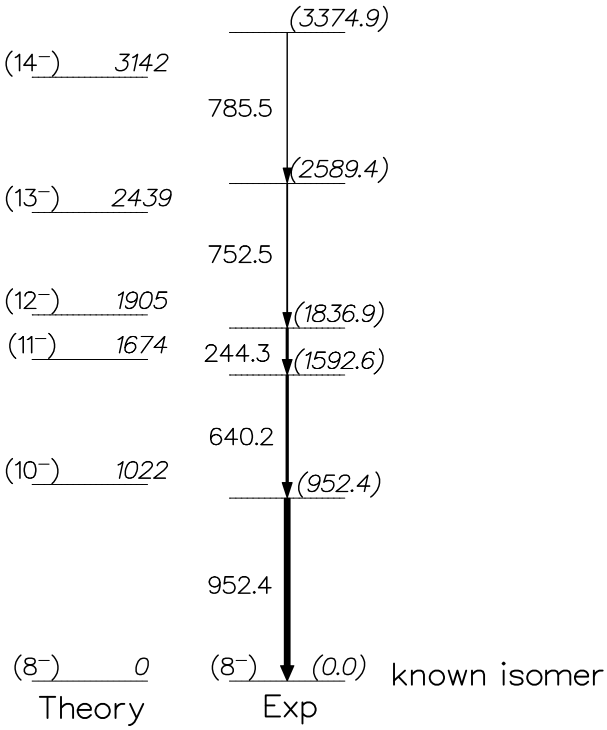

Figure 5.10: Comparison of shell-model calculations and the experimental results in ^{134}I. Energies are in keV.

5.3 High-spin structures of the neutron-rich nuclei ^{137}I and ^{139}Cs

5.3.1 Experimental results

Hwang *et al.* [61] claimed that the 218.6-, 408.6-, 618.4-, 387.5-, and 503.0-keV transitions compose the yrast cascade of ^{139}Cs based on the fact that a 218.64-keV transition was found from the β decay of ^{139}Xe to ^{139}Cs [66]. Later, Nowak *et al.* [98] reported that the transitions out of the yrast levels in ^{139}Cs have energies of 595.5, 601.5, 475.2, 468.5, 544.3, 428.2, 589.9, 236.6, 740.3, 756.3, and 727.6 keV and also supported the existence of the low-lying 218.6-keV transition.

To clarify the above dilemma, measurements to determine the mass number of the transitions have been performed. In the 595.5/475.2- (^{139}Cs) [98], 594.3/640.9- (^{140}Cs) [61], 369.5/481.0- (^{141}Cs) [60, 61, 104], 205.4/404.7- (^{142}Cs) [61], and 282.3/397.2-keV (^{143}Cs) [61, 104] double gates, the fission yield ratios of the 292.6-keV transition in ^{107}Tc [39, 61, 105] to the 154.1-keV transition in ^{108}Tc [61, 65] are measured to be 0.10(1), 0.16(2), 0.31(4), 0.47(7), and 1.25(18), respectively, as shown in Fig. 5.11. The variation of these ratios follows those of similar ratios of ^{105}Mo to ^{106}Mo in $^{141-145}$Ba double gates [66], which indicates that the mass number for the 475.2 → 595.5-keV cascade is below 140. Because the level schemes of ^{137,138}Cs have been well established [13, 106, 107], we argue that the 475.2 → 595.5-keV cascade belongs to the ^{139}Cs nucleus. In addition, we need to point out that the same ratio of ^{107}Tc to ^{108}Tc in the 218.6/408.6-keV [61] double gate is measured to be 0.49(7) which is consistent with the value in the ^{142}Cs gate, as shown in Fig. 5.11. This means that the 408.6 → 218.6-keV cascade forms a band in ^{142}Cs. The level structures of ^{140,142}Cs have been reported in Refs. [108, 109] and more details will be presented in Chapter VII. Note that the authors in Ref. [61] did not perform any measurement to determine the mass number of the 408.6 → 218.6-keV cascade. Rather, the assignment of this cascade to ^{139}Cs was solely based on the observation of a 218.64-keV transition in the β decay of ^{139}Xe to ^{139}Cs [66]. Because the spin-parity of the 218.64-keV level was assigned to be $5/2^+$ [110], it may not be populated in our fission data.

To demonstrate how we identify new transitions in ^{139}Cs, two coincidence spectra, created by double gating on transitions reported in Ref. [98], are shown in Fig. 5.12,

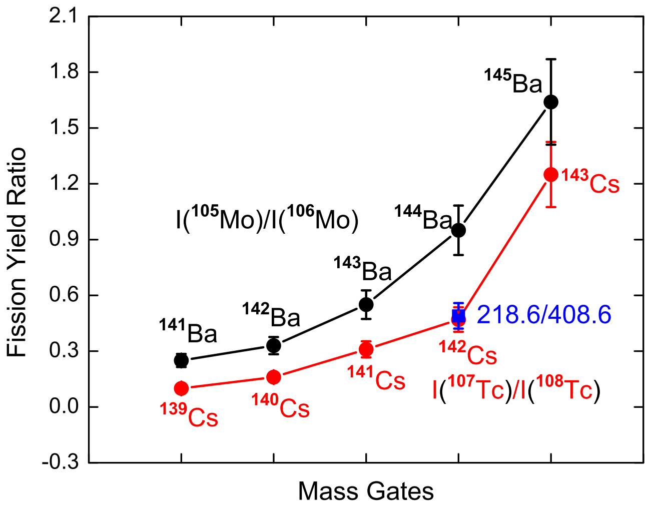

Figure 5.11: Fission yield ratios of ^{107}Tc to ^{108}Tc in Cs gates along with those of ^{105}Mo to ^{106}Mo in Ba gates. The same ratio of ^{107}Tc to ^{108}Tc in the 218.6/408.6-keV double gate is indicated with a solid square. Data are taken from Refs. [39, 61, 65, 66, 98, 104, 105]. For the data points of ^{139}Cs and ^{140}Cs, the uncertainties are smaller than the size of the solid circles.

where the transition energies used for double gating are also indicated. Both of these two spectra clearly show the coincidence relationship among transitions in ^{139}Cs and its partners ^{108}Tc [61, 65], ^{109}Tc [39, 61], and ^{110}Tc [40]. All of the previously known transitions in ^{139}Cs are confirmed, except the 914.9- and 1126.5-keV transitions feeding the 595.5-keV level reported in Ref. [98]. Those coincidence transitions, marked with an asterisk in Fig. 5.12, are newly observed. Two coincidence spectra are shown in Fig. 5.13, which provide additional support for our placements of the new transitions. The gate transitions are indicated in the spectra as well. The effort of extensive cross-checking with many other coincidence spectra leads to the final level identifications and placements in the ^{139}Cs nucleus. Ten new excited levels with eighteen new deexciting transitions are found to allow us to establish the level scheme of ^{139}Cs, as presented in Fig. 5.14, where excited states are extended up to 4670 keV. We have included the 218.6-keV level in our scheme in Fig. 5.14, because it was seen in the β defcay [66] and we will compare it with the corresponding calculated level energy in the next subsection.

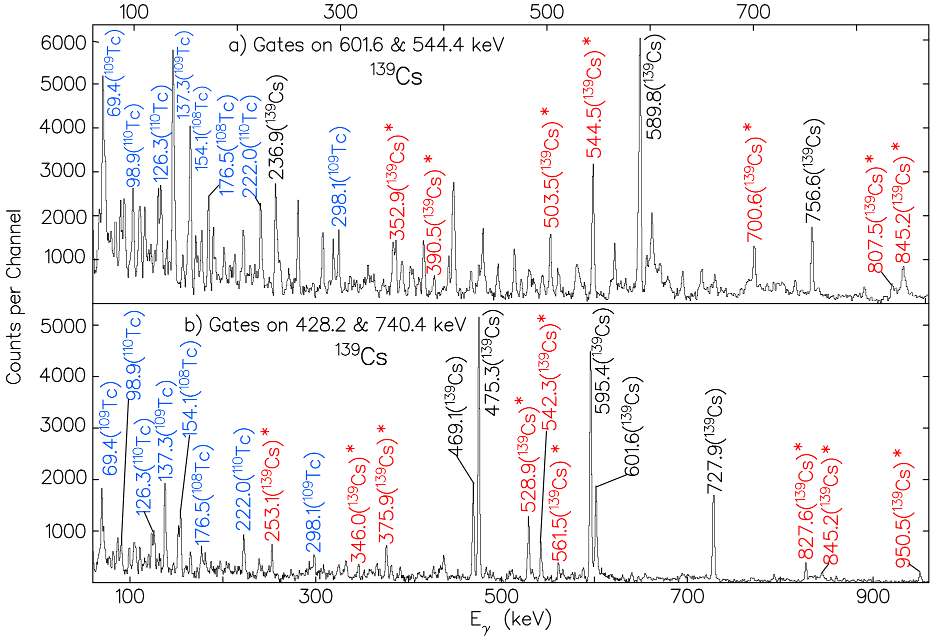

Figure 5.12: Coincidence spectra double gated on known transitions in ^{139}Cs [98]. The newly observed transitions are marked with an asterisk.

The spin-parity of the ground state of ^{139}Cs was reported as $7/2^+$ [66]. Spins and parities of the excited levels, as presented in Fig. 5.14, are determined by measuring the $\gamma - \gamma$ angular correlations for some transitions and the internal conversion coefficient of the 236.9-keV transition. Three examples of our angular correlation measurements in ^{139}Cs are shown in Figs. 5.15 - 5.17. The measured A_2 and A_4 values for the 428.2 $\rightarrow$ 475.3-, 740.4 $\rightarrow$ 428.2-, 727.9 $\rightarrow$ 740.4-, 544.4 $\rightarrow$ 601.6-, and 589.8 $\rightarrow$ 544.4-keV cascades, listed in Table V.2, are all consistent with the theoret-

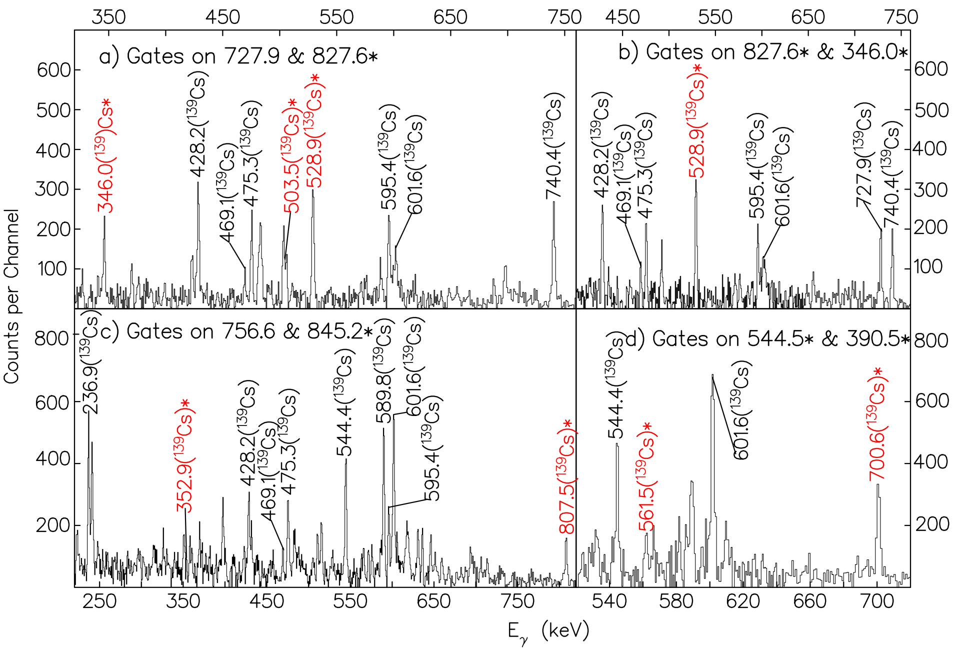

Figure 5.13: Coincidence spectra double gated on transitions in ^{139}Cs. The newly observed transitions are marked with an asterisk.

ical $A_2 = 0.102$ and $A_4 = 0.009$ for a pure quadrupole → quadrupole cascade [3, 5]. Therefore, these transitions are of pure quadrupole character. We propose that their multipolarities are $E2$ rather than $M2$ because the spontaneous fission process populates predominantly yrast levels and high-spin states and $E2$ transitions have been observed in the yrast bands of the neighboring even-even ^{138}Xe [111] and ^{140}Xe nuclei [112]. Another support for our proposal is from the half-life measurements, as described in Ref. [113], for the levels which the above transitions depopulate. No half-lives of more than 4 ns were observed for any of these levels in our data because no time effect on the transition intensities was found in our minimum 4 ns time window. Therefore, $11/2^+$, $15/2^+$, and $19/2^+$ are assigned to the 601.6-, 1146.0-, and 1735.8-keV levels, respectively.

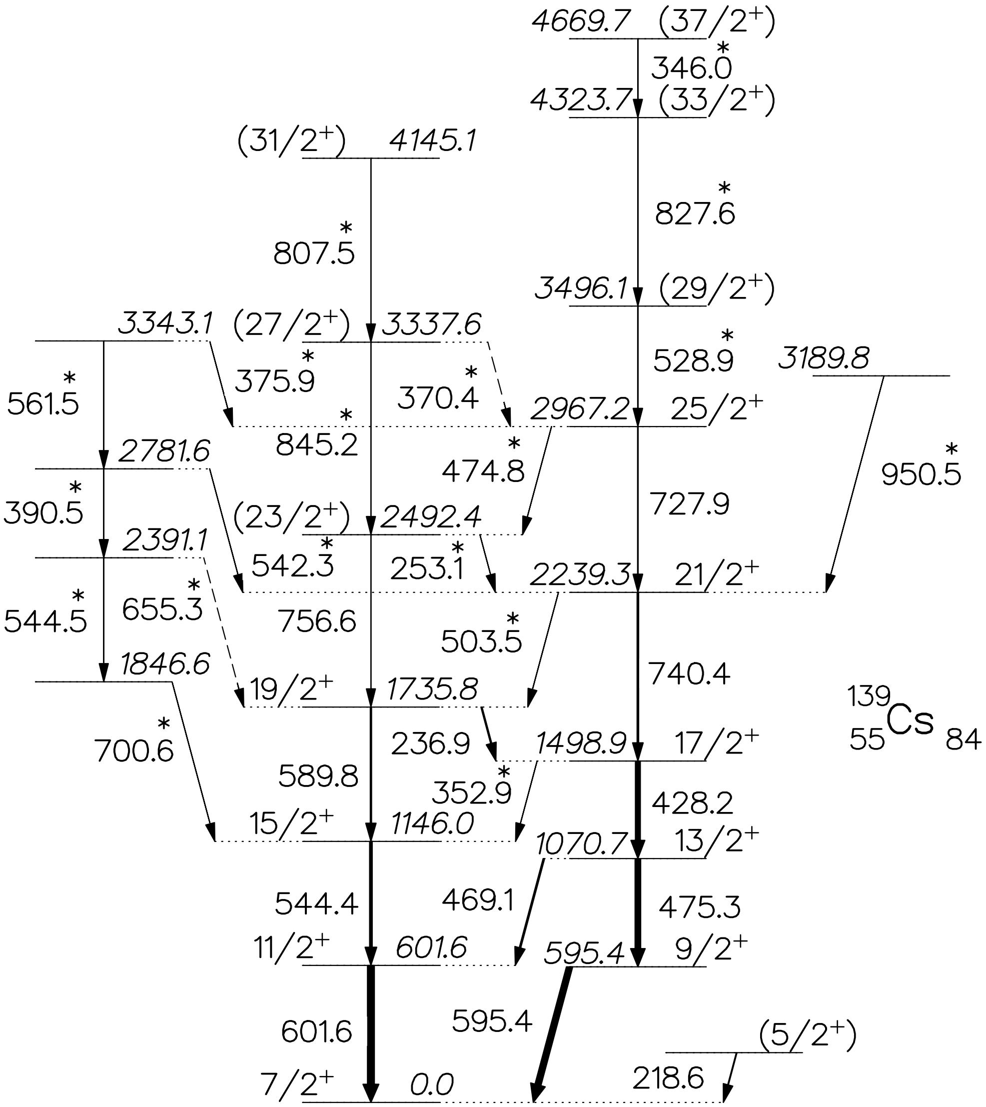

Figure 5.14: The new level scheme of ^{139}Cs. Energies are in keV and the width of the arrow is proportional to the corresponding γ-ray intensity. The transitions marked with an asterisk are newly observed. The 218.6-keV level is based on the β-decay study of Ref. [66].

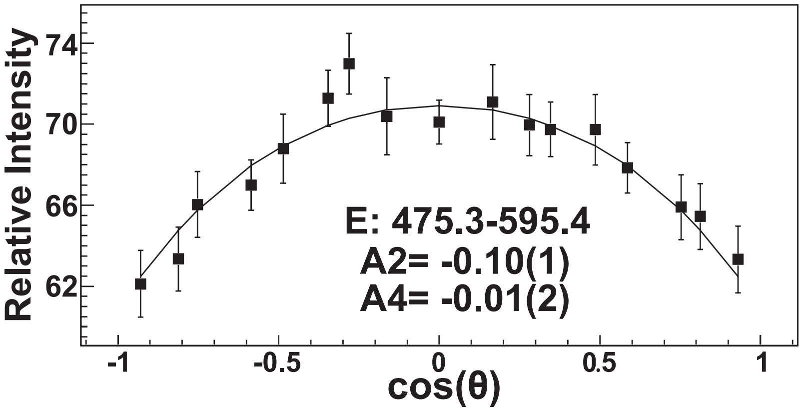

Figure 5.15: Angular correlation for the 475.3 → 595.4-keV cascade in ^{139}Cs.

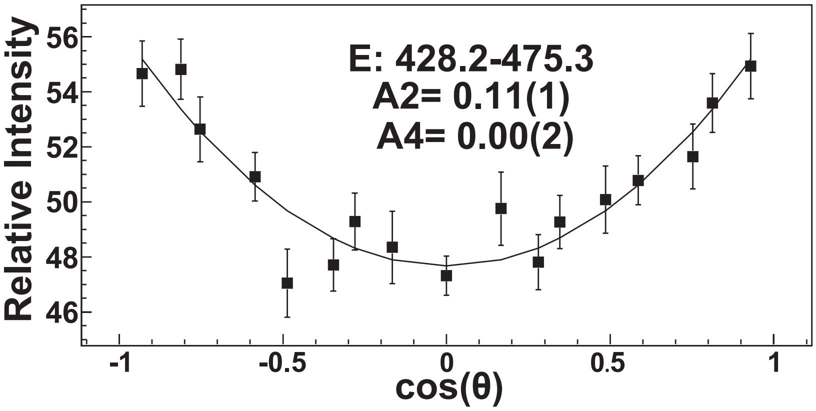

Figure 5.16: Angular correlation for the 428.2 → 475.3-keV cascade in ^{139}Cs.

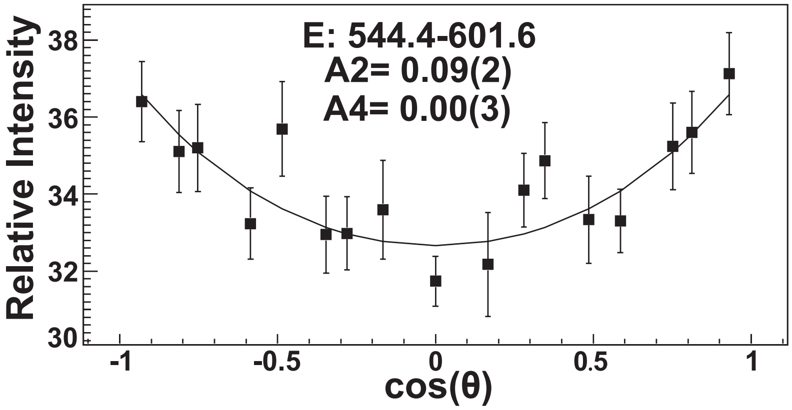

Figure 5.17: Angular correlation for the 544.4 → 601.6-keV cascade in ^{139}Cs.

Table V.2: Angular correlations measured in ^{139}Cs. The theoretical A_2 and A_4 values of $\gamma-\gamma$ angular correlations for a pure quadrupole → quadrupole cascade are included.

Cascade (keV)	A_2^{exp}, A_4^{exp}	A_2^{theory}, A_4^{theory}
428.2 → 475.3	0.11(1), 0.00(2)	0.102, 0.009
740.4 → 428.2	0.11(2), -0.02(3)	0.102, 0.009
727.9 → 740.4	0.11(3), -0.01(4)	0.102, 0.009
544.4 → 601.6	0.09(2), 0.01(3)	0.102, 0.009
589.8 → 544.4	0.10(4), -0.00(7)	0.102, 0.009
475.3 → 595.4	-0.10(1), -0.01(2)	see text

Because the spin of the 601.6-keV level is assigned as 11/2, the spin of the 595.4-keV level should be either 9/2 or 11/2 due to its high-spin feature and yrast structure. If the spin is 11/2, the spin difference between this level and the ground state will be two, which results in a conclusion that the multipolarity of the 595.4-keV transition is $E2$, $M2$, $E3$, or $M3$. However, the very low transition probabilities of $E3$ and $M3$ rule out the possibility of their existence. The impossibility of $E3$ and $M3$ is also supported by the experimental A_2 value because the minimum theoretical A_2 value -0.05 [3, 5] for the $15/2(Q)11/2(Q,O)7/2$ cascade is not nearly as large negatively as the experimental A_2 value $-0.10(1)$ as shown in Fig. 5.15. If the 595.4-keV transition is of pure quadrupole character for an 11/2 assignment, then the A_2 and A_4 values should be 0.102 and 0.009 for a pure quadrupole → quadrupole cascade, which conflicts with these experimental results of $A_2 = -0.10(1)$ and $A_4 = -0.01(2)$. Thus, the spin of the 595.4-keV level is assigned as 9/2. Then, the parity of the levels in the 475.3 → 595.4-keV cascade is obtained from the total internal conversion coefficient (α_{T}) of the 236.9-keV transition. The measured α_{T} of a specific transition can be used to determine its multipolarity and thus the spin-parities of the two levels connected by this transition.

The α_{T} of a low-energy transition can be measured from the intensity balance in and out of a state which this transition feeds or depopulates, by double gating on two other transitions in the same cascade. The total internal conversion coefficient of the 236.9-keV transition is measured to be 0.086(12) by double gating on the 756.6- and 475.3-keV transitions and then calculating the difference between the relative γ-ray intensity of the 236.9-keV transition and that of the 428.2-keV transition, with an assumption that the α_{T} of the 428.2-keV transition is negligible. Theoretical values are computed as $\alpha_{\mathrm{T}}(E1) = 0.020$, $\alpha_{\mathrm{T}}(M1) = 0.083$, $\alpha_{\mathrm{T}}(E2) = 0.094$, and $\alpha_{\mathrm{T}}(M2) = 0.42$, respectively, by using the BrIcc v2.2b Conversion Coefficient Calculator [7]. Comparisons of the experimental α_{T} value with the calculated ones indicate that the multipolarity of the 236.9-keV transition is $M1$ and/or $E2$. So, the parity of the 1498.9-keV level is the same as that of the 1735.8-keV level. With an eye to the results in the above paragraph, the parity of the levels in the 475.3 → 595.4 cascade should be positive. Thus, a spin-parity of $9/2^+$ is assigned to the 595.4-keV level, which confirms the tentative assignment in Ref. [98]. The $E2/M1$ mixture of the 595.4-keV transition, consistent with the character of the 554.4-keV transition in its isotone ^{137}I [92], will be discussed below. Finally, the spins and parities of the levels of energies 1070.7, 1498.9, 2239.3, and 2967.2 keV are determined to be $13/2^+$, $17/2^+$, $21/2^+$, and $25/2^+$, respectively.

The spins and parities of other upper yrast levels are tentatively assigned by assuming that the spin values increase with increasing excitation energies in the spontaneous fission and the transitions are of $E2$ character. As we shall discuss in the following subsection, shell-model calculations confirm these assignments. In the same subsection, a tentative identification is made for those states whose spins and parities cannot be assigned in our experimental data.

Figure 5.18 shows the level scheme of ^{137}I observed in the present work. The level scheme is almost the same as the one reported by Korgul *et al.* [92], except that we add three new excited levels with four new deexciting transitions on the top. In this figure, we have also reported the results of the present shell-model calculations, which will be discussed in the next subsection. The spectra in Fig. 5.19 indicate the coincidence relationship among the new and known transitions in ^{137}I. We adopt the spin-parity assignments in Ref. [92], where angular correlation measurements were performed. The spins and parities of the three new levels are assigned, by assuming that the transitions linking these levels are of $E2$ character.

Because both the 595.4-keV transition in ^{139}Cs and 554.4-keV transition in ^{137}I [92] are $E2/M1$ mixed, it is worth measuring their mixing ratio (δ) values. As shown in Fig. 5.15, the measured A_2 and A_4 values for the 475.3 $\rightarrow$ 595.4-keV cascade in ^{139}Cs are $-0.10(1)$ and $-0.01(2)$, respectively, which produce two minimum values of the mixing ratio of the $9/2^+ \rightarrow 7/2^+$, 595.4-keV transition as $\delta = -4.2^{+0.4}_{-0.5}$ and $\delta = -0.07^{+0.02}_{-0.02}$, by using the DELTA program from the National Nuclear Data Center [66]. The measured A_2 and A_4 values for the 400.4 $\rightarrow$ 554.4-keV cascade in ^{137}I are -0.24(1) and -0.01(1), respectively, as presented in Fig. 5.20, which are consistent with the experimental results of $A_2 = -0.233(6)$ and $A_4 = -0.033(7)$ in Ref. [92]. Our A_2 and A_4 values also give two minimum δ values for the $9/2^+ \rightarrow 7/2^+$, 554.4-keV transition in ^{137}I, as $\delta = -1.3^{+0.2}_{-0.1}$ and $\delta = -0.55^{+0.07}_{-0.10}$. As will be seen in the next subsection, the δ values, which favor an $E2$ character for both the 595.4- (^{139}Cs)

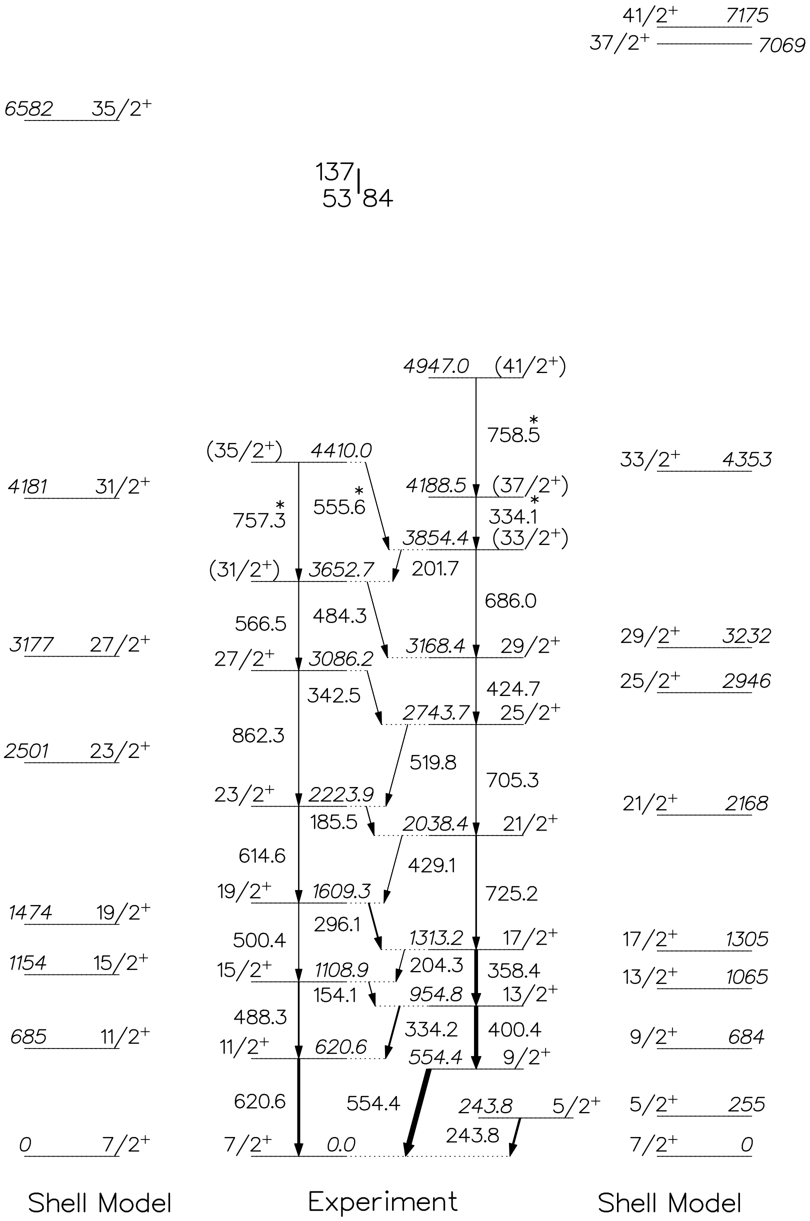

Figure 5.18: The new level scheme of ^{137}I. Energies are in keV and the width of the arrow is proportional to the corresponding γ-ray intensity. Four new transitions observed here are marked with an asterisk. Predictions from shell-model calculations are shown as well.

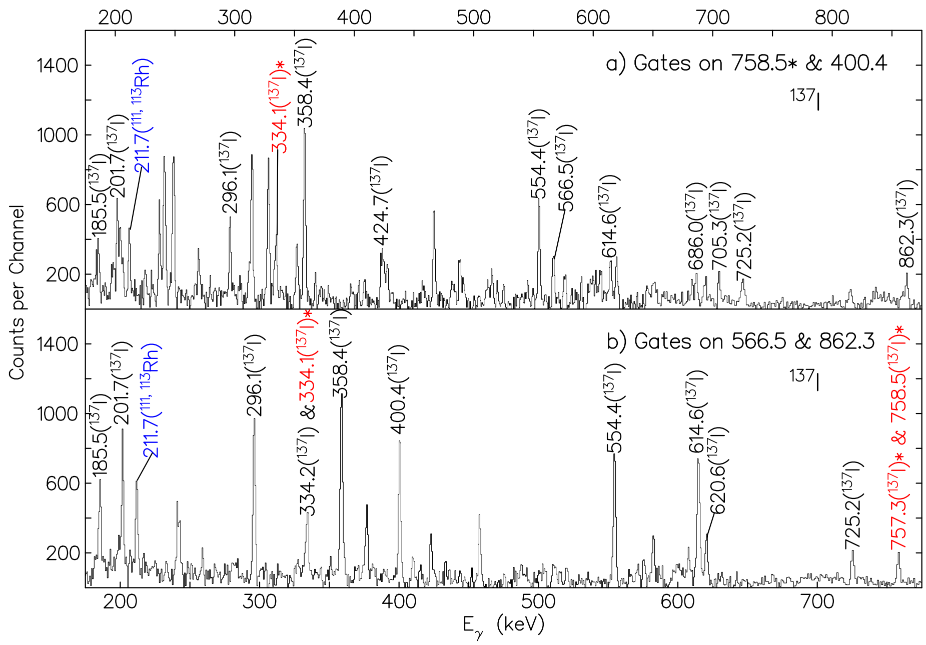

Figure 5.19: Coincidence spectra double gated on transitions in ^{137}I. The newly observed transitions are marked with an asterisk.

and 554.4-keV (^{137}I) transitions, are reproduced very well by the present shell-model calculations.

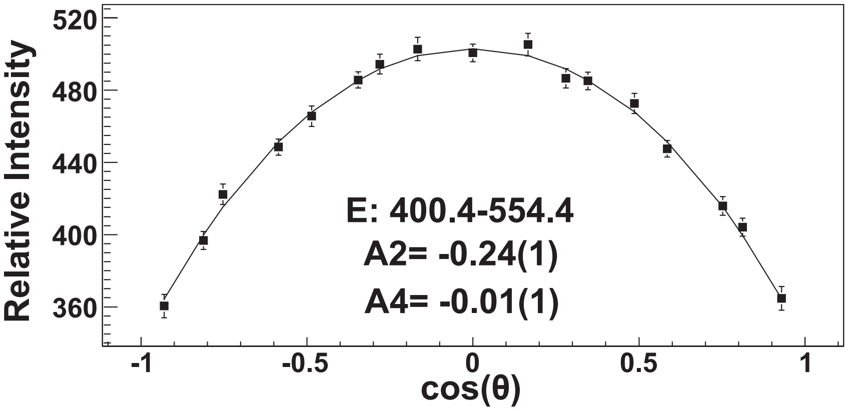

Figure 5.20: Angular correlation for the 400.4 → 554.4-keV cascade in ^{137}I.

5.3.2 Discussion and shell-model calculations

The systematics of the odd-A $^{133-141}$Cs nuclei [61,66,104] are presented in Figs. 5.21 and 5.22. Excitation energies of the first $5/2^+$ states and some other yrast states in these isotopes are shown in Fig. 5.21. Their level patterns indicate a strong shell effect in ^{137}Cs ($N = 82$). Variations of the excitation energies of the $11/2^+$ states of these odd-A Cs isotopes vs the excitation energies of the first 2^+ states of the corresponding even-even Xe cores [66] are shown in Fig. 5.22. We see a nearly linear relationship, which indicates that yrast states in these odd-A $^{133-141}$Cs are formed from coupling the valence proton to the corresponding Xe core.

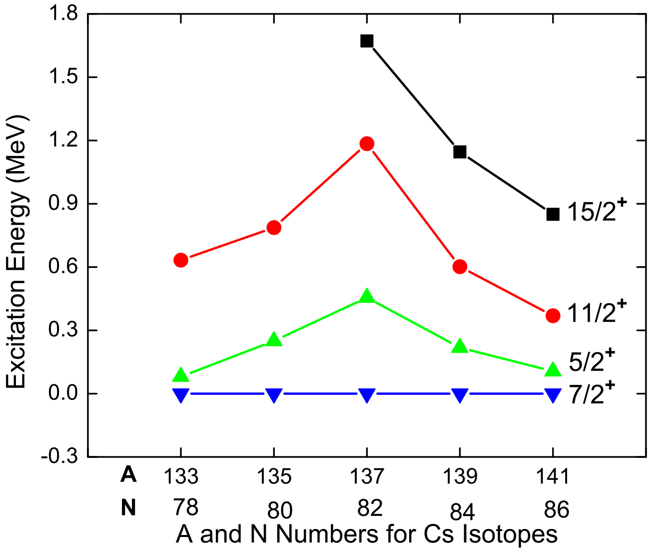

Figure 5.21: Excitation energies of the first excited $5/2^+$ states and some other yrast states of odd-A $^{133-141}$Cs. Data are taken from Refs. [13, 60, 66, 104] and the present work.

The systematics of the odd-A, $N = 84$ isotones, ^{135}Sb [114], ^{137}I [92], ^{139}Cs, and ^{141}La [66], are presented in Figs. 5.23 and 5.24. Excitation energies of the same

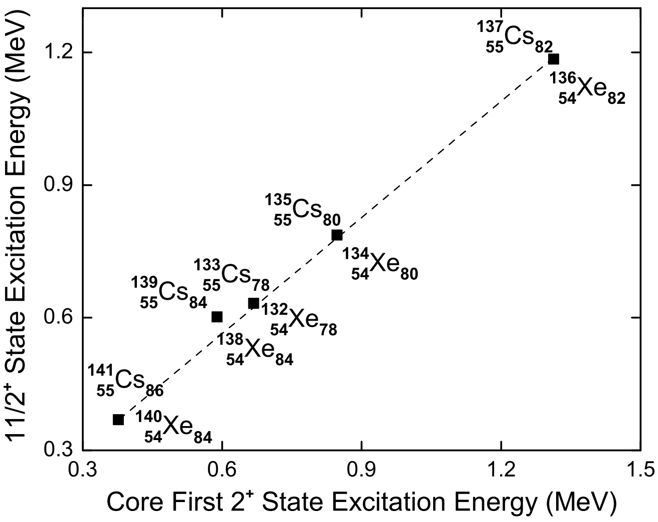

Figure 5.22: Excitation energies of the $11/2^+$ states of the odd-A $^{133-141}$Cs nuclei vs those of the first 2^+ states of the corresponding even-even Xe cores. A dashed line is drawn to indicate the linear relationship of these data. Data are taken from Refs. [13, 60, 66, 104] and the present work.

yrast states as shown in Fig. 5.21 are presented in Fig. 5.23, where a similarity is observed in their level patterns. Variations of the excitation energies of the yrast $11/2^+$ states of ^{135}Sb, ^{137}I, and ^{139}Cs vs the excitation energies of the first 2^+ states of the corresponding ^{134}Sn, ^{136}Te, and ^{138}Xe cores [111], as presented Fig. 5.24, show an almost linear relationship, which also indicates that yrast states of ^{135}Sb,^{137}I, and ^{139}Cs are formed from coupling the valence proton to the corresponding even-even core. Although the $11/2^+$ state of ^{141}La has not been observed so far, one can predict its position as roughly at 600 keV, based on the excitation energies of the same state of ^{135}Sb, ^{137}I, and ^{139}Cs and that of the first 2^+ state of ^{140}Ba [115].

On the above grounds, a shell-model study has been conducted for ^{139}Cs, with five valence protons outside the $Z = 50$ closed shell and two valence neutrons beyond the $N = 82$ major shell. Levels in ^{139}Cs are spaced somewhat more evenly than in

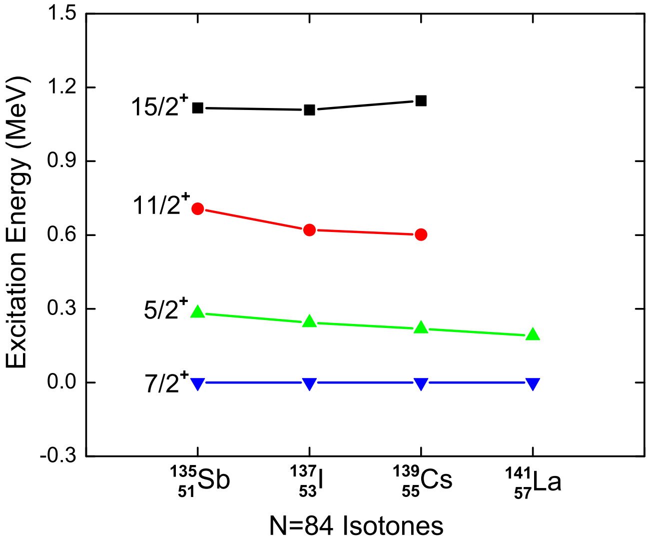

Figure 5.23: Excitation energies of the first excited $5/2^+$ states and some other yrast states of ^{135}Sb, ^{137}I, ^{139}Cs, and ^{141}La. Data are taken from Refs. [66, 92, 114] and the present work.

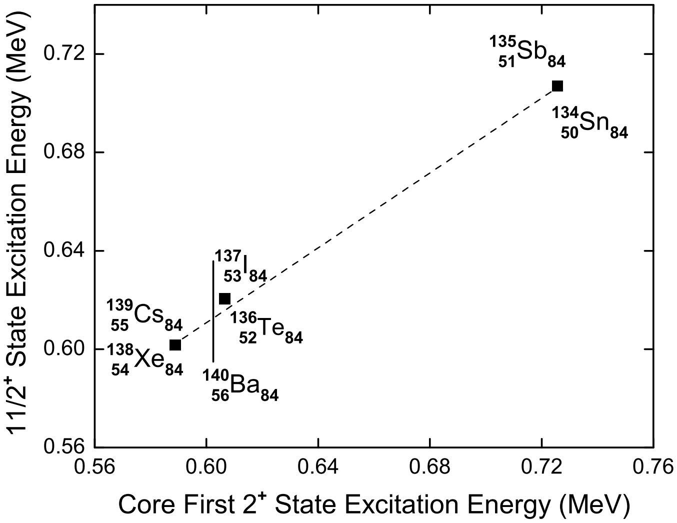

Figure 5.24: Excitation energies of the yrast $11/2^+$ states of ^{135}Sb, ^{137}I, and ^{139}Cs vs those of the first 2^+ states of the corresponding even-even ^{134}Sn, ^{136}Te, and ^{138}Xe cores. The excitation energy of the first 2^+ state of ^{140}Ba is also indicated. A dashed line is drawn to indicate the linear relationship of these data. Data are taken from Refs. [66, 92, 111, 114, 115] and the present work.

^{137}I, which may suggest that the addition of two protons to ^{137}I induces a change towards a collective motion. However, as we shall see in the following, a shell-model description of ^{139}Cs turns out to be quite successful.

We consider ^{132}Sn as a closed core, with the valence protons occupying the five levels $0g_{7/2}$, $1d_{5/2}$, $1d_{3/2}$, $1s_{1/2}$, and $0h_{11/2}$ of the $50-82$ shell, and the two valence neutrons the six levels $0h_{9/2}$, $1f_{7/2}$, $1f_{5/2}$, $2p_{3/2}$, $2p_{1/2}$, and $0i_{13/2}$ of the $82-126$ shell. The same shell-model Hamiltonian was used as that employed in recent studies on ^{132}Sn neighbors with $N > 82$, which yielded results in very good agreement with experiment [116]. Here we only mention that the two-body effective interaction contained in this Hamiltonian was derived from the CD-Bonn nucleon-nucleon potential with the inclusion of the Coulomb force for protons. A brief discussion of the derivation of the two-body matrix elements can be found in Ref. [117], where the adopted values of the single-proton and -neutron energies were also given. These were taken from the experimental spectra of ^{133}Sb and ^{133}Sn [66], respectively, with the exception of the proton $1s_{1/2}$ and the neutron $0i_{13/2}$ levels, which are still missing. The calculations have been carried out using the OSLO shell-model code [118].

Let us start by considering the three-valence-proton nucleus ^{137}I. As mentioned above, the level scheme observed in the present experiment is almost the same as that of Ref. [92] but with three new levels as shown in Fig. 5.18, where the calculated levels are also reported. From Fig. 5.18, one sees that the agreement between theory and experiment is very good up to the $29/2^+$ state, the discrepancy ranging from a few keV to 280 keV, while for the $31/2^+$ and $33/2^+$ states, the theoretical energies are higher by about 500 keV. We see that the three highest-spin levels are predicted to be located more than 2 MeV above the experimental ones. This may indicate that excitations outside the chosen model space play an important role for such high-spin states.

In the work of Ref. [92], a shell-model calculation was also performed to interpret the observed spectrum of ^{137}I. The significant discrepancies occurring between some theoretical and experimental energies were seen as an indication that the excitation pattern of ^{137}I deviates from the shell-model scheme. This was essentially based on the prediction of a $29/2^+$ isomer, which was not observed in their experiment.

The present calculation differs from that of Ref. [92] in that a modern realistic two-body interaction and a larger model space are used. This produces on the whole a better agreement with experimental data. On this basis, we come to the conclusion that an accurate description of ^{137}I may be obtained within the shell-model framework. As for the $29/2^+$ state, we find that this state, dominated by the $\pi(g_{7/2})^2 d_{5/2} \nu(f_{7/2})^2$ configuration, lies above the $27/2^+$ and $25/2^+$ levels and decays to the latter with a transition probability of 5×10^9 s^{-1}. This corresponds to a $B(E2; 29/2^+ \rightarrow 25/2^+)$=317 e^2fm^4, obtained with $e_\pi^{\rm eff} = 1.55e$ and $e_\nu^{\rm eff} = 0.7e$ [119]. It turns out that the transition to the $27/2^+$ state is hindered by a factor of about 100, which is mainly due to the small energy gap. In this case, we have $B(E2)$= 18 e^2fm^4 and $B(M1)$= 0.005 $\mu_{\rm N}^2$, the latter being obtained with the effective $M1$ operator of Ref. [117]. Note that this operator and the above effective charges are just the same as those used for all neighbors near ^{132}Sn (see, for instance, Ref. [120]).

In the same way, we have also calculated the mixing ratio δ for the $9/2^+ \rightarrow 7/2^+$, 554.4-keV transition in ^{137}I. We find $\delta = -3.9$, which comes rather close to the value $-1.3^{+0.2}_{-0.1}$ obtained experimentally, indicating that this transition is mainly of $E2$ character.

Note that between the $9/2^+$ and $7/2^+$ states a $5/2^+$ state is observed at 243.8 keV. We predict the first $5/2^+$ state at 255 keV and find $B(E2; 9/2^+ \rightarrow 5/2^+) = 81\ e^2\mathrm{fm}^4$ corresponding to a transition probability of about $3 \times 10^8\ \mathrm{s}^{-1}$. This makes the feeding of this state not competitive with respect to that of the $7/2^+$ state, in agreement with the finding of the present work. A second $5/2^+$ state is predicted by our calculation at only 130 keV above the yrast one, for which the $B(E2; 9/2^+ \rightarrow 5/2^+)$ value turns out to be 270 $e^2\mathrm{fm}^4$. However, the deexcitation of the $9/2^+$ state to this state is also unlikely owing to the small energy of the γ-ray involved.

Before starting to discuss our results for ^{139}Cs, we would like to mention the work of Ref. [117], which reported a shell-model study on the lighter $N = 84$ isotone ^{135}Sb having only one valence proton. In recent years, this nucleus has been the subject of much theoretical and experimental interest (see, for instance, Ref. [119]). A low-lying $5/2^+$ state was identified [121, 122], whose position appeared to be anomalous when looking at the systematics of the odd-even lighter Sb isotopes. In Ref. [117], it was shown that a shell-model calculation with the same effective Hamiltonian as the present study accounts for the observed properties of the yrast $5/2^+$ state in ^{135}Sb as well as for the energies of the other observed levels.

It is interesting to note the similarity between the ^{135}Sb and ^{137}I levels. Basically, a low-energy $5/2^+$ state is present in both nuclei and a correspondence can be established between the $7/2^+$, $11/2^+$, $15/2^+$, $19/2^+$, and $23/2^+$ states of ^{135}Sb identified in the ^{248}Cm fission experiment [114] and the members with the same angular momentum and parity of one of the two $\Delta I = 2$ cascades observed in ^{137}I. As for the other cascade, the $9/2^+$ state has been identified in ^{135}Sb from the β decay of ^{135}Sn [123].

Also we note the work in Refs. [124, 125], where theoretical calculations based on the shell model for ^{137}I and the particle-plus-rotor model for ^{137}I and ^{139}Cs were reported, respectively. In Ref. [124], the authors did shell-model calculations for ^{137}I using the same model space as ours, but with the empirical interaction SMN, an empirical Hamiltonian which was obtained by some modifications of a Hamiltonian (CW5082) originally derived from the ^{208}Pb region. Overall agreement of their shell-model calculations with the experiment in ^{137}I was found and the differences between their calculated and experimental level energies were considerably smaller for the states from $21/2^+$ to $33/2^+$ than ours. However, their calculations did not reproduce the correct order of the $9/2^+$ and $11/2^+$ states which we do. We also reproduce the $15/2^+ \rightarrow 13/2^+$ and $19/2^+ \rightarrow 17/2^+$ splitting better than Ref. [124]. Interestingly, we find that the first $5/2^+$ state is dominated (50%) by the $\pi(g_{7/2})^2 d_{5/2} \nu(f_{7/2})^2$ configuration, while a different one $\pi(g_{7/2})^3 \nu(f_{7/2})^2$ was predicted in Ref. [124]. Moreover, the three new higher-spin levels seen in our data indicate that more shell-model orbitals are required to be chosen to interpret higher-spin levels in ^{137}I in the shell-model framework, as also found in ^{139}Cs discussed next. The wave functions in the levels in ^{137}I show somewhat large configuration mixing which may lead to mild collectivity. Therefore, particle-plus-rotor-model calculations for ^{137}I were performed in Ref. [125], where the order of the $9/2^+$ and $11/2^+$ levels was predicted correctly. However, their calculations did not reproduce the energy splitting for higher-spin levels in ^{137}I very well.

Our level scheme of ^{139}Cs is shown in Fig. 5.14. In Table V.3, we compare the experimental excitation energies with the calculated values for the levels with assigned spin-parities. As the case for ^{137}I, the agreement between the calculated and experimental energies is very good for all states up to $I^{\pi} = 29/2^{+}$, the discrepancies ranging from few tens of keV up to about 200 keV. As for the $31/2^{+}$ and $33/2^{+}$ states, the discrepancies reach about 300 keV, while the $37/2^{+}$ state is predicted to lie at more than 1 MeV above the observed one. The reason for this large discrepancy again may be that excitations outside the chosen model space play an important role for such a state, as also found for ^{137}I.

Table V.3: Experimental and calculated excitation energies (in MeV) for ^{139}Cs.

I^{π}	E^{exp}	E^{theory}	I^{π}	E^{exp}	E^{theory}
$7/2^{+}$	0.00	0.00	$21/2^{+}$	2.239	2.338
$5/2^{+}$	0.219	0.159	$23/2^{+}$	2.492	2.691
$9/2^{+}$	0.595	0.710	$25/2^{+}$	2.967	3.100
$11/2^{+}$	0.602	0.688	$27/2^{+}$	3.338	3.406
$13/2^{+}$	1.071.	1.141	$29/2^{+}$	3.496	3.472
$15/2^{+}$	1.146	1.192	$31/2^{+}$	4.145	4.464
$17/2^{+}$	1.499	1.426	$33/2^{+}$	4.324	4.593
$19/2^{+}$	1.736	1.607	$37/2^{+}$	4.670	5.824

It is interesting to see that the structures of the level schemes observed in the two lighter isotones, ^{135}Sb and ^{137}I, persist in ^{139}Cs with two more valence protons. As regards the mixing ratio for the $9/2^{+} \rightarrow 7/2^{+}$, 595.4-keV transition in ^{139}Cs, our calculated value of $\delta = -3.6$ comes close to that predicted for ^{137}I and to the experimental value $-4.2^{+0.4}_{-0.5}$, which favors an $E2$ character for this transition.

Finally, let us come to the observed levels of ^{139}Cs shown in Fig. 5.14, to which no spin-parity can be assigned from our experimental data. These cannot be uniquely matched by a sequence of theoretical states. We therefore report in Table V.4 the predicted excitation energies of the second and third states with I^π from $15/2^+$ up to $27/2^+$, which are the most probable candidates for their identification. Based on this table, an attempt at identification can be made if we do not go beyond the second excited states and consider only $M1$ and/or $E2$ transitions. With these assumptions, we may establish a correspondence between the experimental levels at 1.847, 2.391, 2.782, 3.190, and 3.343 MeV and the calculated ones from $I^\pi = 19/2^+$ up to $I^\pi = 27/2^+$. In this case, the discrepancy between theory and experiment turns out to be about 100 keV for all levels, except the $19/2^+$ for which it is around 500 keV. Clearly, for a safer interpretation more experimental data are needed.

Table V.4: Calculated excitation energies (in MeV) of the second and third levels with I^π from $15/2^+$ up to $27/2^+$ in ^{139}Cs.

I^π	$15/2^+$	$17/2^+$	$19/2^+$	$21/2^+$	$23/2^+$	$25/2^+$	$27/2^+$
The second level	1.484	1.533	2.345	2.523	2.897	3.265	3.468
The third level	1.753	1.941	2.391	2.682	3.179	3.365	3.673

Using the particle-plus-rotor model for ^{139}Cs, the authors in Ref. [125] predicted two new levels, $27/2^+$ at 3142 keV and $29/2^+$ at 3693 keV, which were unknown in experiment at that time . These two states may be compared to our new levels at 3337.6 and 3496.1 keV with their spins and parities. Their agreement between theory and experiment is as good as ours at low spin but the present shell-model calculations give better energy splitting than they found, especially at high spin above $15/2^+$.

5.4 Conclusion

In this chapter, the new level schemes of ^{134}I and two $N = 84$ isotones, ^{137}I and ^{139}Cs, which have a few nucleons outside the doubly-magic core ^{132}Sn, are presented.

We establish a new high-spin level scheme of ^{134}I for the first time. These high-spin states are proposed to be built on the 8^- isomeric state based on their yrast feature and systematics of neighboring nuclei. Angular correlations are measured for the 640.2 $\rightarrow$ 952.4-keV cascade in ^{134}I to determine the spin-parities of the states of interest. Shell-model calculations based on our level scheme were performed and good agreement is found for both level energies and spin-parity assignments.

The high-spin structure of the neutron-rich nucleus ^{139}Cs is investigated. The yrast levels identified by Nowak *et al.* are confirmed and extended up to 4670 keV, with ten new levels and eighteen new deexciting transitions observed. Spins and parities of levels in ^{139}Cs are firmly assigned up to $25/2^+$ experimentally. The mixing ratio of the $9/2^+ \rightarrow 7/2^+$, 595.4-keV transition in ^{139}Cs is measured. High-spin states in the $N = 84$ isotone ^{137}I are also studied with three new excited levels and four new deexciting transitions added on the top of the previously known level scheme. The mixing ratio of the $9/2^+ \rightarrow 7/2^+$, 554.4-keV transition in ^{137}I is measured as well.

Realistic shell-model calculations are carried out to interpret the structures of ^{137}I and ^{139}Cs, by choosing ^{132}Sn as a closed core with the valence protons occupying the five levels $0g_{7/2}$, $1d_{5/2}$, $1d_{3/2}$, $1s_{1/2}$, and $0h_{11/2}$ of the $50 - 82$ shell, and the two valence neutrons occupying the six levels $0h_{9/2}$, $1f_{7/2}$, $1f_{5/2}$, $2p_{3/2}$, $2p_{1/2}$, and $0i_{13/2}$

of the $82 - 126$ shell. We have compared the states observed in ^{137}I and ^{139}Cs with those predicted by the calculations. It turns out that the calculations provide a very satisfactory description for both isotones, with discrepancies not exceeding 150 keV for most of the states up to 3.5 MeV. This shows that the interpretation of the low- to medium-energy spectra of these nuclei is well within the shell-model framework. The mixing ratio values of the 554.4-keV transition in ^{137}I and the 595.4-keV transition in ^{139}Cs are well reproduced. However, for levels higher than $33/2^{+}$ in both ^{137}I and ^{139}Cs, larger discrepancies between theory and experiment are found, which may indicate that excitations outside the chosen model space play an important role for such states in these two isotones. The present work has provided further evidence for the similarity of the spectroscopy of the $N = 84$ isotones, whose structures can be described in the shell-model framework.

Along with the previous work on ^{137,138}Cs [13] and ^{134}Te, ^{135}I [14], our experimental data show the power of the shell model to predict the level structures of neutron-rich nuclei with several nucleons outside the doubly-magic core ^{132}Sn $(Z = 50, N = 82)$. The current work indicates that the shell model can be used for neutron-rich nuclei as far as $Z = 55$ and $N = 84$, which is of great significance for both experiment and theory.

CHAPTER VI

g-FACTOR AND SPIN-PARITY ASSIGNMENTS OF EXCITED STATES IN $N = 83$ ISOTONES ^{135}Te, ^{136}I, ^{137}Xe, AND ^{138}Cs

6.1 Introduction

As noted in Chapter V, the study of nuclei with several valence nucleons beyond the doubly-magic core ^{132}Sn ($Z = 50, N = 82$) is a subject of special interest. In particular, the magnetic moments of such nuclei provide direct insight into the single particle structure of the orbitals outside the major shells. The g-factor is also sensitive to the two-body interactions of the valence nucleons and their interactions with the core. Therefore, measurements of g-factors of excited states in isotopes near the doubly-magic ^{132}Sn core help us to understand the nuclear shell structure in this region. Moreover, spin-parity assignments of excited states in such nuclei provide important tests of shell-model calculations. A new technique was developed to measure the g-factors of some states of interest in ^{134}Te and ^{135}I [14], and neutron-rich Xe, Ba, and Ce isotopes [33]. Some details of this method can be found in Subsection 3.4.3 and more information in Refs. [8, 30, 31]. The previously unknown g-factor of the $15/2^-$ state in ^{137}Xe is measured by using this technique. The experimental g-factor is reproduced very well by shell-model calculations with a two-body effective interaction derived from the CD-Bonn nucleon-nucleon potential. In addition, the measured angular correlation coefficients are used to assign and confirm spins and parities of several levels in four $N = 83$ isotones, ^{135}Te, ^{136}I, ^{137}Xe, and ^{138}Cs, which are also supported by shell-model calculations reported here.

6.2 Experimental results

The methods mentioned in Subsection 3.4.3 have been used to perform angular correlation studies for these four $N = 83$ isotones, ^{135}Te, ^{136}I, ^{137}Xe, and ^{138}Cs, and to measure the g-factor of the $15/2^-$ state in ^{137}Xe. The experimental results are reported as follows.

Figure 6.1 shows the partial level schemes of ^{135}Te, ^{136}I, ^{137}Xe, and ^{138}Cs. The spins and parities assigned to some of the states are determined by the measured angular correlations. The details of the assignments for levels and the measurement of the g-factor of the $15/2^-$ state in ^{137}Xe will be discussed below. The results of the angular correlations are summarized in Table VI.1.

For ^{135}Te, the measured A_2 and A_4 for the 325.0 $\rightarrow$ 1180.3-keV cascade are 0.097(6) and 0.007(9), respectively, which are obtained from the angular correlation shown in Fig. 6.2. The A_2 and A_4 here are consistent with the theoretical values 0.102 and 0.009 for a pure quadrupole $\rightarrow$ quadrupole cascade. Because of the yrast feature and high-spin character of the 1180.3- and 1505.3-keV levels, these two transitions are of $E2$ character. Therefore, with the known spin-parity of the ground state as $7/2^-$, the spins and parities of the 1180.3- and 1505.3-keV levels are assigned as $11/2^-$ and $15/2^-$, respectively, which agrees with the previous shell-model predictions [54, 126, 127].

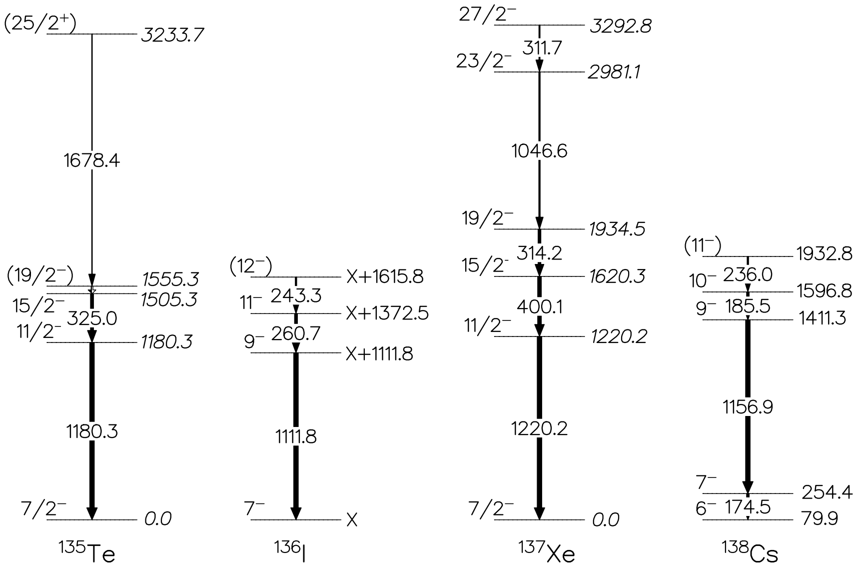

Figure 6.1: Partial level schemes of ^{135}Te, ^{136}I, ^{137}Xe, and ^{138}Cs with spins and parities assigned in this work. Data are taken from Refs. [13, 54, 101, 107, 126, 128] and the present work.

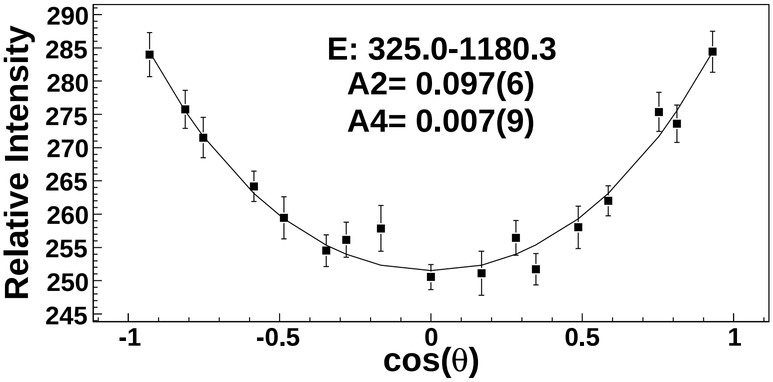

Figure 6.2: Angular correlation for the 325.0 → 1180.3-keV cascade in ^{135}Te.

Table VI.1: Angular correlations measured in ^{135}Te, ^{136}I, ^{137}Xe, and ^{138}Cs. A_2^{theory} and A_4^{theory} for a pure quadrupole → quadrupole and pure dipole → quadrupole cascades are indicated. The additional gates used for better selectivity are listed.

Nucleus	Cascade (keV)	Spin sequence	A_2^{exp}, A_4^{exp}	A_2^{theory}, A_4^{theory}	Additional gates (keV)
^{135}Te	325.0 → 1180.3	$15/2^- \to 11/2^- \to 7/2^-$	0.097(6), 0.007(9)	0.102, 0.009	None
^{136}I	260.7 → 1111.8	$11^- \to 9^- \to 7^-$	0.101(6), 0.009(10)	0.102, 0.009	None
^{137}Xe	400.1 → 1220.2	$15/2^- \to 11/2^- \to 7/2^-$	0.103(5), 0.012(8)	0.102, 0.009	314.2, 1046.6, 311.7, 1091.5, 240.8, 422.3, 150.4, 236.6
	314.2 → 400.1	$19/2^- \to 15/2^- \to 11/2^-$	0.072(7), 0.014(10)	0.102, 0.009	None
	311.7 → 1046.6	$27/2^- \to 23/2^- \to 19/2^-$	0.091(13), 0.009(19)	0.102, 0.009	1200.2, 400.1, 314.2, 1091.5, 304.9, 240.8, 150.4, 236.6
^{138}Cs	185.5 → 1156.9	$10^- \to 9^- \to 7^-$	-0.076(23), -0.007(34)	-0.071, 0.0	174.5, 236.0, 84.7, 895.5, 137.3, 222.0

For ^{136}I, the measured A_2 and A_4 for the 260.7 $\rightarrow$ 1111.8-keV cascade are 0.101(6) and 0.009(10), respectively, which are obtained from the angular correlation shown in Fig. 6.3. The A_2 and A_4 values here are consistent with the theoretical ones of $A_2 = 0.102$ and $A_4 = 0.009$ for a pure quadrupole $\rightarrow$ quadrupole cascade. Because the high-spin states in ^{136}I were proposed to be built on the 7^- isomeric state [54,101], 9^- and 11^- are assigned to the $(X + 1111.8)$- and $(X + 1372.5)$-keV levels, respectively, which confirms the previous calculated results in the shell-model framework [54,127].

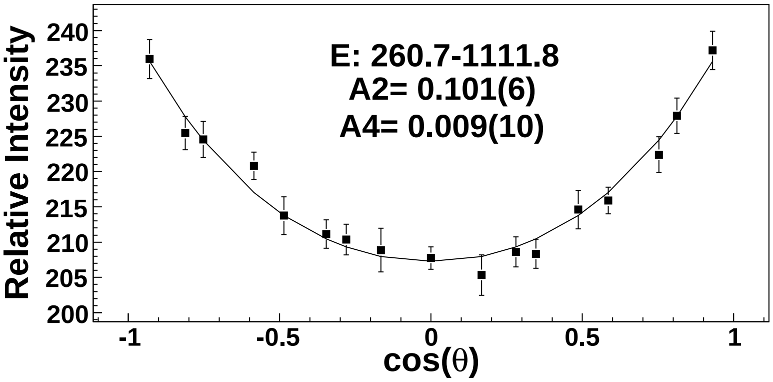

Figure 6.3: Angular correlation for the 260.7 $\rightarrow$ 1111.8-keV cascade in ^{136}I.

For ^{137}Xe, the measured A_2 and A_4 for the 400.1 $\rightarrow$ 1220.2-keV cascade are 0.103(5) and 0.012(8), respectively, which are obtained from the angular correlation shown in Fig. 6.4. These values are consistent with $A_2^{\text{theory}} = 0.102$ and $A_4^{\text{theory}} = 0.009$ for a pure quadrupole $\rightarrow$ quadrupole cascade, which indicates the $15/2^- \rightarrow 11/2^- \rightarrow 7/2^-$ cascade is unattenuated.

However, an attenuation seems to occur in the angular correlation of the 314.2 $\rightarrow$

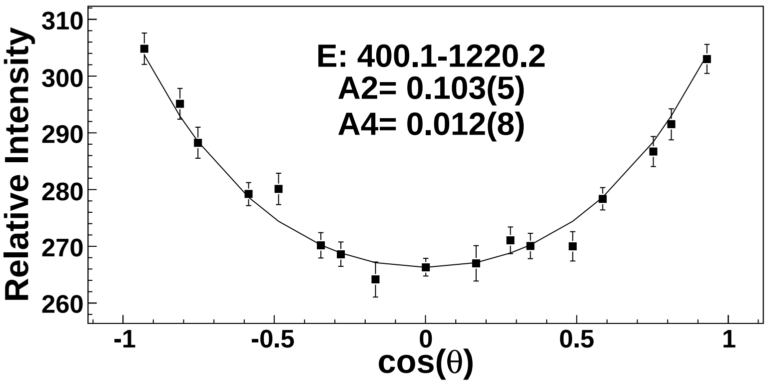

Figure 6.4: Angular correlation for the 400.1 → 1220.2-keV cascade in ^{137}Xe.

400.1-keV cascade in ^{137}Xe, as presented in Fig. 6.5, because the spin-parity sequence of $19/2^- \rightarrow 15/2^- \rightarrow 11/2^-$ was firmly assigned to this cascade in experiment [128] and theory [127] and the multipolarities of these two transitions were determined as $E2$ [128]. To extract the g-factor from the attenuation, the hyperfine field acting on the nucleus and the lifetime of the state must be known. The comprehensive hyperfine field compilation in Ref. [35] provides a wide range of fields for Xe in the iron host for samples with different preparation methods and at different temperatures. As was discussed in one previous paper [33], we adopt the $B_{\mathrm{HF}}(\mathrm{Xe})$ value as 73(8) T given in Ref. [35]. The g-factors in heavier Xe isotopes extracted by using $B_{\mathrm{HF}}(\mathrm{Xe}) = 73(8)$ T were predicted by IBM-2 very well in Ref. [33]. There is no measured value of the lifetime of the $15/2^-$ level. As in the report for the g-factor of the $15/2^+$ state in ^{135}I [14], shell-model calculations are used to obtain the lifetime of the $15/2^-$ state in ^{137}Xe. The lifetime of the $15/2^-$ state is calculated to be 0.6 ns. The details of the calculations will be presented in the following section. Thus, with the measured attenuation factor $G_2 = 0.71(7)$, the absolute value of the g-factor of the $15/2^-$ state in ^{137}Xe is obtained as 0.26(5), by using Eqs. (3.5) and (3.7).

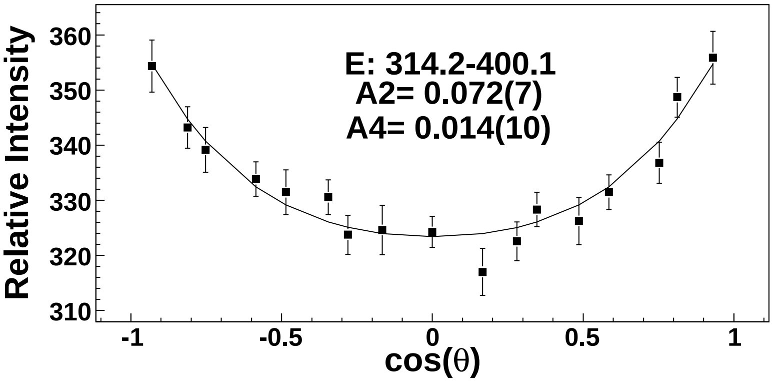

Figure 6.5: Angular correlation for the 314.2 → 400.1-keV cascade in ^{137}Xe. An attenuation is observed.

For the spin-parity assignment of the 2981.1-keV level in ^{137}Xe, one can use the correlation of the 1046.6 → 314.2-keV cascade because the multipolarity of the 314.2-keV transition is known to be $E2$ [128]. However, the 1934.5-keV, $19/2^-$ level has a lifetime of 11.7(6) ns [129], which makes the angular correlation of the 1046.6 → 314.2-keV cascade heavily attenuated. Then we choose the 311.7 → 1046.6-keV cascade and measure the correlation between these two transitions to determine the multipolarity of the 1046.6-keV transition, since the 311.7-keV transition is known to have an $E2$ character from linear polarization measurements [128]. The correlation shown in Fig. 6.6 gives the A_2 and A_4 values as 0.091(13), 0.009(19). These values are in good agreement with theory for a pure quadrupole → quadrupole cascade. On the basis of the $E2$ character for the 311.7-keV transition and the yrast character for the 2981.1-keV level, we conclude that the 1046.6-keV transition is of $E2$ character.

Thus, $23/2^-$ is assigned to the 2981.1-keV level, populating the $19/2^-$ level of energy 1934.5-keV. We are also able to assign $27/2^-$ to the 3292.8-keV level according to the above discussion. The assignments of $23/2^-$ to the 2981.1-keV and $27/2^-$ to the 3292.8-keV levels are consistent with the tentative experimental results [128], as well as the theoretical predictions [127].

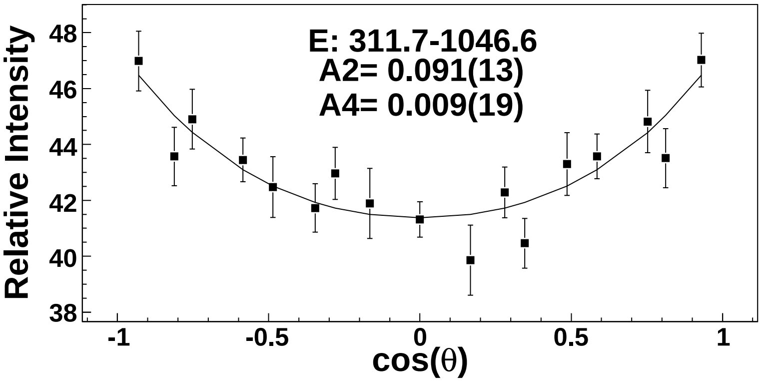

Figure 6.6: Angular correlation for the 311.7 → 1046.6-keV cascade in ^{137}Xe.

For ^{138}Cs, Li *et al.* [13] measured the angular correlation for the 1156.9 → 174.5-keV cascade by using the same method as in the present work to be $A_2 = -0.07(1)$ and $A_4 = -0.02(2)$. These results are consistent with the theoretical A_2 and A_4 values for a pure quadrupole → dipole ($9^- \to 7^- \to 6^-$) cascade as predicted by shell-model calculations [13]. However, the angular correlation results can not exclude some quadrupole mixing in the $7^- \to 6^-$ transition. Here, the correlation of the 185.5 → 1156.9-keV cascade is obtained as $A_2 = -0.076(23)$ and $A_4 = -0.007(34)$ in Fig. 6.7. With the known multipolarity of the 1156.9-keV transition as $E2$, the multipolarity of the 185.5-keV transition is assigned as mainly $M1$, since this result agrees very well with shell-model calculations in Refs. [13, 107] and the present calculations which predict the spin-parity of the 1596.8-keV level to be 10^-. An $E1$ assignment is not excluded experimentally, but it disagrees with the theory.

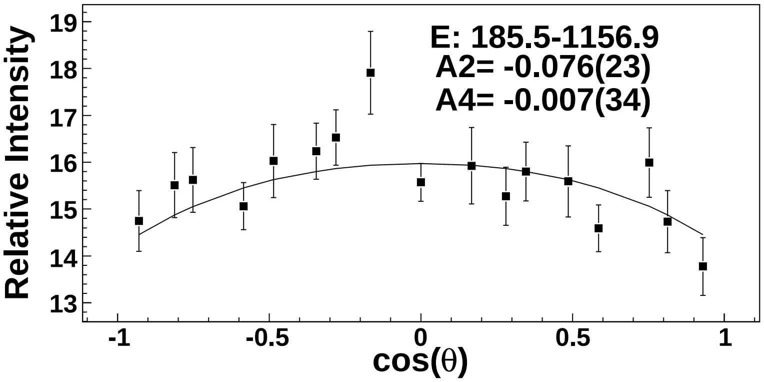

Figure 6.7: Angular correlation for the 185.5 → 1156.9-keV cascade in ^{138}Cs.

6.3 Shell-model interpretations

In this section we shall give a shell-model interpretation of the level schemes of the $N = 83$ isotones. The levels of ^{135}Te, ^{136}I, ^{137}Xe, and ^{138}Cs shown in Fig. 6.1 will be discussed, focusing attention on changes in the wave functions induced by the valence neutron beyond $N = 82$ as well as by the increase in the number of protons. To investigate this issue, we also discuss the level schemes of the corresponding $N = 82$ isotopes.

As in previous calculations, the valence neutron is assumed to occupy the six levels

$1f_{7/2}$, $2p_{3/2}$, $0h_{9/2}$, $2p_{1/2}$, $1f_{5/2}$, and $0i_{13/2}$ of the $82-126$ shell, while for protons the model space includes the five levels $0g_{7/2}$, $1d_{5/2}$, $1d_{3/2}$, $2s_{1/2}$, and $0h_{11/2}$ of the $50-82$ shell.

The Hamiltonian, which is the same as that of the previous shell-model studies on ^{132}Sn neighbors by the Napoli group [117,120,130,131], contains a two-body effective interaction derived from the CD-Bonn nucleon-nucleon potential [132]. The strong short-range repulsion of the latter is renormalized by constructing a smooth low-momentum potential $V_{\text{low}-k}$ [133], that is used directly as input for the calculation of the effective interaction within the framework of the $\hat{Q}$-box folded-diagram expansion [116]. Details on the derivation of the two-body effective interaction, as well as on the adopted single-proton and -neutron energies, can be found in Refs. [120] and [117], respectively. The shell-model calculations have been performed using the OXBASH computer code [134].

The experimental and calculated levels of ^{135}Te and ^{137}Xe are compared in Fig. 6.8, where we also report their "parent" states in ^{134}Te and ^{136}Xe. With respect to the levels in Fig. 6.1, we have added the second $19/2^-$ state in ^{135}Te and the second $19/2^-$ and $23/2^-$ states in ^{137}Xe [126,128].

We start discussion by noting the close correspondence between the level structures of ^{134}Te and ^{135}Te. Basically, from the current calculations it turns out that the states of ^{135}Te result essentially from the maximum spin alignment of a $1f_{7/2}$ neutron with the 0^+, 2^+, 4^+, 6_1^+, 6_2^+, and 9^- states of ^{134}Te, which are all dominated by a single configuration. More precisely, the lowest four states of ^{134}Te arise from the $\pi(0g_{7/2})^2$ configuration while the 6_2^+ and 9^- states from the $\pi 0g_{7/2}1d_{5/2}$ and

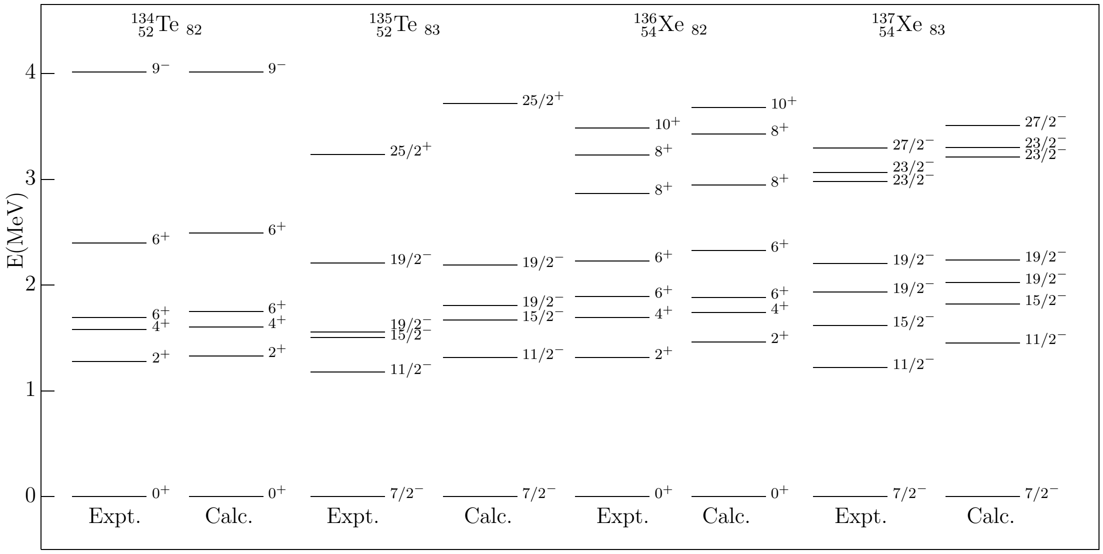

Figure 6.8: Experimental and theoretical levels in ^{134}Te, ^{135}Te, ^{136}Xe, and ^{137}Xe. Data are taken from Refs. [53, 54, 126, 128, 135] and the present work.

$\pi 0g_{7/2}0h_{11/2}$ configurations, respectively. The different nature of the two 6^+ states is confirmed by the different values of the measured half-lives [66], 164.1(9) ns for the first and an upper limit of 16 ps for the second. The calculated values, 185 ns and 2 ps, are in good agreement with experiment. As for the $19/2^-$ states in ^{135}Te, which are found to preserve the proton structure of the two 6^+ states, only the half-life of the lowest one has been measured [66] and its value is 0.511(20) μs, rather close to that of the first 6^+ state. The calculated half-life, 0.595 μs, compares well with the experimental one. For the second $19/2^-$ state, a value on the order of a picosecond is predicted, which is consistent with the half-life of the second 6^+ state. The $E2$ transition rates have been calculated using effective proton and neutron charges of $1.55e$ and $0.7e$ [119], while the $M1$ transition rates with an effective $M1$ operator which accounts for core-polarization effects [119]. The γ-ray energies are taken from experiment.

It is worth mentioning that the presence of an additional neutron in ^{135}Te favors configuration mixing. The wave functions of the states in ^{134}Te are found to have a percentage of dominant configuration ranging from 80 to 100% while these limits decrease to 74 and 82% for ^{135}Te. As regards the agreement between the experimental and calculated excitation energies, we find that the energies of ^{134}Te are very well reproduced, while for ^{135}Te a slightly expanded spectrum is predicted with a somewhat larger discrepancy for the $25/2^+$ state.

^{136}Xe and ^{137}Xe have an additional pair of protons with respect to the Te isotopes discussed above. This is reflected in ^{136}Xe by the presence of seniority-four states just above the second 6^+ state. These 8^+_1, 8^+_2, and 10^+ states arise mainly from the $\pi(0g_{7/2})^4$, $\pi(0g_{7/2})^3 1d_{5/2}$, and $\pi(0g_{7/2})^2(1d_{5/2})^2$ configurations, respectively, with a percentage of minor components less than 9%. The structures of the lowest five states in ^{136}Xe are quite similar to those of the corresponding states in ^{134}Te, with two additional protons in the $0g_{7/2}$ level. However, the wave functions of the ^{136}Xe states have a larger configuration mixing, where the percentage of the dominant component ranges from 55 to 79%.

As the case for ^{135}Te, each level of ^{137}Xe in Fig. 6.8 results from the maximum spin alignment of a $1f_{7/2}$ neutron and a ^{136}Xe state, although here configuration mixing plays a more prominent role. This is particularly true for the two $19/2^-$ and the two $23/2^-$ states. As an example, the calculated wave functions of the two $19/2^-$ states together with those of the two 6^+ states in ^{136}Xe are reported in Table VI.2. One sees that neither of the two states in ^{137}Xe preserves the simple proton structure of the 6^+ states but they both are strongly mixed. The measured half-lives are consistent with these findings. The value measured for the first $19/2^-$ state, 8.1(4) ns [129], is indeed different from the half-lives of the first and second 6^+ states, which are 2.95(9) μs and ≤ 50 ps, respectively. No experimental value is available for the second $19/2^-$ state. It is worth mentioning that the present calculated half-lives for the 6^+ states in ^{136}Xe states are 1 μs and 13 ps, in agreement with experiment, while the value for the first $19/2^-$ is one order of magnitude larger than experiment. However, assuming that the predicted ordering of the two $19/2^-$ states is not right, the second calculated state would correspond to the first observed one with a calculated half-life of 7 ns, which is quite close to the experimental value.

Table VI.2: Wave functions of the two 6^+ states in ^{136}Xe and the two $19/2^-$ states in ^{137}Xe (components with a percentage smaller than 10% are omitted).

Nucleus	I^π	Configuration	Probability
^{136}Xe	6_1^+	$\pi(0g_{7/2})^4$	77
	6_2^+	$\pi(0g_{7/2})^3 1d_{5/2}$	79
^{137}Xe	$(\frac{19}{2}^-)_1$	$\pi(0g_{7/2})^4 \nu 1f_{7/2}$	30
		$\pi(0g_{7/2})^3 1d_{5/2} \nu 1f_{7/2}$	44
	$(\frac{19}{2}^-)_2$	$\pi(0g_{7/2})^4 \nu 1f_{7/2}$	38
		$\pi(0g_{7/2})^3 1d_{5/2} \nu 1f_{7/2}$	36

The calculated value of the g-factor for the $15/2^-$ state in ^{137}Xe, which has been measured for the first time in the present experiment is +0.31, which agrees very well with the measured value $|g| = 0.26(5)$.

In Fig. 6.9, the calculated and experimental levels of ^{136}I and ^{138}Cs are shown, together with those of the two corresponding $N = 82$ isotones. Note that for ^{136}I and

^{138}Cs, the spectra are not relative to the ground states but to the 7^- and 6^- isomeric states, respectively. It should be mentioned that some of the theoretical results for ^{136}I have been discussed in a recent paper [136] by the Napoli group.

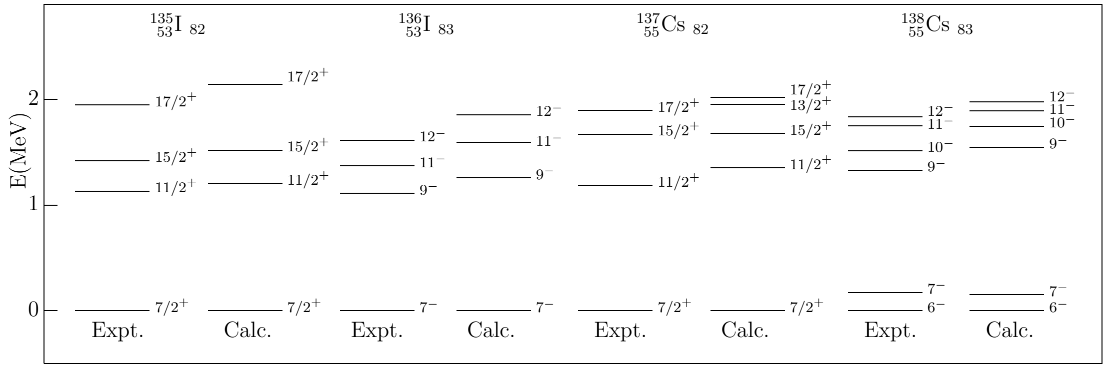

Figure 6.9: Experimental and theoretical levels in ^{135,136}I and ^{137,138}Cs. Data are taken from Refs. [13, 53, 54, 101, 107, 135] and the present work.

It turns out that the 7^-, 9^-, and 11^- states of ^{136}I are dominated by the $\pi(0g_{7/2})^3\nu 1f_{7/2}$ configuration with a percentage from 71 to 81%, while the 12^- state arises (99%) from the $\pi(0g_{7/2})^2 1d_{5/2}\nu 1f_{7/2}$ configuration. They all have the maximum I resulting from the coupling of a $1f_{7/2}$ neutron to the $7/2^+$, $11/2^+$, $15/2^+$, and $17/2^+$ states of ^{135}I.

As for ^{137,138}Cs, they have been the subject of the previous study in Ref. [13], where high-spin level energies were measured and compared with results of a shell-model calculation using the same Hamiltonian as in the present work. As shown in Fig. 6.9, the 12^- yrast state in ^{138}Cs has been located [13] at about 100 keV above the 11^- one, and the calculated energy is in very good agreement with the experimental value. The 11^- state decays to the 10^- state, which arises from the maximum spin alignment of a $1f_{7/2}$ neutron and the yrast $13/2^+$ state in ^{137}Cs. The latter, which is still missing in the experimental spectrum, is predicted at 1.95 MeV excitation energy with a wave function composed mainly of the $\pi(0g_{7/2})^4 1d_{5/2}$ configuration. It is worth mentioning that a 10^- state, which does not have an experimental counterpart, is predicted in ^{136}I, just a few tens of keV above the 11^- state. The probability of the $E2$ transition $12^- \rightarrow 10^-$ is calculated to have a value which is more than two orders of magnitude smaller than that of the $E2/M1$ transition $12^- \rightarrow 11^-$.

Finally, one sees that the two cascades in ^{136}I and ^{138}Cs end in two different isomeric states. For ^{136}I the position of the 6^- state is unknown and that of the 7^- state with respect to the ground state is still controversial [101, 137]. The non observation of the 6^- state in the present experiment may imply that it lies either above the 7^- state or very close to it. The present calculations support the second alternative because the 6^- state has been predicted at 30 keV below the 7^- one, while 30 keV is the detection energy cut-off in the present experiment.

6.4 Conclusion

The knowledge of g-factors in isotopes with several nucleons outside the doubly-magic core ^{132}Sn is extended with the first measurement of the g-factor of the $15/2^-$ state in ^{137}Xe. Our result is in good agreement with shell-model calculations. Based on observed angular correlations, spins and parities are assigned to several levels in the $N = 83$ isotones ^{135}Te, ^{136}I, ^{137}Xe, and ^{138}Cs. These assignments are in agreement with the previous experimental results and shell-model predictions. The present shell-model calculations also show configuration mixing in these nuclei caused by one more neutron than their corresponding $N = 82$ isotopes and the increasing proton numbers.

CHAPTER VII

EVIDENCE FOR OCTUPOLE CORRELATIONS IN ^{140,142}Cs

7.1 Introduction

Neutron-rich Cs ($Z = 55$) isotopes with mass numbers from 137 to 145 have five protons beyond the 50 proton major shell and the neutron number is located between the 82 and 126 neutron closed shells. High-spin states in these nuclei have been studied from the spontaneous fission of ^{248}Cm [98,104,107,138], ^{252}Cf [13,60,61,139], and deep inelastic transfer reactions [106]. Nuclear shapes in these neutron-rich Cs isotopes are expected to change gradually from a spherical shape in ^{137,138,139}Cs [13, 98,106,107,139]to a weak deformed shape in ^{140,141,142}Cs [60,61,104,138] and then to a well deformed shape in ^{143,144,145}Cs [61,104,138]. Octupole correlations were observed in ^{141}Cs [60] and ^{143}Cs [104]. In this work, octupole correlations are extended to ^{140,142}Cs [108,109] from the analysis of ^{252}Cf spontaneous fission data.

The odd-odd isotopes ^{140}Cs$_{85}$ and ^{142}Cs$_{87}$ have three and five neutrons outside the $N = 82$ cloesd shell, respectively, and are close to the octupole deformation/correlation region centered around $Z = 56$, $N = 88$ [22,23,140–143]. Possible octupole deformations were proposed in the Cs isotopes at $N = 85 - 88$ in Ref. [144], based on the observation of inverted staggering of the odd-even effect in the differential radii in the Cs isotopes. Urban *et al.* reported the observation of octupole correlations in ^{143}Cs and tentative results in ^{141}Cs [104]. Recently our group proposed parity doublets in ^{141}Cs [60], with the simplex quantum numbers $s = +i$ and $s = -i$.

The β decay of ^{140}Xe [66] and fission of ^{252}Cf [61] have been used to populate excited states in ^{140}Cs. Many transitions at low excitation energy were observed in the β decay of ^{140}Xe [66]. A few high-spin levels were identified in ^{140}Cs in the spontaneous fission of ^{252}Cf by Hwang *et al.* [61]. In this work, we report a new level scheme for ^{140}Cs based on the results in Ref. [61]. We observe seven new transitions at low and moderate spin and thirteen at high spin. The new structure is proposed to be related to octupole correlations .

A high-spin level scheme of ^{142}Cs was reported in Ref. [61] involving six transitions of energies 97.3, 205.6, 404.7, 544.9, 699.9, and 787.0 keV out of the yrast band and seven other transitions. No nuclear structure was discussed further by the authors. By means of our new and higher-statistics data, a new level scheme for ^{142}Cs is proposed. Spin-parities are assigned to levels based on some angular correlation measurements and systematics of neighboring nuclei. The new level structure of ^{142}Cs shows evidence for the existence of octupole correlations.

In a reflection-asymmetric nuclear mean field, an electric dipole moment D_0 may occur as a difference of the interference terms between quadrupole Y_{20} and octupole Y_{30} shape vibrations for protons or neutrons. One expects to see significantly larger D_0 in nuclei with octupole correlations than those without octupole correlations. It is of interest to compare the D_0 values for the Cs isotopes with octupole correlations with those for other neighboring isotopes with octupole deformations/correlations. The D_0 values for ^{140,142}Cs are determined using the corresponding branching ratios from the same spin states. A dramatic decrease of D_0 with increasing neutron numbers in the Cs isotopic chain is found, as proposed in Ref. [60].

7.2 Experimental results

7.2.1 ^{140}Cs

The level scheme of ^{140}Cs proposed by Hwang *et al.* [61] was solely based on the observation of an 80.1-keV transition in the fission data, which has the same energy as the one found in the previous β-decay studies of ^{140}Xe to ^{140}Cs [66]. Here, a measurement is undertaken to firmly establish the mass number of the transitions proposed in Ref. [61], as reported in Subsection 5.3.1.

The level scheme of ^{140}Cs reported in Ref. [61] is extended and a side-band is proposed. The coincidence spectrum, created by double gating on the 80.1- and 563.6-keV transitions [61], is shown in Fig. 7.1. In addition to previously known transitions in Tc isotopes and ^{140}Cs, one clearly sees five new transitions of energies 35.5, 54.8, 90.3, 551.2, and 552.6 keV, the latter two forming a doublet. To further confirm the existence and positions of the above five new transitions, two spectra are obtained, as presented in Fig. 7.2, where the gate transitions are indicated. Figure 7.2 (a), gated on the known 594.3- and 640.9-keV transitions in ^{140}Cs, shows the coincidence relationship among known transitions in ^{107,108,109}Tc and ^{140}Cs, and the newly observed transitions, such as the 35.5-, 54.8-, and 90.3-keV transitions and two others of energies 472.5 and 702.2 keV. The spectrum, gated on the new 551.2-keV and known 563.6-keV transitions, is given in Fig.7.2 (b), where the new transitions of energies 35.5, 552.6, 652.6, and 876.5 keV are seen. Note that the new 54.8-keV transition seen in Fig.7.2 (a) is not found in Fig.7.2 (b). This observation is very important for us to place newly observed transitions in the level scheme of ^{140}Cs.

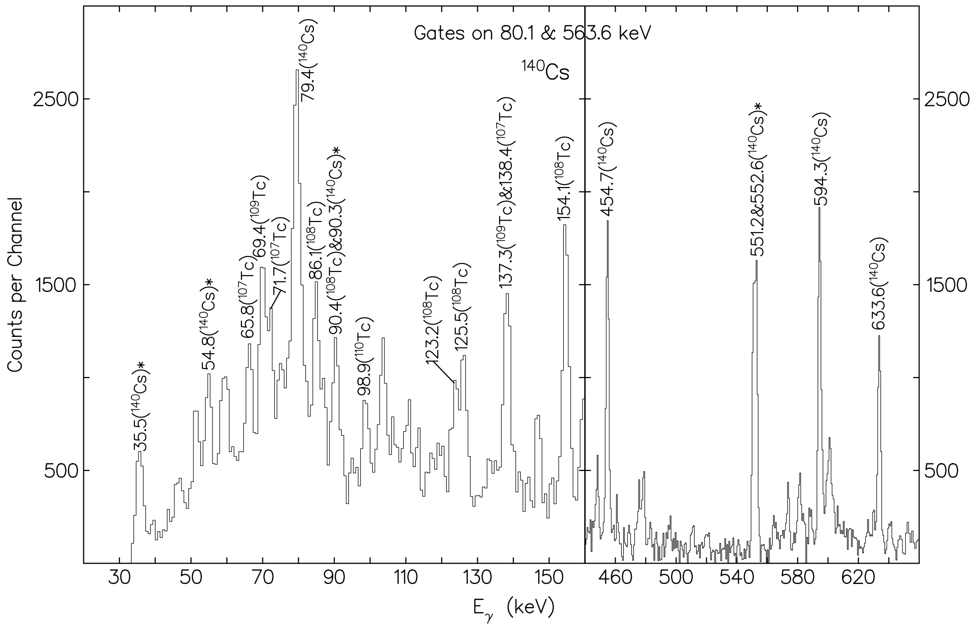

Figure 7.1: Coincidence spectrum double gated on the 80.1- and 563.6-keV transitions in ^{140}Cs [61]. The new transitions are marked with an asterisk.

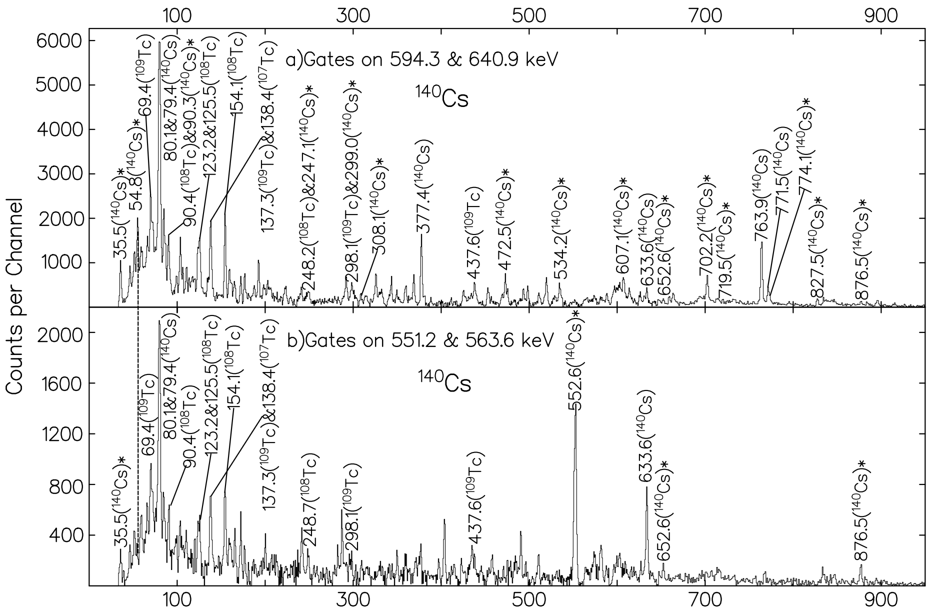

Figure 7.2: Coincidence spectra double gated on transitions in ^{140}Cs. The newly identified transitions are marked with an asterisk. A dashed line is drawn to illuminate the position of the 54.8-keV transition.

Careful cross-checking of numerous coincidence spectra leads to the final transition identifications and placements in the level scheme of ^{140}Cs. Eight new excited levels with thirteen new de-exciting transitions at high spin and three new excited levels with seven new deexciting transitions at low and moderate spin are observed. The level scheme of ^{140}Cs is presented in Fig. 7.3, where excited states are extended up to 3794 keV with a new side-band (band 3).

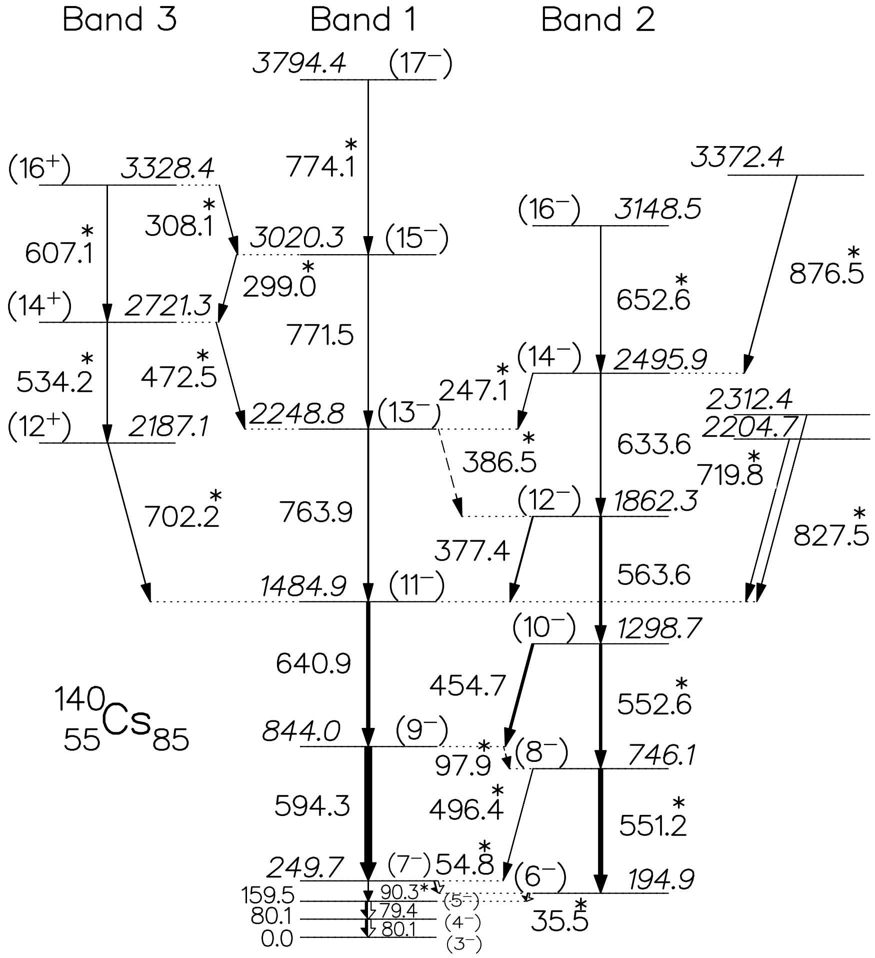

Figure 7.3: The new level scheme of ^{140}Cs. Energies are in keV and the width of the arrow is proportional to the corresponding γ-ray intensity. The newly observed transitions are marked with an asterisk. The level energies are relative to that of the (3^{-}) state.

Angular correlations are measured for some strong transitions in Fig. 7.3. The measured A_2 and A_4 values for the 640.9 → 594.3- and 454.7 → 594.3-keV cascades are shown in Figs. 7.4 and 7.5, respectively. These data are consistent with a $\Delta I = 2$ character of the 594.3- and 640.9-keV transitions and a $\Delta I = 1$ character of the 454.7-keV transition [3, 5], which allow us to assign spin-parities to levels relative to I^π of the 249.7-keV level, populated by the 594.3-keV transition.

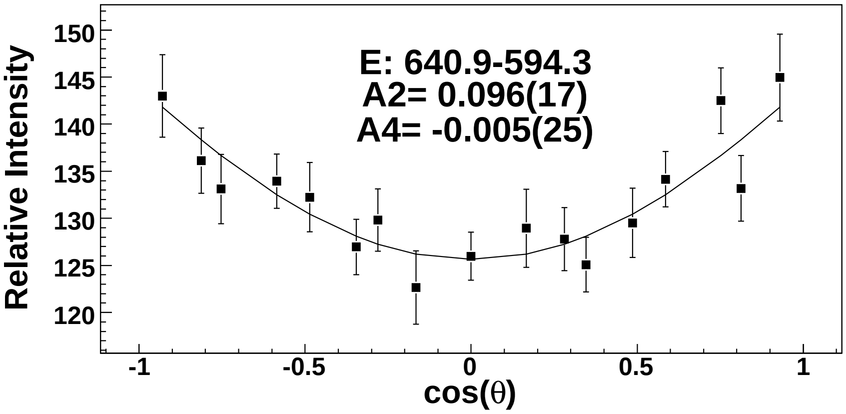

Figure 7.4: Angular correlation for the 640.9 → 594.3-keV cascade in ^{140}Cs.

It is assumed that spin values increase with increasing excitation energies, as commonly observed in fission products at high spin. We argue that the 594.3- and 640.9-keV transitions have a stretched $E2$ multipolarity and the 454.7-keV transition has an $E2/M1$ mixed multipolarity. Consequently, multipolarities of other upper crossover transitions above the 194.9-keV level in bands 1 and 2 are proposed to be stretched $E2$, whereas those of the linking transitions are $E2/M1$, by considering the multipolarity of the 54.8-keV transition as $E2/M1$. As will be discussed in Subsection

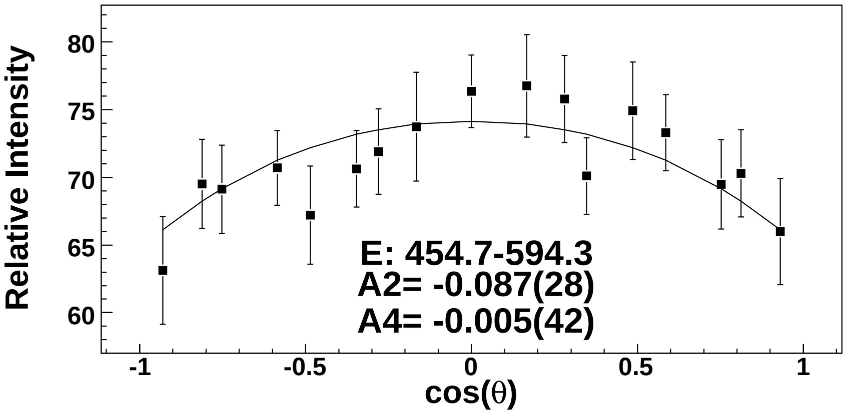

Figure 7.5: Angular correlation for the 454.7 → 594.3-keV cascade in ^{140}Cs.

7.3.1, the very probable I^{π} assignments for the 249.7- and 194.9-keV levels are 7^{-} and 6^{-}, respectively. So, spins and parities can be assigned to the levels above the 249.7-keV level, as present in Fig. 7.3, based on their multipolarites proposed above and the detailed systematics analysis below. Spins and parities are assigned to the levels in band 3, according to the proposal in Subsection 7.3.1 that band 3 along with band 1 forms an octupole $s = +1$ doublet.

7.2.2 ^{142}Cs

As argued in Chapter V on the nuclear structure of ^{139}Cs, a group of transitions previously assigned to ^{139}Cs by Hwang *et al.* [61] belong to ^{142}Cs. This assignment is based on the measurement that yields the fission yield ratio of ^{107}Tc [64] to ^{108}Tc [65] in the 218.6/408.6-keV [61] double gate, 0.49(7), consistent with the value of 0.47(7) for ^{142}Cs.

Careful examinations and back-ground subtractions of several coincidence spectra reveal that the peak observed around 97 keV in the 408.6/218.3-keV gate is 96.9 keV, not the same as the one of energy 97.3 keV observed in the 404.8/205.6-keV gate. The coincidence spectra double gated on the 218.3/96.9- and 205.6/97.3-keV transitions show the newly identified transitions, especially these of energies 269.5, 757.9, 299.1, 821.5, 744.4, 457.6, and 584.4 keV, as presented in Fig. 7.6. Two additional spectra are shown in Fig. 7.7 to provide more evidence for the new transitions. The observation of the 457.6-keV transition in Figs. 7.6 (a) and 7.7 (a) helps us to properly place the transitions previously assigned to ^{139}Cs in Ref. [61].

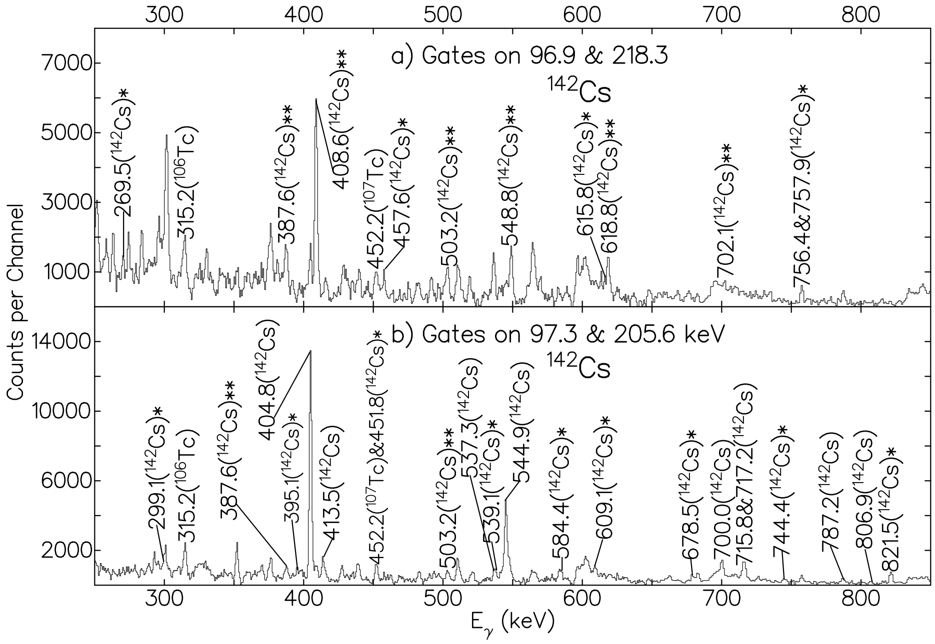

Figure 7.6: Coincidence spectra double gated on the 96.9/218.3- and 97.3/205.6-keV transitions in ^{142}Cs. The transitions marked with two asterisks are those previously assigned to ^{139}Cs in Ref. [61], but now to ^{142}Cs. The newly identified transitions are marked with an asterisk.

We learned of the work of Rząca-Urban *et al.* on the level scheme of ^{142}Cs [145], where two low-energy transitions of energies 25.3 and 26.4 keV were observed. How-

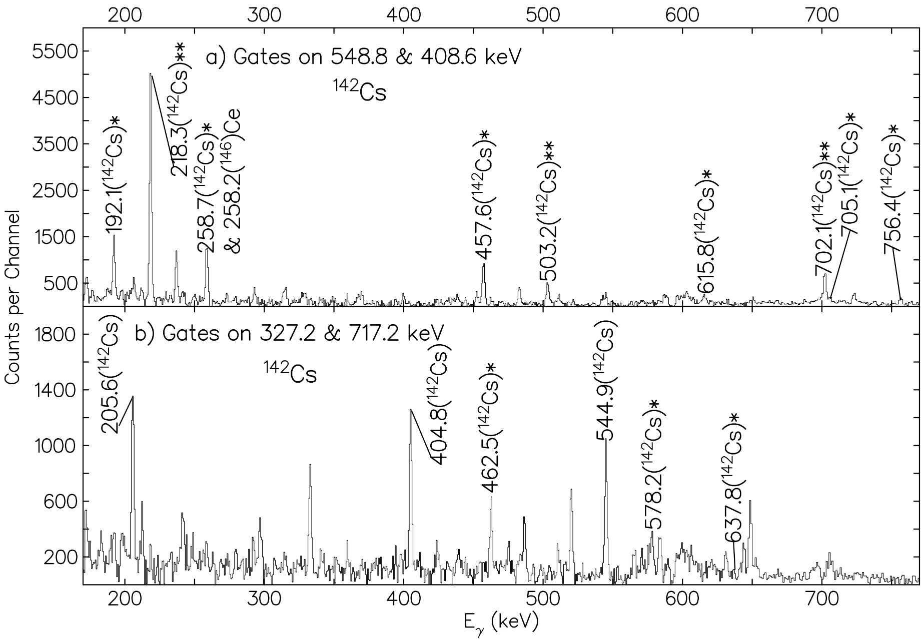

Figure 7.7: Coincidence spectra double gated on the 408.6/548.8- and 717.2/327.2-keV transitions provide evidence for the newly identified transitions marked with an asterisk. Contamination from the $2^+ \rightarrow 0^+$ transition of energy 258.2 keV in ^{146}Ce is indicated in (a) because the gate energy 408.6 keV is very close to the $4^+ \rightarrow 2^+$ transition of energy 409.6 keV in ^{146}Ce.

ever, we can confirm/not confirm these two transitions because they are well below our detection energy cut-off of 30 keV. Since they were identified in the spectrum measured with low-energy photon spectrometers (LEPSs) in Ref. [145] and the three transitions of energies 192.1, 395.1, and 539.1 keV interlacing bands 1 and 2 (see Fig. 7.8) are also seen in our data, as shown in Figs. 7.6 (b) and 7.7 (a), we accept the placements of the transitions at low spin as reported in Ref. [145]. With the reassignment of the transitions in ^{139}Cs in Ref. [61] to ^{142}Cs, the level scheme of ^{142}Cs is presented in Fig. 7.8, having thirty-seven new transitions more than those in Ref. [61] and seven new levels with seventeen new transitions more than those in Ref. [145].

The measured angular correlation coefficients for cascades in ^{142}Cs are summarized in Table VII.1, where the corresponding theoretical values [3, 5] are also listed. Note that no angular correlation including the 205.6-keV transition is measured because the 204.8-keV transition in ^{106}Tc (4n partner) [64], the 206.0- and 207.5-keV transitions in ^{107}Tc (3n partner) [64], and the 204.0-keV transition in ^{108}Tc (2n partner) [65] contribute to the 205.6-keV transition and contaminate it. This transition was proposed to have an $E2$ multipolarity in Ref. [145], which is adopted here. More details of the spin-parity assignments in ^{142}Cs will be given in Subsection 7.3.2.

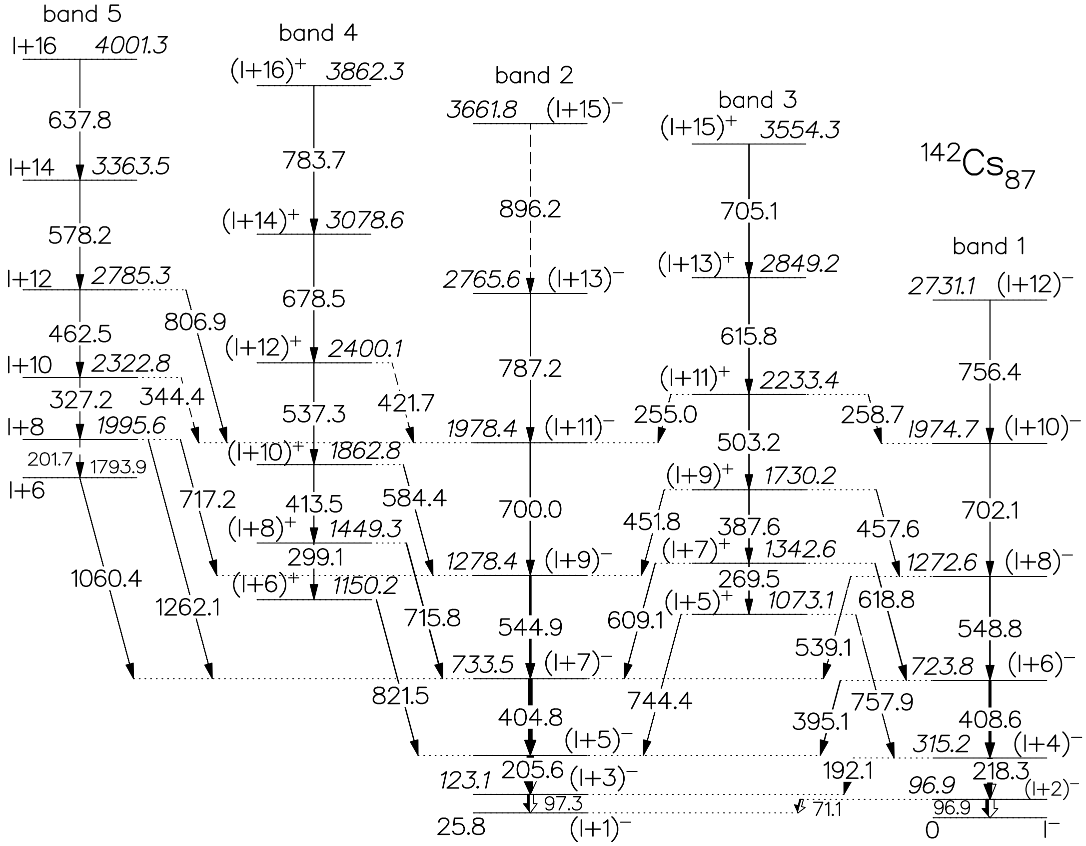

Figure 7.8: The new level scheme of ^{142}Cs. Energies are in keV. Two sets of parity doublets are observed. The unknown energy of the isomer is shown as zero. Its energy should be added to the level energies shown here when this energy is known.

Table VII.1: Angular correlations measured for cascades in ^{142}Cs. A_2^{theory} and A_4^{theory} for a pure quadrupole → quadrupole and pure dipole → quadrupole cascades are indicated. Multipolarities for the transitions are assigned.

Cascade (keV)	A_2^{exp}, A_4^{exp}	A_2^{theory}, A_4^{theory}	Multipolarity
218.3 → 96.9	0.11(2), -0.02(3)	0.102, 0	$E2 \rightarrow E2$
408.6 → 218.3	0.086(19), 0.032(29)	0.102, 0	$E2 \rightarrow E2$
548.8 → 408.6	0.093(25), -0.010(39)	0.102, 0	$E2 \rightarrow E2$
544.9 → 404.8	0.104(16), 0.001(24)	0.102, 0	$E2 \rightarrow E2$
715.8 → 404.8	-0.052(30), -0.003(45)	-0.071, 0	$E1 \rightarrow E2$
618.8 → 408.6	-0.078(38), -0.022(59)	-0.071, 0	$E1 \rightarrow E2$

7.3 Discussion

7.3.1 ^{140}Cs

The ground state of ^{140}Cs was reported to have a spin-parity of 1^- [66]. A configuration $\pi(1g_{7/2})^{-3}\nu(2f_{7/2})^3$ was assigned to the 1^- ground state [146]. Note that one can write the $g_{7/2}$ proton configuration as $\pi(1g_{7/2})^{-3}$ or $\pi(1g_{7/2})^5$. The neighboring odd-odd Cs isotopes, ^{136}Cs, ^{138}Cs and ^{142}Cs, have ground states of 5^-, 3^-, and 0^-, respectively [66]. The 5^- ground state of ^{136}Cs was reported to be a $\pi(1g_{7/2})^{-3}_{7/2}\nu(2d_{3/2})^{-1}$ configuration, which is formed by coupling the ground state of ^{135}Cs with the ground state of ^{135}Xe. An 8^- isomeric state in ^{136}Cs was observed with the $\pi(1g_{7/2})^{-3}_{7/2}\nu(1h_{11/2})^{-1}$ configuration [66], by coupling the ground state of ^{135}Cs with the $11/2^-$ isomer of ^{135}Xe. The 3^- ground state in ^{138}Cs was related to the configuration $\pi(1g_{7/2})^5\nu 2f_{7/2}$ [147]. An isomer of 6^- was identified in ^{138}Cs and interpreted to be either a $\pi(1g_{7/2})^5\nu 2f_{7/2}$ in Ref. [13] or $\pi(1g_{7/2})^4 2d_{5/2}\nu 2f_{7/2}$ dominating configuration in Ref. [107]. With a further addition of two neutrons to ^{140}Cs, the configuration $\pi(1g_{7/2})^{-3}\nu(2f_{7/2})^{-3}$ was proposed to form the main component in the nuclear wave function of the 0^- ground state in ^{142}Cs [146]. As regards to odd-odd $N = 85$ isotones, ^{136}Sb has a 1^- ground state and a (6^-) isomer, both of which are likely to be members of the $\pi 1g_{7/2}\nu(2f_{7/2})^3$ multiplet [148, 149]. For the ground state of ^{138}I, both 0^- and 1^- seem to be possible based on shell-model calculations but neither was observed experimentally [93]. A (3^-) isomer was proposed in Ref. [93] as a $[\pi 1g_{7/2}\nu 2f_{7/2}]_j$ member. The spins and parities of the ground states of ^{142}La and ^{144}Pr were reported to be 2^- and 0^-, respectively, from the β-decay studies [66]. The spin-parity of the ground state of ^{146}Pm was determined to be 3^- in the β-decay studies [150,151], without providing a configuration explanation. A (9^+) isomer at 872.9 keV in ^{146}Pm was accounted for by a configuration $\pi 1h_{11/2}\nu(2f_{7/2})^3_{7/2}$ in analogy with the corresponding levels in ^{148}Eu and ^{150}Tb [152]. The predominant configuration of the 5^- ground state of ^{148}Eu is $\pi(2d_{5/2})^{-1}\nu(2f_{7/2})^3_{7/2}$ [153], by coupling the ground state of ^{147}Eu to that of ^{147}Sm. An isomeric state was observed with a $\left[\pi 1h_{11/2}(2d_{5/2})^{-2}_0\nu(2f_{7/2})^3_{7/2}\right]_{9^+}$ configuration from the coupling of the $11/2^-$ isomer in ^{147}Eu with the ground state of ^{147}Sm [153,154]. On the basis of the above systematics, it is reasonable to interpret the 1^- ground state in ^{140}Cs as $\pi(1g_{7/2})^5_{7/2}\nu(2f_{7/2})^3_{3/2}$, by coupling the ground state of ^{139}Cs [139] to that of ^{139}Xe [155, 156].

High-spin states have been observed in odd-A, $N = 85$ isotones, such as ^{138}I, ^{146}Pm, and ^{148}Eu, in which high-spin levels are built on the (3^-), (9^+), and 9^+ isomers, respectively [93,152,154]. In the latter two nuclei, levels in the $13^+ \rightarrow 11^+ \rightarrow 9^+$ cascade are members of the $\pi 1h_{11/2}(2d_{5/2})^{-2}_0\nu(2f_{7/2})^3_{7/2,11/2,15/2}$ multiplet, whereas those in the $14^+ \rightarrow 12^+ \rightarrow 10^+$ cascade are members of the $\pi 1h_{11/2}(2d_{5/2})^{-2}_0\nu 1h_{9/2}(2f_{7/2})^2_{0,2,4}$ multiplet. These two cascades are connected by $\Delta I = 1$ linking transitions. It is worth mentioning that the 10^+ level decays to not only the 9^+ level but also to an 8^+ level, 8 keV above the 9^+ level, in ^{148}Eu, which is not seen in ^{146}Pm. However, the configuration of this 8^+ state was not clearly explained in Ref. [154]. It might be formed by coupling the $1h_{11/2}$ proton to the $(2f_{7/2})^3_{5/2}$ neutron. Also ^{138}I has two $\Delta I = 2$ cascades, $(11^-) \rightarrow (9^-) \rightarrow (7^-)$ and $(12^-) \rightarrow (10^-) \rightarrow (8^-)$, connected by $\Delta I = 1$ transitions [93]. All of these levels were interpreted as members of the $[\pi 1g_{7/2}\nu 2f_{7/2}]_j$ multiplet in Ref. [93]. It is also very interesting to observe a (6^-) level in ^{138}I, connected to the 8^-, 7^-, and 5^- levels by the 425.5-, 65.6-, and 68.2-keV transitions, respectively. The level at 194.9 keV in ^{140}Cs is quite similar to this 6^- level in ^{138}I, connected to the 746.1-, 249.7-, and 159.5-keV levels by the 551.2-, 54.8-, and 35.5-keV transitions, respectively, as shown in Fig. 7.3. This similarity may indicate that levels in bands 1 and 2 in ^{140}Cs have the same configuration, as proposed in ^{138}I. Since no isomer like the $11/2^-$ level in ^{145}Pm and ^{147}Eu has been identified in ^{139}Cs, we do not think either the 249.7- or 194.9-keV level is an isomeric state, different from the (9^+) and 9^+ states in ^{146}Pm and ^{148}Eu on which high-spin states are built, respectively. The same conclusion can be drawn in ^{138}I and is supported by Ref. [93], because one has not observed an isomeric state at high spin in ^{137}I either [139]. Therefore, we may argue that the 249.7-keV level has a $\pi(1g_{7/2})^5_{7/2}\nu(2f_{7/2})^3_{7/2}$configuration, which comes from the coupling of the $7/2^+$ ground state of ^{139}Cs [139] with the $7/2^+$ state of ^{139}Xe. This level, 22.8 keV above the $3/2^-$ ground state, is one member of the $\nu(2f_{7/2})^3_{3/2,5/2,7/2}$ multiplet, which is a common feature of the $N = 85$ even-odd nuclei. High-spin states in ^{139}Xe are built on this level [155, 156]. The systematics of even-odd and odd-odd $N = 85$ nuclei, presented in Fig. 7.9, supports such an argument. If one considers the maximum aligned coupling of the $7/2^+$ ground state of ^{139}Cs [139] with the $7/2^-$ state of ^{139}Xe, one will obtain a (7^-) spin-parity for the 249.7-keV level in ^{140}Cs, which is analogous to the $(X + 295)$-keV level in ^{138}I.

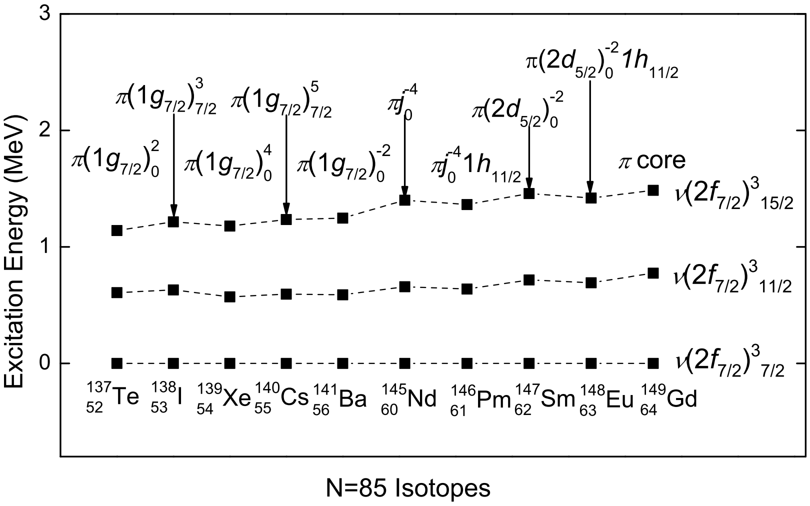

Figure 7.9: Comparison of $\nu(2f_{7/2})^3_{7/2}$ states in $N = 85$ isotones. Experimental energies are given relative to the lowest state drawn in the figure. Data of other nuclei are taken from Refs. [93, 152, 154–159].

However, the spin-parity of the 80.1-keV level known from the β-decay studies, either 1^- or 0^- [66], can not be derived with the assumption that the 54.8- and 35.5-keV transitions are of $\Delta I = 1$ character, unless the 79.4-keV transition is of $\Delta I = 4$ character. There may be three possible explanations for this discrepancy. First, the 54.8- and 35.5-keV transitions may be of $\Delta I = 2$ character, which makes the 194.9- and 159.5-keV levels of spins 5 and 3, respectively. Then a spin 1 might be assigned to the 80.1-keV level by assuming that the spin carried by the 79.4-keV transition is 2. However, $\Delta I = 2$ for the 54.8 transitions is not reasonable, as discussed above and below in detail. Second, the coupling of the $7/2^+$ ground state of ^{139}Cs [139] with the $7/2^+$ state of ^{139}Xe may be non-stretched, which gives a spin smaller than 7, like 5. With the spin assignments of 4 and 3 to the 194.6- and 159.5-keV levels, respectively, one could assign a spin 1 to the 80.1-keV level, with the 79.4-keV transition assumed to be of $\Delta I = 2$ character. The third is the most likely one that the observed 80.1-keV transition is not the one found in the β-decay studies [66]. That can be true because it is common in many other odd-odd isotopes where there is no overlap between the levels obtained in the spontaneous fission of ^{252}Cf and the β decay. If so, the 0-keV level is likely to be an isomer and have a (3^-) spin-parity. This is supported by comparing the level structure of ^{140}Cs with that of ^{138}I as discussed below in detail.

Based on the above argument, levels in band 1 in Fig. 7.3 built on the 249.7-keV, (7^-) level are likely to be members of the $\pi(1g_{7/2})^5_{7/2}\nu(2f_{7/2})^3_{7/2}$configuration. As was mentioned above, the 14^+, 12^+, and 10^+ states in ^{146}Pm and ^{148}Eu have a $\pi 1h_{11/2}(2d_{5/2})^{-2}_0\nu 1h_{9/2}(2f_{7/2})^2_{0,2,4}$ configuration, different from that of the 13^+ ,11^+, and 9^+ levels. This configuration is formed by coupling the $11/2^-$ isomer in the corresponding odd-even isotopes with the yrast $9/2^-$ state in the relevant even-odd isotones, where the $9/2^-$ state was supposed to be a $\nu 1h_{9/2}(2f_{7/2})^2_{0,2,4}$ configuration [158]. This configuration is obtained by promoting a $2f_{7/2}$ neutron to the $1h_{9/2}$ orbital, to interpret levels in the $21/2^- \rightarrow 17/2^- \rightarrow 13/2^- \rightarrow 9/2^-$ cascade in ^{145}Nd and ^{147}Sm, respectively [158]. However, the level pattern of band 2 in ^{140}Cs seems unlike that of the $14^+ \rightarrow 12^+ \rightarrow 10^+$ cascade in ^{146}Pm and ^{148}Eu. The 746.1-keV level populates the 249.7-keV level weakly; on the contrary, it feeds the lower 194.9-keV level strongly. The same structure is seen in ^{138}I, where a strong transition was identified between the (8^-) and (6^-) levels. Because levels in both the $(11^-) \rightarrow (9^-) \rightarrow (7^-)$ and $(12^-) \rightarrow (10^-) \rightarrow (8^-)$ cascades in ^{138}I have the same configuration, one may be favorable to the idea that levels in both bands 1 and 2 above the (7^-) level are members of the $\pi(1g_{7/2})^5_{7/2}\nu(2f_{7/2})^3_{7/2}$ configuration, though the $\nu 1h_{9/2}(2f_{7/2})^2_{0,2,4}$ configuration was also proposed to interpret levels in the $21/2^- \rightarrow 17/2^- \rightarrow 13/2^- \rightarrow 9/2^-$ cascade in ^{139}Xe [155, 156], a neighboring $Z = 54$ isotone of ^{140}Cs. As will be discussed below, rotational and vibrational motions are observed in ^{140}Cs. So, bands 1 and 2 are the signature partners in ^{140}Cs.

Let us compare the level patterns of ^{138}I and ^{140}Cs, in more detail. Figure 7.10 shows level energies in ^{138}I and ^{140}Cs, which are relative to the X-keV state in the former and the 0-keV state in the latter. Their striking similarity supports the above arguments and also indicate that the 0-keV level in ^{140}Cs is not the ground state with $I^\pi = 1^-$ but is likely to be an isomeric state with $I^\pi = 3^-$ in analogy to the (3^-), X-keV state in ^{138}I. The lowest 80.1-keV transition observed in ^{140}Cs is likely to be an $E2/M1$ transition as the 118.3-keV transition in ^{138}I. The spin-parity assignments for high-spin levels in bands 1 and 2 in ^{140}Cs in the above discussion are well born out by Fig. 7.11, where only high-spin levels above the 7^- level in ^{138}I and ^{140}Cs are compared. One sees that the level pattern in bands 1 and 2 in ^{140}Cs bears a remarkable resemblance to that in ^{138}I. So, it is reasonable to assign (7^-) to the 249.7-keV level and a $\pi(1g_{7/2})^5_{7/2}\nu(2f_{7/2})^3_{7/2}$configuration to levels in bands 1 and 2 in ^{140}Cs. The similarity in the level patterns of two $N = 83$ isotones, ^{136}I and ^{138}Cs [107], support the above argument as well. Of course, care should be taken in giving pure configuration assignments to nuclei located in a transitional region between the spherical and deformed nuclear shapes, especially to those odd-odd isotopes.

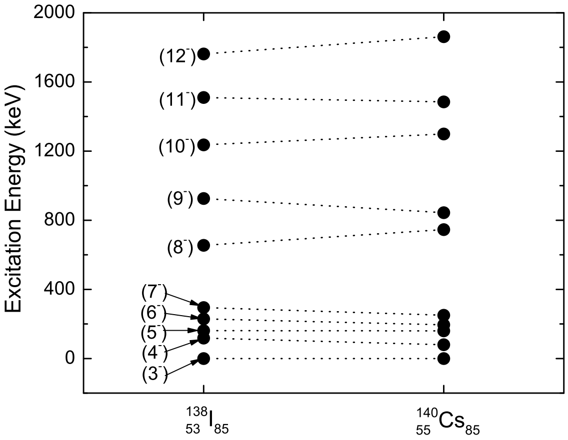

Figure 7.10: Comparison of bands 1 and 2 in ^{140}Cs with the corresponding bands in ^{138}I. Excitation energies are given with respect to the 0-keV and X-keV levels in ^{140}Cs and ^{138}I, respectively. Data are taken from the present work and Ref. [93].

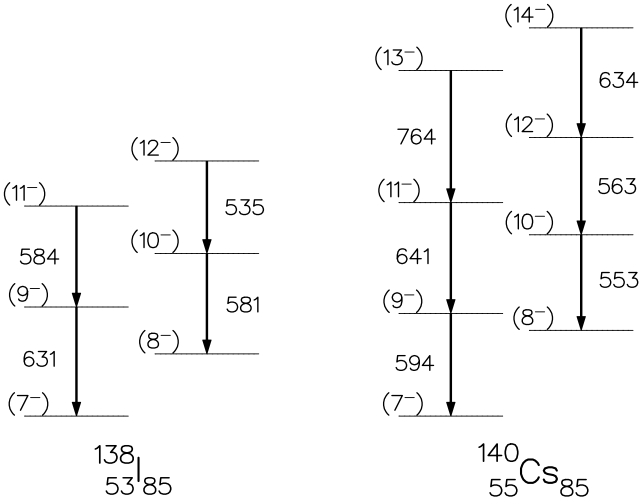

Figure 7.11: High-spin levels built on the (7⁻) level in ^{140}Cs and ^{138}I. Data are taken from the present work and Ref. [93].

It is also worth mentioning that ^{140}Cs, with two protons more than ^{138}I, shows more collectivity in the level pattern than ^{138}I, as presented in Fig. 7.11. Levels in ^{140}Cs are spaced more evenly than in ^{138}I and transition energies raise with increasing spins, which suggests that the addition of two protons to ^{138}I induces a change towards a collective motion. Moreover, the energy splitting in levels in ^{140}Cs are more obvious and larger than that in ^{138}Cs, as shown in Fig. 7.10. Bands 1 and 2, built on the (7^-) and (6^-) levels, respectively, show features of rotational bands. Thus, shell-model calculations are somewhat infeasible to describe the level pattern of ^{140}Cs. The collective level pattern also indicate that the octupole correlation, a collective motion, may be observed in ^{140}Cs with $Z = 55$ and $N = 85$, close to the $Z = 56$ and $N = 88$ octupole sub-shell gaps [22, 140–143], like heavier Cs isotopes, ^{141,143}Cs [60, 104] and ^{142}Cs discussed in Subsection 7.3.2.

Let us turn to band 3 in ^{140}Cs. The levels in this band are connected to the corresponding levels in band 1. A common feature observed in this nuclear region is the existence of octupole-phonon excitations. Octupole structures have been proposed in ^{141,143}Cs [60,104]. Two neighboring even-odd $N = 85$ isotones, ^{139}Xe and ^{141}Ba, also show octupole excitations built on a $13/2^+$ band-head, which is due to an octupole-phonon coupled to a $\nu(2f_{7/2})^3_{7/2}$ level [155, 156]. The octupole-phonon state has a spin-parity of 3^- at 2015 keV in ^{138}Xe and at 1803 keV in ^{140}Ba. Such a 3^- octupole-excitation state has been found in other $A = 140$ even-even nuclei in this region, namely ^{140}Xe and ^{140}Ce. Therefore, octupole excitations are expected to be present in ^{140}Cs. Furthermore, with the proton number increasing up to 61 and 63, ^{146}Pm ($N = 85$) and ^{148}Eu ($N = 85$) exhibit the octupole structures as well, where the

$11/2^-$ state in ^{145}Pm is coupled to the $\nu(2f_{7/2})^3_{7/2} \otimes 3^-$, $13/2^+$ state in ^{145}Nd [152] for the former and the $11/2^-$ state in ^{147}Eu to the $\nu(2f_{7/2})^3_{7/2} \otimes 3^-$, $13/2^+$ state in ^{147}Sm [154] for the latter. The first level of the octupole band in both ^{146}Pm and ^{148}Eu has $I^\pi = 12^-$, decaying to the 11^+ level in the yrast band by an $E1$ transition. So, a possible candidate band related to octupole excitations in ^{140}Cs is band 3, by analogy with the structure of ^{146}Pm and ^{148}Eu. The 2187.1-keV level in band 3 is likely to have a spin-parity of (12^+) by coupling the $7/2^+$ ground state of ^{139}Cs [139] to the $\nu(2f_{7/2})^3_{11/2} \otimes 3^-$, $17/2^+$ level in ^{139}Xe [155,156]. Then, (14^+) and (16^+) are assigned to the 2721.3- and 3328.4-keV levels, respectively, by assuming the crossover transitions of $E2$ character. The band-head of band 3 is expected to be the (10^+) level, formed by coupling the $7/2^+$ ground state of ^{139}Cs [139] to the first octupole level of $13/2^+$ in ^{139}Xe [155, 156]. However, this expected level is not observed. Therefore, bands 1 and 3 form a parity doublet and the simplex quantum number for this doublet is found to be $s = +1$.

For nuclei with a small number of valence particles ($N < 85$), octupole effects were explained due to octupole phonon excitations. In nuclei with a larger number of valence particles, one expects stronger octupole correlations, which will eventually cause octupole deformations of the nuclear potential. At $N = 85$, the number of valence particles may not be large enough to cause an octupole instability of the nuclear mean field, yet sufficient for numerous octupole excitations to appear. To check the stability of octupole excitations in ^{140}Cs, the energy displacement $\delta E(I) = E(I^-) - \frac{1}{2}\Big[E\big((I+1)^+\big) + E\big((I-1)^+\big)\Big]$ and the rotational frequency ratio $R(I) =$

$2\Big[E\big((I+1)^-\big) - E\big((I-1)^-\big)\Big]/\Big[E\big((I+2)^+\big) - E\big((I-2)^+\big)\Big]$ [141] of the $s = +1$ band structure (bands 1 and 3) are calculated and plotted in Figs. 7.12 and 7.13, respectively. Shown in Figs. 7.12 and 7.13 are also those of the $s = +i$ structure of the $N = 85$ isotones ^{139}Xe and ^{141}Ba [155, 156], the $s = -i$ structure of the $N = 86$ isotope ^{141}Cs [60], and the $s = +1$ structure of ^{140}Xe ($Z = 54$, $N = 86$) [112]. In Fig. 7.12, one sees that the curve of ^{140}Cs lies between those of the two isotones ^{139}Xe and ^{141}Ba and is close to those of ^{141}Cs and ^{140}Xe. All curves of these five nuclei are declining and approaching zero when spins increase. In the plots of $R(I)$, it is very interesting to note that the curve of ^{140}Cs is close to the vibration limit $R(I) = (2I-5)/(2I+1)$ with increasing spins, following the tendency observed in the other four nuclei, which may indicate octupole vibrations in ^{140}Cs, as proposed in ^{139}Xe [156], ^{141}Ba [156], ^{140}Xe [112], and ^{141}Cs [60]. The argument of octupole vibrations in ^{140}Cs appears inconsistent with the one obtained in Fig. 7.12, where the curve is decreasing to and even lower than zero, one of the criteria for the limit of stable octupole deformations. More experimental data and theoretical efforts are required to interpret this contradiction.

It is also worth showing excitation energies in octupole bands in these five nuclei. Figure 7.14 presents the excitation energies of corresponding levels in the three $N = 85$ isotones ^{139}Xe, ^{140}Cs, and ^{141}Ba, respectively. In this figure, one observes a decrease of octupole excitation energies from Xe to Cs and then to Ba at $N = 85$, a sign of increasing octupole excitations from Xe to Cs and then to Ba as proton numbers approach to 56. Excitation energies of octupole bands in ^{140}Xe, ^{140}Cs, and ^{141}Cs are

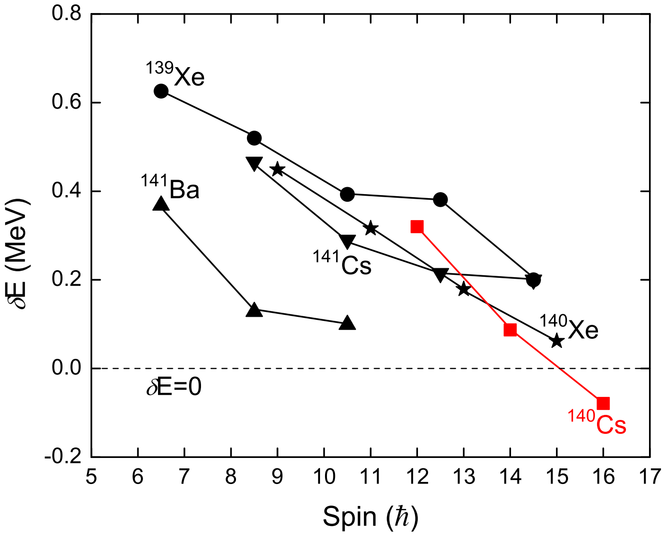

Figure 7.12: Energy displacement $\delta E(I)$ of the $s = +1$ band structure of ^{140}Cs and those of the $s = +i$ structure of the $N = 85$ isotones ^{139}Xe and ^{141}Ba [155, 156], the $s = -i$ structure of the $N = 86$ isotope ^{141}Cs [60], and the $s = +1$ structure of ^{140}Xe [112]. All curves are approaching zero with increasing spins.

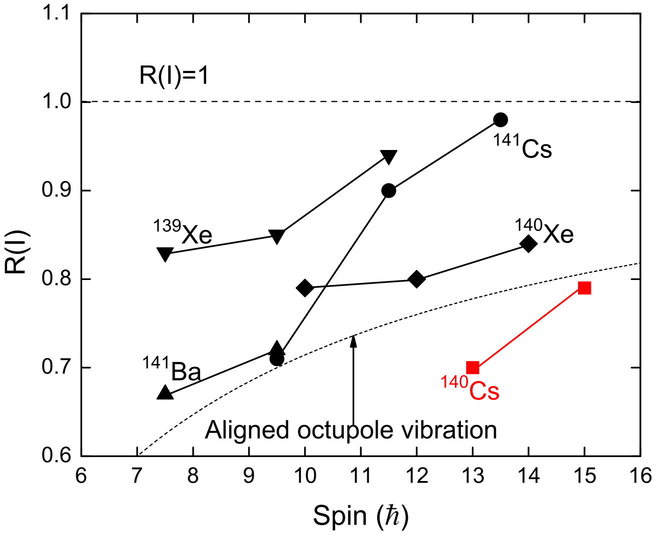

Figure 7.13: $R(I)$ of the $s = 1$ band structure of ^{140}Cs, the $s = +i$ band structure of ^{139}Xe and ^{141}Ba [155, 156], the $s = -i$ band structure of ^{141}Cs [60], and the $s = +1$ structure of ^{140}Xe [112].

shown in Fig. 7.15. Although Fig. 7.12 indicates octupole deformations in ^{140}Cs , most of the above evidence supports the proposal of the existence of octupole excitations of vibration character in ^{140}Cs. Additional theoretical work may provide a clarification.

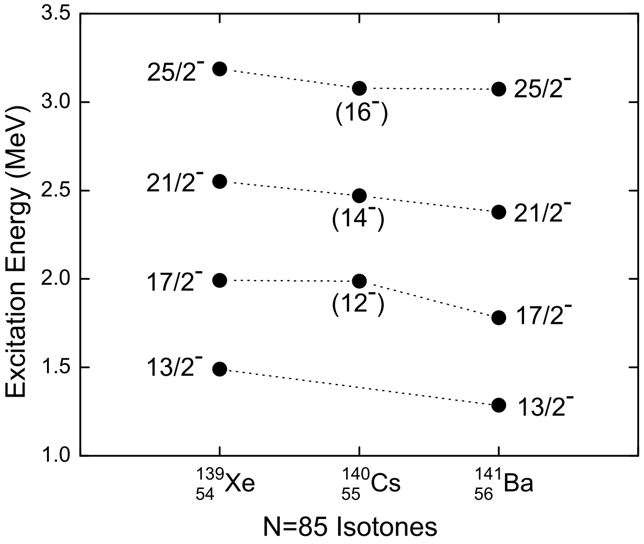

Figure 7.14: Excitation energies in octupole bands in $N = 85$ isotones ^{139}Xe, ^{140}Cs, and ^{141}Ba. The level energies are relative to the $7/2^-$ level in ^{139}Xe and ^{141}Ba and the 249.7-keV, (7^-) level in ^{140}Cs. Data are taken from the present work and Refs. [155, 156].

Even-even nuclei with 6 or 8 extra protons and 6 or 8 extra neutrons beyond the doubly-magic cores ^{132}Sn and ^{208}Pb exhibit the yrast band behavior of reflection asymmetry which is characterized by states of spin I and alternating parity $\pi = (-1)^I$ connected by collective $E1$ transitions at high spin ($I \geq 4$ or 6). This observation has been interpreted as a mix of octupole deformations with prolate-spheroidal-quadrupole deformations. In neighboring odd-A nuclei, one also finds parity-doubling examples. Regularly, the linking $E1$ transitions are very competi-

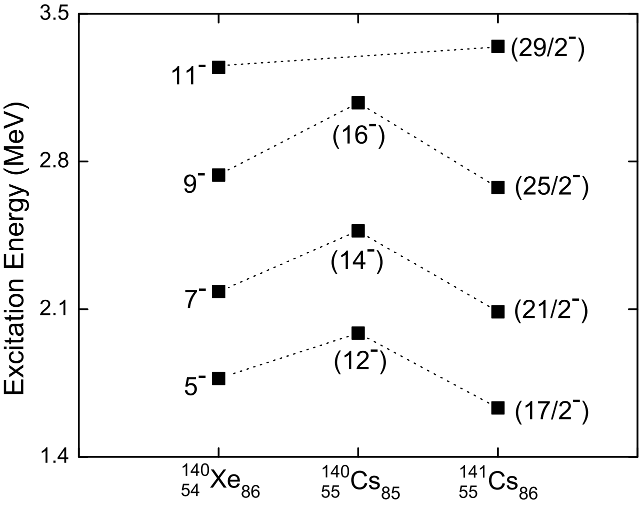

Figure 7.15: Excitation energies in octupole bands in ^{140}Xe, ^{140}Cs, and ^{141}Cs. The level energies are relative to the ground state in ^{140}Xe and ^{141}Cs and the 249.7-keV, (7^-) level in ^{140}Cs. Data are taken from the present work and Refs. [60, 112].

tive with $E2$ branches. A few examples have been found in neutron-rich Xe, Cs, Ba, La, and Ce isotopes. Following the reports on ^{141,143}Cs [60, 104] which showed evidence of octupole correlations, one again sees alternating parity in the weaker deformed ^{140}Cs as discussed above. We will further investigate the strength of octupole excitations in ^{140}Cs, namely the electric dipole moment D_0, in Subsection 7.3.2, along with the same quality in ^{142}Cs where octupole correlations are proposed.

7.3.2 ^{142}Cs

The ground state of ^{142}Cs was known to have $I^\pi = 0^-$, where the configuration $\pi(1g_{7/2})^{-3}\nu(2f_{7/2})^{-3}$ was believed to form the main component in the nuclear wave function [146]. The decay pattern of the current level scheme excludes the possibility that the 0-keV band-head is the ground state. So, we agree with the proposal in

Ref. [145] that the present level scheme is built on an isomer with $I \geq 2$. We cannot determine the spin and excitation energy of this isomeric state in the present work. All the level energies reported in the level scheme in Fig. 7.8 are relative to this isomer, while a symbol I is used for the spin of this isomer. However, this isomer is most likely to have a negative parity, based on the systematics of ^{140}Cs [108] and ^{144}La [29].

Multipolarity assignments for some transitions and the spin-parity assignments to the related levels in ^{142}Cs are made based on angular correlation measurements. Our angular correlation results in Table VII.1 agree with those reported in Ref. [145], except the one for the 218.3 → 96.9-keV cascade. Ours is consistent with theory for a pure quadrupole → pure quadrupole cascade [3, 5], whereas the authors in Ref. [145] claimed that the 96.6-keV transition probably has a $\Delta I = 1$, $E2/M1$ character. Though it is possible for this transition to have a $\Delta I = 1$, pure $E2$ multipolarity, the $\Delta I = 2$, $E2$ assignment is more reasonable given spin-parity assignments of other low-lying levels, as discussed in the following. Though the measurement of the total internal conversion coefficient (α_{T}) for the 96.9-keV transition is able to give direct information of its multipolarity, it is impracticable in the present work because we cannot determine the branching ratios of the low-energy transitions of energies 71.1 and 25.8 keV. Note that the authors in Ref. [145] claimed in their experimental section that the 123.0 and 25.3-keV levels, with spins of $I + 2$ and I, respectively, have an opposite parity to the X- and 96.6-keV levels, with spins of I and $I + 1$, respectively, but they concluded that the X-keV level has the same parity as the 123.0-keV level in their discussion section. Here, we propose that the 25.8-, 96.9-, and 123.1-keV levels have spins of $I+1$, $I+2$, and $I+3$, respectively, and all of them have the same parity as the 0-keV level. So, all three low-energy linking transitions of energies 25.8, 71.1, and 26.2 keV are of $\Delta I = 1$, $E2/M1$ character. These assignments bear a remarkable similarity to those in ^{140}Cs [108] and ^{144}La [29]. The assignment of $(I+3)^-$ to the 123.1-keV level is well supported by the non-observation of a 123.1-keV transition to the 0-keV, I^- level. In addition, all cascade transitions are assigned to be stretched $E2$. Of course, definite multipolarity assignments to these low-energy transitions are still an open question.

As listed in Table VII.1, the angular correlation for the 715.8 → 404.8-keV cascade agrees well with theory for a pure dipole → quadrupole cascade [3,5]. So pure dipole is assigned to the 715.8-keV transition. By considering the decay paths of the 1449.3-keV level, $E1$ is assigned to the 715.8-keV transition. The same assignment to the 618.8-keV transition is also made based on the angular correlation for the 618.8 → 408.6-keV cascade in Table VII.1. These $E1$ assignments allow us to assign positive parity to the levels in bands 3 and 4 in ^{142}Cs. Thus, bands 1 and 3, and bands 2 and 4 form two sets of alternating-parity doublets in ^{142}Cs, respectively. Then the octupole collectivity is proposed in ^{142}Cs, as seen in ^{140}Cs. This proposal is strongly supported by the remarkable resemblance among the level structures of ^{140,141,142,143}Cs.

For band 5, spins are assigned to the levels based on their decay patterns and the assumption that the cascade transitions are stretched $E2$.

One way to obtain the strength of octupole correlations in a nucleus is to calculate the electric dipole moment D_0 by measuring the corresponding $B(E1)/B(E2)$ ratios and the quadrupole moment Q_0. The nuclear electric dipole moment is a measure of the shift between the center of charge and the center of mass of the nucleus. The $B(E1)/B(E2)$ ratios of levels in the $s = +1$ doublet in ^{140}Cs and levels of two doublets in ^{142}Cs are calculated using the formula $B(E1)/B(E2) = 0.771\big[E_\gamma(E2)^5 I_\gamma(E1)\big]/\big[(E_\gamma(E1)^3 I_\gamma(E2)\big] \times 10^{-6}$ fm^{-2}, given in Table VII.2. The measured γ-ray branching ratios are also provided in Table VII.2. Note that the measured $B(E1)/B(E2)$ ratios in both ^{140}Cs and ^{142}Cs monotonically increase with increasing spins (excitation energies), as in ^{143}Cs ($s = +i$) [60, 104]. This effect, however, was not observed in ^{141}Cs [60]. One sees the same effect for the $s = +i$ doublet in ^{143}La [29] and ^{145}La [62]. Explanations of this observation require further theoretical work.

Table VII.2: $B(E1)/B(E2)$ ratios from the corresponding levels in ^{140,142}Cs. The transitions are followed by their intensities in parentheses.

Nucleus	Level spin ($\hbar$)	Level energy (keV)	$E_\gamma(E2)$ (keV)	$E_\gamma(E1)$ (keV)	$B(E1)/B(E2)$ (10^{-6} fm^{-2})
^{140}Cs	(14^+)	2721.3	534.2 (71)	472.5 (100)	0.45(12)
	(16^+)	3328.4	607.1 (100)	308.1 (30)	0.65 (17)
					average 0.55(18)
^{142}Cs	$(I+7)$	1342.6	269.5 (22)	618.8 (100)	0.03(1)
	$(I+9)$	1730.2	387.6 (100)	457.6 (49)	0.08(2)
	$(I+11)$	2233.4	503.2 (100)	258.7 (35)	0.50(14)
	$(I+8)$	1449.3	299.1 (42)	715.8 (100)	0.01(1)
	$(I+10)$	1862.8	413.5(100)	584.4(73)	0.03(1)
					average 0.13(4)

Here we use the rotational formula $D_0 = \sqrt{5B(E1)/16B(E2)} \times Q_0$ to calculate the electric dipole moment D_0 in a nucleus with octupole correlations. Since the Q_0 values of most even-even nuclei are available, those of odd-A nuclei can be taken from their corresponding neighboring even-even cores. However, for an odd-odd nucleus, it is more complicated. A "four-point interpolation" of the known Q_0 values of the neighboring even-even nuclei for ^{140,142}Cs is a good way to determine the Q_0 values of ^{140,142}Cs, respectively. The four neighboring even-even nuclei for ^{140}Cs are ^{138,140}Xe and ^{140,142}Ba, and for ^{142}Cs are ^{140,142}Xe and ^{142,144}Ba. However, the experimental Q_0 values of ^{138,142}Xe are not known. So, a "three-point interpolation" is used in practice. The average over ^{140}Xe (1.80(4) eb), ^{140}Ba (2.08(46) eb), and ^{142}Ba (2.65(7) eb) [160] yields $Q_0 = 2.18(44)$ eb for ^{140}Cs and the average over ^{142}Ba (2.65(7) eb), ^{144}Ba (3.25(9) eb), and ^{140}Xe (1.80(4) eb) [160] gives $Q_0 = 2.57(60)$ eb for ^{142}Cs. Using $Q_0 = 2.18(44)$ eb and the average value of all $B(E1)/B(E2)$ ratios in Table VII.2 in ^{140}Cs as $0.55(18)\times10^{-6}$ fm^{-2}, one obtains $D_0 = 0.09(3)$ $e$fm for ^{140}Cs. In the same manner, $D_0 = 0.05(2)$ $e$fm for ^{142}Cs is derived. Given the corresponding D_0 values for ^{141,143}Cs in Ref. [60], a plot is drawn to show the systematics of D_0 for ^{140,141,142,143}Cs, where octupole correlations have been proposed. This plot is given in Fig. 7.16, where those D_0 values reported in Sm, Nd, Ce, La, Ba, and Xe isotopes with octupole correlations are also included. Note that the D_0 value for ^{142}Cs is larger than that of ^{143}Cs [60]. Even if the very high value of $B(E1)/B(E2)$ of $0.50(14)\times10^{-6}$ fm^{-2} at $(I + 11)$ is deleted, the D_0 value for ^{142}Cs is obtained as 0.028(7) $e$fm, which is still larger than 0.015(5) $e$fm for ^{143}Cs [60].

The present study enriches our knowledge of the variation of the electric dipole moments in the Cs isotopic chain and provides further evidence for the proposal in Ref. [60] that a pronounced decrease of the electric dipole moments with increasing neutron numbers occurs in the Cs isotopes. These data presented in Fig. 7.16 show the

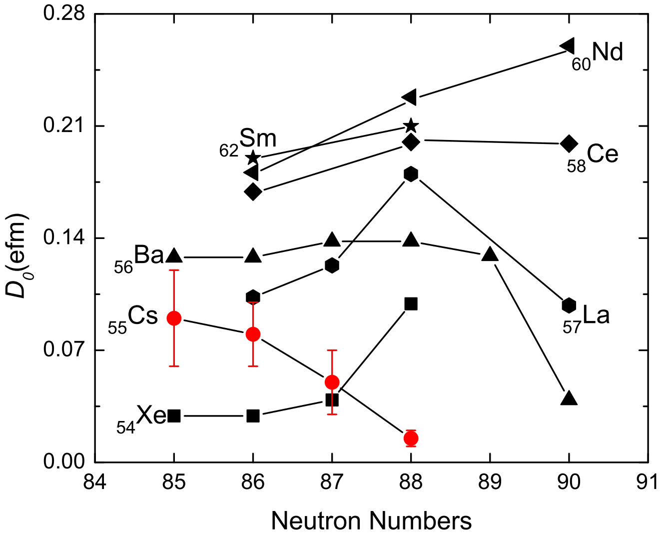

Figure 7.16: Electric dipole moments D_0 of ^{140,142}Cs compared to those reported in Sm, Nd, Ce, La, Ba, Cs, and Xe isotopes with octupole correlations. A pronounced decrease of D_0 is seen in the Cs isotopes. Data are taken from the present work for ^{140,142}Cs, from Ref. [29] for ^{143,144}La, and reproduced from Fig. 12 in Ref. [60] for other nuclei.

observation of decreasing electric dipole moments with increasing neutron numbers from ^{140}Cs to ^{143}Cs. In Fig. 7.16, one sees that the variation of the dipole moments in the above Cs isotopes follow those in Ba and La. The data show that the D_0 values for Ba have a small and definite increase, but they have a definite decrease at $N = 90$ for Ba and La. The decrease occurs earlier in the Cs isotopes. It is not necessary that the point where this decrease occurs should be the same for different isotopes. Note that a similar dramatic drop in D_0 was found at $N = 136$ in ^{224}Ra. As was discussed in Ref. [60], it is very likely that the decrease of D_0 with increasing neutron numbers observed in the Cs isotopic chain from ^{140}Cs to ^{143}Cs has an origin similar to that for the drop of D_0 for ^{146}Ba. Shell-correction calculations in the reflection-asymmetric mean field theory indicated that the dramatically reduced D_0 in ^{146}Ba is because of the very small shell-correction term, from the cancellation between contributions to

D_0^{shell} of protons and neutrons, and the negligible macroscopic contribution, due to the cancellation between the reorientation term and the neutron-skin term [161].

Moreover, one sees very good systematics of lowering of the D_0 values with decreasing proton numbers from $Z = 62$ (Sm) down to $Z = 54$ (Xe) at $N = 86, 87$, which can be interpreted as a shell effect of the $Z = 50$ closed shell [142]. The dipole moments of ^{143,144}La are located below the values of the corresponding Ba isotones only because their levels are not extended to as high spins as those in ^{145,147}La, where the $B(E1)/B(E2)$ ratios for higher-spin levels are much larger than those for lower-spin levels. This has been interpreted by Zhu *et al.* [62] as configuration mixing in the lower-spin states.

7.4 Conclusion

The nuclear structure of the odd-odd, $N = 85$ nucleus ^{140}Cs has been re-investigated. A measurement has been performed to firmly assign the mass number 140 to the previously known transitions. Eight new excited levels with thirteen new deexciting transitions at high spin and three new excited levels with seven new deexciting transitions at low and medium spin are observed to enable us to establish the level scheme of ^{140}Cs. Spins and parities of levels in ^{140}Cs are tentatively assigned on the basis of angular correlation measurements, systematics of $N = 85$ isotones, and the proposal of the existence of octupole excitations. The structure of ^{140}Cs has been discussed and the newly identified side-band (band 3) along with band 1 is proposed to form an $s = +1$ octupole doublet. Further examinations indicate that octupole excitations are more of vibration character in ^{140}Cs.

A new level scheme of ^{142}Cs has been established. Spin-parities have been tentatively assigned to levels in ^{142}Cs based on angular correlations and systematics of neighboring nuclei. Two sets of alternating-parity doublets are extended to indicate more definite octupole correlations in ^{142}Cs.

The average electric dipole moments for ^{140,142}Cs are measured and compared with ^{141,143}Cs and other neighboring nuclei observed with octupole correlations. A remarkable decrease in D_0 in the Cs isotopic chain with increasing neutron numbers is found, which may be analogous to the drop of D_0 in ^{146}Ba. The pronounced drop of D_0 in the Cs isotopes may have a similar origin to that in the Ba isotopes. More theoretical efforts are needed to interpret what we have found in the Cs isotopes with octupole correlations.

CHAPTER VIII

CONCLUSIONS

The present dissertation is accomplished mainly by analyzing our fission experimental data collected in 2000. A large amount of γ-ray coincidence events were accumulated with the Gammasphere detector array for further detailed analysis of properties of neutron-rich nuclei produced in the spontaneous fission of ^{252}Cf.

A few nuclei in three different mass regions have been studied. They are: (a) ^{114,115}Rh in the $A = 110$ region, where triaxiality plays an important role in the nuclear structure; (b) ^{134}I, ^{137}I, ^{139}Cs, and four $N = 83$ isotones beyond the doubly-magic core ^{132}Sn, where the shell model is suitable for describing their properties; (c) ^{140}Cs and ^{142}Cs near the region centered on $Z = 56$, $N = 88$, where octupole deformations/correlations were proposed.

The first identification of high-spin excited states in ^{114,115}Rh provides very important information on the structure of Rh nuclei in the more neutron-rich region. A $\Delta I = 1$, negative-parity yrast band and a side-band in ^{114}Rh are found. The signature inversion of the yrast bands of ^{106,112,114}Rh is observed at 13.7 $\hbar$ for ^{106}Rh, 12.5 $\hbar$ for ^{112}Rh, and 10.6 $\hbar$ for ^{114}Rh. The triaxial deformation is proposed to result in the signature inversion. The level scheme of ^{115}Rh is established with an yrast band and an yrare band. The large signature splitting and the yrare band show features of a typical triaxial nucleus. Preliminary calculations based on the rigid-triaxial-rotor-plus-quasiparticle model have been performed to predict triaxiality of $\gamma = 28°$ for

^{115}Rh.

A new high-spin level scheme of ^{134}I has been established for the first time. This high-spin level scheme is proposed to be built on the 8^- isomeric state. Shell-model calculations have been performed and good agreement with experiment is found for both level energies and spin-parity assignments. Two $N = 84$ isotones ^{137}I and ^{139}Cs have been studied. The high-spin structure of ^{139}Cs is investigated, by extending its level scheme to 4670 keV. Spins and parities of levels in ^{139}Cs are firmly assigned up to $25/2^+$ experimentally. High-spin states in ^{137}I are extended as well. The level patterns of these two isotones indicate the important role that the two major shells $Z = 50$ and $N = 82$ play in their structures. Realistic shell-model calculations have been carried out to interpret the structures of ^{137}I and ^{139}Cs, by choosing ^{132}Sn as a closed core. The calculations provide a very satisfactory description for both isotones, with discrepancies not exceeding 150 keV for most of the states up to 3.5 MeV. This shows that the interpretation of the low- to medium-energy levels in ^{137}I and ^{139}Cs is well within the shell-model framework. However, for levels higher than $33/2^+$ in both ^{137}I and ^{139}Cs, larger discrepancies are found, which may indicate that excitations outside the chosen model space play an important role for such states. The present work indicates that the shell model can be used for neutron-rich nuclei as far as $Z = 55$ and $N = 84$.

The g-factor of the $15/2^-$ state in ^{137}Xe has been measured for the first time to extend our knowledge of g-factors in nuclei having several nucleons beyond the doubly-magic core ^{132}Sn. The measured value is in good agreement with the theoretical prediction from the shell model. Based on observed angular correlations, spins and parities are assigned to several levels in four $N = 83$ isotones ^{135}Te, ^{136}I, ^{137}Xe, and ^{138}Cs. These assignments are supported by the present shell-model calculations, which also show configuration mixing in these nuclei caused by one more neutron than their corresponding $N = 82$ isotopes and increasing proton numbers.

The nuclear structures of the odd-odd ^{140}Cs and ^{142}Cs have been re-investigated. A new level scheme with a new side-band is built in ^{140}Cs. Spins and parities of levels in ^{140}Cs are tentatively assigned. The structure of ^{140}Cs has been discussed and the new side-band (band 3) along with band 1 is proposed to form an $s = +1$ octupole doublet more of vibration character. A new level scheme of ^{142}Cs has been established. Spin-parities have been tentatively assigned to levels in ^{142}Cs. Two sets of alternating-parity doublets are built to indicate octupole correlations in ^{142}Cs. The average electric dipole moments for ^{140,142}Cs are measured and compared with neighboring nuclei. A striking decrease in D_0 in the Cs isotopic chain with increasing neutron numbers is found. The pronounced drop of D_0 in the Cs isotopes may have a similar origin to that in the Ba isotopes at $N = 90$.

In a word, the present dissertation enriches our knowledge of nuclear structures of neutron-rich nuclei produced in the spontaneous fission of ^{252}Cf. The current studies involve three important mass regions, which are of great interest in both theory and experiment.

REFERENCES

[1] D. R. Hamilton, Physical Review **58**, 122 (1940).

[2] *Beta- and Gamma-Ray Spectroscopy*, edited by K. Siegbahn (Interscience Publishers Inc., New York, 1955).

[3] H. W. Taylor, B. Singh, F. S. Prato, and R. McPherson, Atomic Data and Nuclear Data Tables **9**, 1 (1971).

[4] *The Electromagnetic Interaction in Nuclear Spectroscopy*, edited by W. D. Hamilton (American Elsevier Publishing Company, New York, 1975).

[5] P. E. Haustein, H. W. Taylor, R. McPherson, and R. Fairchild, Atomic Data and Nuclear Data Tables **10**, 321 (1972).

[6] A. J. Becker and R. M. Steffen, Physical Review **180**, 1043 (1969).

[7] http://physics.anu.edu.au/nuclear/bricc/.

[8] K. Li, Ph.D. thesis, Vanderbilt University, 2008.

[9] X. Q. Zhang, Ph.D. thesis, Vanderbilt University, 2001.

[10] M. Mayer and J. Jensen, *Elementary Theory of Nuclear Shell Structure* (John Wiley and Sons, Inc., New York, 1955).

[11] K. Heyde, *Basic Ideas and Concepts in Nuclear Physics: An Introductory Approach* (Institute of Physics Publishing, Bristol and Philadelphia, 1994).

[12] G. Racah, Physical Review **78**, 622 (1950).

[13] K. Li *et al.*, Physical Review C **75**, 044314 (2007).

[14] C. Goodin *et al.*, Physical Review C **78**, 044331 (2008).

[15] J. M. Eisenberg and W. Greiner, *Nuclear Theory*, 3rd rev. ed. (North-Holland, Amsterdam, 1987), Vol. 1.

[16] H. Mach *et al.*, Physical Review C **41**, 1141 (1990).

[17] S. G. Nilsson, Kgl. Danske Videnskab. Selskab., Mat.-fys Medd **29**, (1955).

[18] S. G. Nilsson and I. Ragnarsson, *Shapes and Shells in Nuclear Structure* (Cambridge University Press, Cambridge, 1995).

[19] J. H. Hamilton *et al.*, Journal of Physics G **10**, L87 (1984).

[20] J. H. Hamilton, Progress in Particle and Nuclear Physics **15**, 107 (1985).

[21] J. H. Hamilton, in *Treatise on Heavy Ion Science*, edited by A. Bromley (Plenum Press, New York, 1989), Vol. 8, pp. 2–98.

[22] G. A. Leander *et al.*, Physics Letters B **152**, 284 (1985).

[23] P. A. Butler and W. Nazarewicz, Reviews of Modern Physics **68**, 349 (1996).

[24] J. H. Hamilton *et al.*, Progress in Particle and Nuclear Physics **35**, 635 (1995).

[25] A. C. Wahl, Atomic Data and Nuclear Data Tables **39**, 1 (1988).

[26] *Table of Isotopes*, 8th ed., edited by R. B. Firestone and V. S. Shirley (John Wiley & Sons, Inc., New York, 1996).

[27] F. Yang and J. H. Hamilton, *Modern Atomic and Nuclear Physics*, revised ed. (World Scientific Publishing Company, Singapore, 2010).

[28] G. M. Ter-Akopian *et al.*, Physical Review Letters **73**, 1477 (1994).

[29] Y. X. Luo *et al.*, Nuclear Physics **A818**, 121 (2009).

[30] A. V. Daniel *et al.*, Nuclear Instruments and Methods in Physics Research Section B **262**, 399 (2007).

[31] C. T. Goodin, Ph.D. thesis, Vanderbilt University, 2008.

[32] E. Matthias, S. S. Rosenblum, and D. A. Shirley, Physical Review Letters **14**, 46 (1965).

[33] C. Goodin *et al.*, Physical Review C **79**, 034316 (2009).

[34] C. Goodin *et al.*, Physical Review C **80**, 014318 (2009).

[35] G. N. Rao, Hyperfine Interactions **26**, 1119 (1985).

[36] J. Skalski, S. Mizutori, and W. Nazarewicz, Nuclear Physics **A617**, 282 (1997).

[37] H. Hua *et al.*, Physical Review C **69**, 014317 (2004).

[38] Y. X. Luo *et al.*, Journal of Physics G **31**, 1303 (2005).

[39] Y. X. Luo *et al.*, Physical Review C **70**, 044310 (2004).

[40] Y. X. Luo *et al.*, Physical Review C **74**, 024308 (2006).

[41] Y. X. Luo *et al.*, Physical Review C **69**, 024315 (2004).

[42] Ts. Venkova *et al.*, The European Physical Journal A **6**, 405 (1999).

[43] Ts. Venkova *et al.*, The European Physical Journal A **15**, 429 (2002).

[44] A. Jokinen *et al.*, Nuclear Physics **A549**, 420 (1992).

[45] J. Kurpeta *et al.*, The European Physical Journal A **31**, 263 (2007).

[46] R. Duffait *et al.*, Nuclear Physics **A454**, 143 (1986).

[47] P. Joshi *et al.*, Physics Letters B **595**, 135 (2004).

[48] M.-G. Porquet *et al.*, The European Physical Journal A **15**, 463 (2002).

[49] M.-G. Porquet *et al.*, The European Physical Journal A **18**, 25 (2003).

[50] N. Fotiades *et al.*, Physical Review C **67**, 064304 (2003).

[51] W. B. Walters, E. A. Henry, and R. A. Meyer, Physical Review C **29**, 991 (1984).

[52] S. H. Liu *et al.*, Physical Review C **79**, 067303 (2009).

[53] S. K. Saha *et al.*, Physical Review C **65**, 017302 (2001).

[54] P. Bhattacharyya *et al.*, Physical Review C **56**, R2363 (1997).

[55] L. M. Yang *et al.*, Chinese Physics Letters **18**, 24 (2001).

[56] H. B. Ding *et al.*, Chinese Physics Letters **24**, 1517 (2007).

[57] Q. H. Lu *et al.*, Physical Review C **52**, 1348 (1995).

[58] J. K. Hwang *et al.*, Physical Review C **74**, 017303 (2006).

[59] Y. J. Chen *et al.*, Physical Review C **73**, 054316 (2006).

[60] Y. X. Luo *et al.*, Nuclear Physics **A838**, 1 (2010).

[61] J. K. Hwang *et al.*, Physical Review C **58**, 3252 (1998).

[62] S. J. Zhu *et al.*, Physical Review C **59**, 1316 (1999).

[63] J. G. Wang *et al.*, Physical Review C **78**, 014313 (2008).

[64] L. Gu *et al.*, Physical Review C **79**, 054317 (2009).

[65] Q. Xu *et al.*, Physical Review C **78**, 064301 (2008).

[66] http://www.nndc.bnl.gov/.

[67] I. Hamamoto, Nuclear Physics **A520**, 297c (1990).

[68] F. R. Espinoza-Quiñones *et al.*, Physical Review C **52**, 104 (1995).

[69] R. Bengtssonb, H. Frisk, F. R. Mayd, and J. A. Pinston, Nuclear Physics **A415**, 189 (1984).

[70] I. Hamamoto, Physics Letters B **235**, 221 (1990).

[71] N. Tajima, Nuclear Physics **A572**, 365 (1994).

[72] K. Hara and Y. Sun, Nuclear Physics **A531**, 221 (1991).

[73] Z. C. Gao, Y. S. Chen, and Y. Sun, Physics Letters B **634**, 195 (2006).

[74] R. A. Bark *et al.*, Physics Letters B **406**, 193 (1997).

[75] N. Yoshida, H. Sagawa, and T. Otsuka, Nuclear Physics **A567**, 17 (1994).

[76] F. R. Xu, W. Satuła, and R. Wyss, Nuclear Physics **A669**, 119 (2000).

[77] R. R. Zheng, S. Q. Zhu, and X. D. Luo, International Journal of Modern Physics E **12**, 59 (2003).

[78] R. R. Zheng *et al.*, Chinese Physics Letters **21**, 1475 (2004).

[79] J. Timár *et al.*, Nuclear Physics **A696**, 241 (2001).

[80] J. Timár *et al.*, Acta Physica Polonica B **33**, 493 (2002).

[81] A. Gelberg *et al.*, Nuclear Physics **A557**, 439c (1993).

[82] J. K. Hwang *et al.*, Physical Review C **65**, 054314 (2002).

[83] J. A. Alcántara-Núñez *et al.*, Physical Review C **69**, 024317 (2004).

[84] D. Sohler *et al.*, Physical Review C **71**, 064302 (2005).

[85] I. Deloncle *et al.*, The European Physical Journal A **8**, 177 (2000).

[86] J. A. Shannon *et al.*, Physics Letters B **336**, 136 (1994).

[87] J. A. Grau *et al.*, Physical Review C **14**, 2297 (1976).

[88] S. Lalkovski *et al.*, The European Physical Journal A **18**, 589 (2003).

[89] K. Butler-Moore *et al.*, Journal of Physics G **25**, 2253 (1999).

[90] M. A. Stoyer *et al.*, Nuclear Physics **A787**, 455c (2007).

[91] S. E. Larsson, G. Leander, and I. Ragnarsson, Nuclear Physics **A307**, 189 (1978).

[92] A. Korgul *et al.*, The European Physical Journal A **12**, 129 (2001).

[93] T. Rząca-Urban *et al.*, Physical Review C **75**, 054319 (2007).

[94] W. Urban *et al.*, Physical Review C **65**, 024307 (2002).

[95] V. Berg and A. Hoglund, Nuclear Physics **A175**, 495 (1971).

[96] R. A. Meyer *et al.*, Physical Review C **13**, 1617 (1976).

[97] C. D. Coryell *et al.*, Nuclear Physics **A179**, 689 (1972).

[98] A. Nowak *et al.*, The European Physical Journal A **6**, 1 (1999).

[99] O. B. Dabbousi, M. H. Prior, and H. A. Shugart, Physical Review C **3**, 1326 (1971).

[100] C. Thibault *et al.*, Nuclear Physics **A367**, 1 (1981).

[101] W. Urban *et al.*, The European Physical Journal A **27**, 257 (2006).

[102] P. Bhattacharyya *et al.*, Physical Review C **64**, 054312 (2001).

[103] L. Coraggio, A. Covello, A. Gargano, and N. Itaco, Physical Review C **80**, 061303 (2009).

[104] W. Urban *et al.*, Physical Review C **69**, 017305 (2004).

[105] W. Urban *et al.*, Physical Review C **70**, 057308 (2004).

[106] R. Broda *et al.*, Physical Review C **59**, 3071 (1999).

[107] T. Rząca-Urban *et al.*, The European Physical Journal A **32**, 5 (2007).

[108] S. H. Liu *et al.*, Physical Review C **81**, 037302 (2010).

[109] S. H. Liu *et al.*, Physical Review C **81**, 057304 (2010).

[110] S. H. Faller *et al.*, Physical Review C **38**, 905 (1988).

[111] A. Korgul *et al.*, The European Physical Journal A **7**, 167 (2000).

[112] W. Urban *et al.*, The European Physical Journal A **16**, 303 (2003).

[113] J. K. Hwang *et al.*, Physical Review C **69**, 057301 (2004).

[114] P. Bhattacharyya *et al.*, The European Physical Journal A **3**, 109 (1998).

[115] S. J. Zhu *et al.*, Chinese Physics Letters **14**, 569 (1997).

[116] L. Coraggio *et al.*, Progress in Particle and Nuclear Physics **62**, 135 (2009).

[117] L. Coraggio, A. Covello, A. Gargano, and N. Itaco, Physical Review C **72**, 057302 (2005).

[118] T. Engeland, OSLO shell-model code, 1991-2006 (unpublished).

[119] A. Korgul *et al.*, The European Physical Journal A **32**, 25 (2007).

[120] A. Covello, L. Coraggio, A. Gargano, and N. Itaco, Progress in Particle and Nuclear Physics **59**, 401 (2007).

[121] A. Korgul *et al.*, Physical Review C **64**, 021302 (2001).

[122] J. Shergur *et al.*, Physical Review C **65**, 034313 (2002).

[123] J. Shergur *et al.*, Physical Review C **72**, 024305 (2005).

[124] S. Sarkar and M. S. Sarkar, The European Physical Journal A **21**, 61 (2004).

[125] R. Kshetri, M. S. Sarkar, and S. Sarkar, Physical Review C **74**, 034314 (2006).

[126] B. Fornal *et al.*, Physical Review C **63**, 024322 (2001).

[127] S. Sarkar and M. Saha Sarkar, Physical Review C **64**, 014312 (2001).

[128] P. J. Daly *et al.*, Physical Review C **59**, 3066 (1999).

[129] R. G. Clark, L. E. Glendenin, and W. L. Talbert, in *Proceedings of the Third IAEA Symposium on the Physics and Chemistry of Fission* (International Atomic Energy Agency, Vienna, 1974, Rochester, New York, 1973), Vol. 2, p. 221.

[130] L. Coraggio, A. Covello, A. Gargano, and N. Itaco, Physical Review C **73**, 031302 (2006).

[131] A. Gargano, L. Coraggio, A. Covello, and N. Itaco, Journal of Physics: Conference Series **168**, 012013 (2009).

[132] R. Machleidt, Physical Review C **63**, 024001 (2001).

[133] S. Bogner *et al.*, Physical Review C **65**, 051301 (2002).

[134] B. A. Brown, A. Etchegoyen, and W. D. M. Rae, Technical Report No. 524, Michigan State University National Superconducting Cyclotron Laboratory, (unpublished), OXBASH shell-model code.

[135] C. T. Zhang *et al.*, Physical Review Letters **77**, 3743 (1996).

[136] L. Coraggio, A. Covello, A. Gargano, and N. Itaco, Physical Review C **80**, 021305(R) (2009).

[137] B. Fogelberg *et al.*, Physical Review C **75**, 054308 (2007).

[138] T. Rząca-Urban *et al.*, Physics Letters B **348**, 336 (1995).

[139] S. H. Liu *et al.*, Physical Review C **80**, 044314 (2009).

[140] W. Nazarewicz *et al.*, Nuclear Physics **A429**, 269 (1984).

[141] W. Nazarewicz and P. Olanders, Nuclear Physics **A441**, 420 (1985).

[142] W. Nazarewicz and S. L. Tabor, Physical Review C **45**, 2226 (1992).

[143] I. Ahmad and P. A. Butler, Annual Review of Nuclear and Particle Science **43**, 71 (1993).

[144] R. K. Sheline, A. K. Jain, and K. Jain, Physical Review C **38**, 2952 (1988).

[145] T. Rząca-Urban *et al.*, Physical Review C **80**, 064317 (2009).

[146] C. Ekström, L. Robertsson, G. Wannberg, and J. Heinemeier, Physica Scripta **19**, 516 (1979).

[147] G. H. Carlson, W. L. Talbert, and J. R. McConnell, Physical Review C **9**, 283 (1974).

[148] M. N. Mineva *et al.*, The European Physical Journal A **11**, 9 (2001).

[149] G. S. Simpson *et al.*, Physical Review C **76**, 041303 (2007).

[150] H. W. Taylor and A. H. Kukoc, Nuclear Physics **A122**, 425 (1968).

[151] P. Drehmann, Zeitschrift Physik **271**, 349 (1974).

[152] T. Rząca-Urban *et al.*, Nuclear Physics **A588**, 767 (1995).

[153] M. Piiparinen *et al.*, Zeitschrift für Physik A **301**, 231 (1981).

[154] J. R. Jongman *et al.*, Nuclear Physics **A581**, 165 (1995).

[155] Y. X. Luo *et al.*, Physical Review C **66**, 014305 (2002).

[156] W. Urban *et al.*, Physical Review C **66**, 044302 (2002).

[157] W. Urban *et al.*, Physical Review C **61**, 041301R (2000).

[158] W. Urban *et al.*, Physical Review C **53**, 2516 (1996).

[159] S. Flibotte *et al.*, Nuclear Physics **A530**, 187 (1991).

[160] S. Raman, C. W. Nestor, and P. Tikkanen, Atomic Data and Nuclear Data Tables **78**, 1 (2001).

[161] P. A. Butler and W. Nazarewicz, Nuclear Physics **A533**, 249 (1991).